University of Wollongong

Research Online

University of Wollongong Thesis Collection 2017+

University of Wollongong Thesis Collections

2019

Thermionic emission and electron transport in Dirac materials

Sunchao Huang

Follow this and additional works at: https://ro.uow.edu.au/theses1

University of Wollongong

Copyright Warning

You may print or download ONE copy of this document for the purpose of your own research or study. The University does not authorise you to copy, communicate or otherwise make available electronically to any other person any copyright material contained on this site.

You are reminded of the following: This work is copyright. Apart from any use permitted under the Copyright Act 1968, no part of this work may be reproduced by any process, nor may any other exclusive right be exercised, without the permission of the author. Copyright owners are entitled to take legal action against persons who infringe their copyright. A reproduction of material that is protected by copyright may be a copyright infringement. A court may impose penalties and award damages in relation to offences and infringements relating to copyright material. Higher penalties may apply, and higher damages may be awarded, for offences and infringements involving the conversion of material into digital or electronic form.

Unless otherwise indicated, the views expressed in this thesis are those of the author and do not necessarily represent the views of the University of Wollongong.

Research Online is the open access institutional repository for the University of Wollongong. For further information contact the UOW Library: research-pubs@uow.edu.au

School of Physics

Thermionic emission and electron transport in Dirac materials

Sunchao Huang

“This thesis is presented as part of the requirements for
the award of the Degree of Doctor of Philosophy
of the University of Wollongong”

Thesis supervisors:
Prof. Chao Zhang
Dr. Enbang Li

September/2019

Certification

I, Sunchao Huang, declare that this thesis, submitted in partial fulfilment of the requirements for the award of Doctor of Philosophy, in the School of Physics, University of Wollongong, is wholly my own work unless otherwise referenced or acknowledged. The document has not been submitted for qualifications at any other academic institution.

Sunchao Huang
September 2019

Acknowledgements

First of all, I would like to express my deep sense of gratitude to my supervisor Professor Chao Zhang for his encouragement, inspiration, continued support and guidance throughout my research. His optimism, goodness, kindness and calmness make me feel comfortable and encouraged. I express my great thanks to my co-supervisor Dr. Enbang Li for his help and support.

I would like to thank Professor R. A. Lewis for his guidance in academic writing. I thank Dr. Matthew Sanderson and Jack Zuber for their language polishing to my publications.

I am pleased to express my thanks to everyone who has offered their time and help to me at the University of Wollongong.

I sincerely thank Dr. Feng Gao, Dr. Suoguo Chen, Dr. Zhijin Yan and Dr. Wenye Duan for their encouragement both in my research and life.

I thank Qinqing Xu, Dan Zhang, Qiong Wang, Selin Akaraci, Liqun Sun, Xianyan Yang, Zhongyuan Yao, Hao Zhang and all my friends for their company.

I would like to express my deepest sense of gratitude to my parents, family and relatives for the continued support and encouragement.

Abstract

In this thesis, we study thermionic emission in two kinds of Dirac materials, namely Dirac semimetals and nodal-ring semimetals. Starting with the linear energy-momentum dispersion, we develop a modified Richardson-Dushman (RD) law to describe the thermionic emission current in 3D Dirac semimetals. The modified RD law has no mass dependence, which is significantly different from the RD law. We found the average energy carried by a degree of freedom in Dirac semimetals is twice of that in conventional materials. As a result, 3D Dirac semimetals have the best thermal efficiency and coefficient of performance when compared to conventional semiconductors and graphene.

The density of states of 3D Dirac semimetals is smaller than that of 3D conventional materials, which results in a relatively smaller thermionic current density. A new type of 3D Dirac material, nodal-ring has a larger density of states near to the Dirac cones due to it having more Dirac cones compared to Dirac semimetals. We developed a modified RD law to calculate its thermionic emission current. The results show the thermionic emission current can be enhanced by the nodal-ring. Additionally, it has different thermionic emission in the x- and y-directions due to the anisotropic energy-momentum dispersion.

Thermionic emission has many potential applications in harvesting thermal energy and cooling. We calculate the heat transfer from electronic devices without and with thermionic cooling. Without thermionic cooling, the internal temperature of the devices is at best equal to and usually higher than the temperature of the surrounding environment. However, when thermionic cooling is employed to transport heat, the internal temperature can be considerably lower than the environmental temperature.

Additionally, hot carrier relaxation is studied in gapped Dirac semimetals. A finite gap relaxes the selection rule and gives rise to a nonvanishing internode coupling via phonon scattering. The gap also enhances the intra-node scattering. By using the Boltzmann transport equation, we find that the relaxation rate increases with the square of the gap and the electron temperature.

Finally, we investigate the strong tunable photo-mixing in semi-Dirac semimetals in the terahertz regime. The third-order photoresponses along the linear and parabolic directions have been analyzed and determined quantitatively. We have found a remarkable tunability of the mixing efficiency along the parabolic direction by a small electric field in the linear direction, up to two orders of magnitude.

List of Journal Articles

[1] Huang, S., Sanderson, M., Tian, J., Chen, Q., Wang, F., & Zhang, C. (2017). Hot carrier relaxation in three dimensional gapped Dirac semi-metals. Journal of Physics D: Applied Physics, 51(1), 015101.

[2] Huang, S., Sanderson, M., Zhang, Y., & Zhang, C. (2017). High efficiency and non-Richardson thermionics in three dimensional Dirac materials. Applied Physics Letters, 111(18), 183902.

[3] Huang, S., Tran, M. H., Zuber, J., Wang, Q., Zhu, Y., & Zhang, C. (2019). Strong tunable photomixing in semi-Dirac materials in the terahertz regime. JOSA B, 36(2), 200-203.

[4] Huang, S., Lewis, R., & Zhang, C. (2019). Thermionic enhanced heat transportation in electronic devices based on 3D Dirac materials. Journal of Applied Physics, 126(16), 165105.

[5] Sanderson, M., Huang, S., Bao, Q., & Zhang, C. (2017). Optical conductivity of a commensurate graphene-topological insulator heterostructure. Journal of Physics D: Applied Physics, 50(38), 385301.

[6] Sanderson, M., Huang, S., Zhang, Y., & Zhang, C. (2018). Frequency and orientation dependent conductivity of a semi-Dirac system. Journal of Physics D: Applied Physics, 51(20), 205302.

[7] Zuber, J., Huang, S., Tian, J., & Zhang, C. (2018). Dynamical polarization in a

graphene-topological-insulator heterostructure. Materials Research Express, 6, 045603.

[8] Tian, J., Zuber, J., Huang, S., & Zhang, C. (2019). Superconducting pair-breaking under intense sub-gap terahertz radiation. Applied Physics Letters, 114(21), 212601.

List of Conference Articles

[1] Huang, S., Zuber, J., Li, E & Zhang, C. Strong Anisotropic Photo-mixing Effect of Semi-Dirac Materials in the Terahertz Regime, 44th Conference on Infrared, Millimeter and Terahertz Waves (IRMMW-THz 2019), Pairs, France.

[2] Huang, S., Zuber, J., Li, E & Zhang, C. Bandgap Dependence of Hot Electron Relaxation in Three Dimensional Dirac Semi-Metals, 44th Conference on Infrared, Millimeter and Terahertz Waves (IRMMW-THz 2019), Pairs, France.

Contents

List of Figures

Chapter 1

Introduction

There are two fundamental research topics in physics. One of them is to explore the nature of light and its interactions with substances. The last four centuries from Newton's era (the seventeenth century) to Albert Einstein's era (the twentieth century) have witnessed endless wars between particles and waves of light. Now, it is widely accepted that light has wave-particle duality and manifests one of them depending on how it is observed. Partly based on this postulate, quantum mechanics has been established, opening the door to modern science. In return, the area of light has been significantly enriched thanks to the establishment of quantum mechanics.

The other research area is to find the fundamental building blocks of matter, such as atoms, electrons and phonons, as well as how these building blocks form substances such as crystals, magnets and superconductors. At the beginning of the 20^{th} century, most physicists thought that there were no new building blocks to be discovered. Moreover, Landau's spontaneous symmetry breaking theory can well describe these known quantum states. In 1980, a new building block, the quantum Hall (QH) state was discovered. This new state does not adhere to Landau's paradigm [2]. In order to describe the new quantum state, topological concepts have been introduced. Soon, many topological materials such as Dirac semimetals and Weyl semimetals were discovered [3–7].

According to band theory, traditional materials can be classified into three different types (shown in Fig. 1.1), namely (a) metals, (b) semiconductors and (c) insulators. For metals, the conduction band and valence band are overlapped. Hence, there are many electrons in the bottom of the conduction band, which makes metals good conductors.

If there is a gap between the valence band and conduction band and the gap is less than 3 eV, then the material is called semiconductor. The conduction band has no electrons at absolute zero temperature (0 K) and cannot transport current, while it has a few electrons due to thermal excitations at a finite temperature. If the gap is greater than 3 eV, then the state is called insulator where the conduction band can hardly obtain electrons via thermal excitation. Unlike ordinary insulators, topological insulators (d) not only have gapped bulk states but also have topologically protected surface states. The gapless surface states have a linear energy-momentum dispersion, which makes a very small effective electron mass. Additionally, the electrons in the surface states obey the Dirac equation instead of the Schrödinger equation. Moreover, the electrons in surface states move in one direction which is robust to dissipation [8].

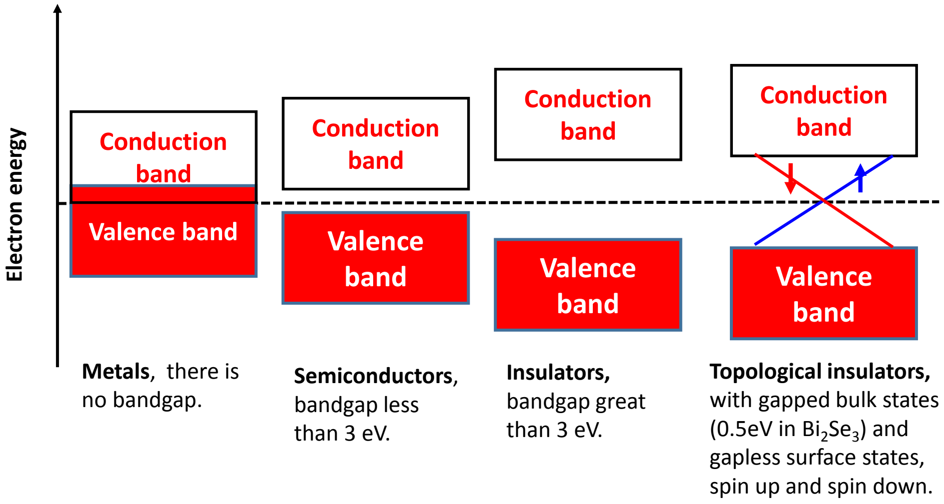

Figure 1.1: Schematic band structure for metals, semiconductors, insulators and topological insulators.

Although, up to now, no topological states have been realized in monolayer graphene, graphene systems have many exotic properties similar to those possessed by topological materials such as high Fermi velocity, 0.85×10^6 m/s [9, 10], giant instrinsic mobility and super mechanical properties [11]. Its conduction band and valence band cross each other in the momentum space, forming a Dirac cone. The energy-momentum dispersion near the Dirac cone is linear, and the corresponding electrons obey the Dirac equation [12]. Additionally, graphene has a rather simple crystal structure containing two carbon atoms in the primitive unit cell. In this sense, graphene provides a wonderful platform to investigate Dirac Fermions.

1.1 Dirac Fermions in graphene

Graphene, a 2D carbon material, has a hexagonal crystal structure shown in Fig. 1.2. In every vertex of the hexagons, there is a carbon atom. The unit cell is outlined by black lines, which contains two carbon atoms. The lattice environment of the two atoms are different from each other. The lattice vectors are given as $\mathbf{a}_1 = \frac{a}{2}(3, \sqrt{3})$ and $\mathbf{a}_2 = \frac{a}{2}(3, -\sqrt{3})$, where $a = 1.42$ Å is the distance between a pair of the nearest atoms. The band structure of graphene can be calculated by using the first-principles calculations. Here, within the framework of density functional theory, the first-principles calculations code of VASP [13] (Vienna Ab *initio* Simulation Package) is employed to conduct the band structure calculations. The exchange and correlation potentials are depicted by the generalized gradient approximation (GGA) [14] of Perdew-Burke-Ernzerhof (PBE). The energy cutoff and k-mesh are chosen to balance accuracy against computational time [15, 16]. Here we use 550 eV as cutoff energy and (21×21×1) as k-mesh.

The calculated band structure is shown in Fig. 1.3(a). It has linear dispersion at low energy from -1 eV to 1 eV, near the Dirac point K, and has nonlinear dispersion at high energies. Fig. 1.3(b) is a zoomed portion of the band structure at low energy where the points are calculated results and lines are fitted functions, $y = b_1 x + b_2$. Fitting parameters are used to evaluate the Fermi velocity and the hopping parameter via the following equations [17, 18]

$$E = pv_F = \hbar k v_F, \tag{1.1}$$

$$t = \frac{2\hbar v_F}{\sqrt{3}a}. \tag{1.2}$$

The evaluated Fermi velocity (v_F) and hopping energy (t) are 0.85×10^6 m/s and 2.6 eV, respectively, agreeing with previous results [9, 10]. In fact, the Fermi velocity of graphene can be modified by varying the charge carrier concentration up to 3.0×10^6 m/s [18]. Therefore the Fermi velocity of graphene is usually set to 1.0×10^6 m/s with hopping energy 3.0 eV or 2.7 eV in the tight-binding model in order to simplify calculations [19].

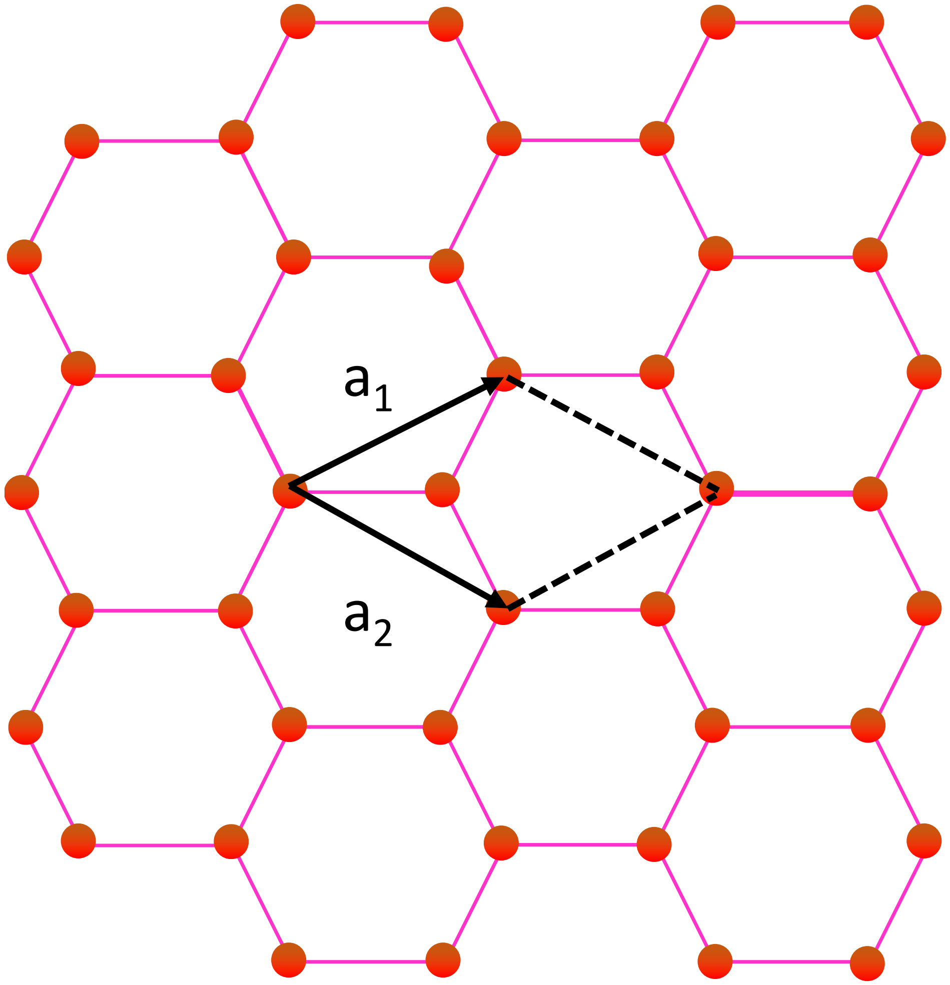

Figure 1.2: A schematic crystal structure for graphene, where black lines outline a unit cell containing two carbon atoms. Lattice vectors are given as $\mathbf{a}_1 = \frac{a}{2}(3, \sqrt{3})$ and $\mathbf{a}_2 = \frac{a}{2}(3, -\sqrt{3})$, where $a = 1.41$ Å is the distance between a pair of the nearest atoms.

In the tight-binding model, the effective Hamiltonian of graphene is given by

$$H = \begin{pmatrix} 0 & h(\boldsymbol{k}) \\ h^*(\boldsymbol{k}) & 0 \end{pmatrix},$$

where $h(\boldsymbol{k}) = t[1 + \mathrm{e}^{-i\boldsymbol{k}\boldsymbol{a_1}} + \mathrm{e}^{-i\boldsymbol{k}\boldsymbol{a_2}}]$ with lattice vectors $\boldsymbol{a}_1$ and $\boldsymbol{a}_2$ shown in Fig. 1.2; t is the hopping energy that has been obtained via the first-principles calculations. By diagonalizing the effective Hamiltonian, the eigenvalues are obtained by

$$\epsilon_{\pm}(\boldsymbol{k}) = \pm t\sqrt{1 + 4\cos(\frac{3k_x a}{2})\cos(\frac{\sqrt{3}k_y a}{2}) + 4\cos^2(\frac{\sqrt{3}k_y a}{2})}. \tag{1.3}$$

According to the equation, band structure of graphene is plotted in Fig. 1.4, where six

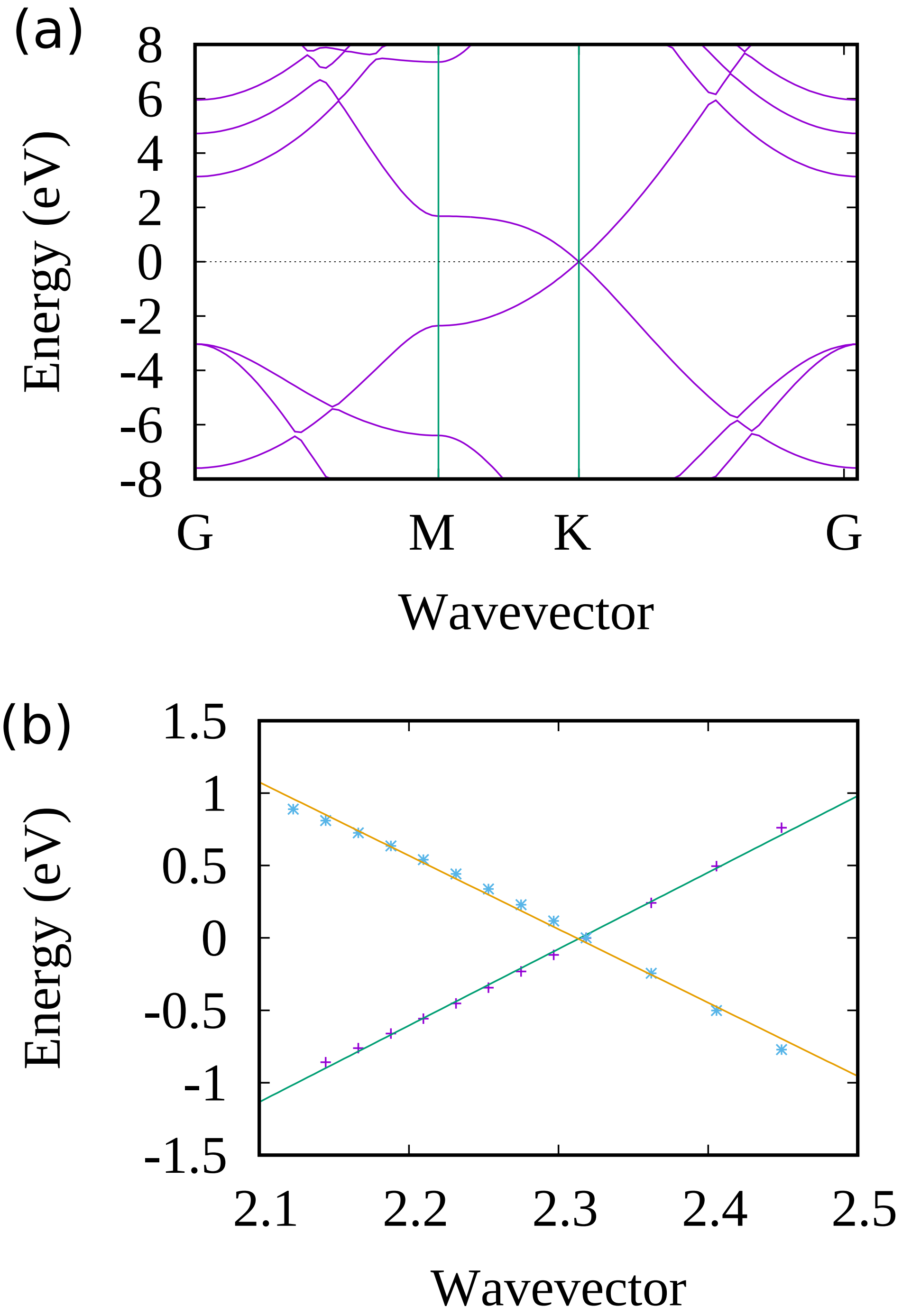

Figure 1.3: The top panel is the band structure of graphene with a linear energy-momentum dispersion near Dirac point K; the bottom panel is a part of band structure near Dirac point where the points are calculated results and lines are fitted functions, $y = b_1x + b_2$.

Dirac cones are observed. Let $\epsilon_{\pm} = 0$, the position of the six Dirac cones is obtained by, $\boldsymbol{K}_1(\frac{2\pi}{3a},\frac{2\pi}{3\sqrt{3}a})$, $\boldsymbol{K}_2(\frac{2\pi}{3a},\text{-}\frac{2\pi}{3\sqrt{3}a})$, $\boldsymbol{K}_3(-\frac{2\pi}{3a},\text{-}\frac{2\pi}{3\sqrt{3}a})$, $\boldsymbol{K}_4(-\frac{2\pi}{3a},\frac{2\pi}{3\sqrt{3}a})$, $\boldsymbol{K}_5(0,\frac{4\pi}{3\sqrt{3}a})$, $\boldsymbol{K}_6(0,\text{-}\frac{4\pi}{3\sqrt{3}a})$.

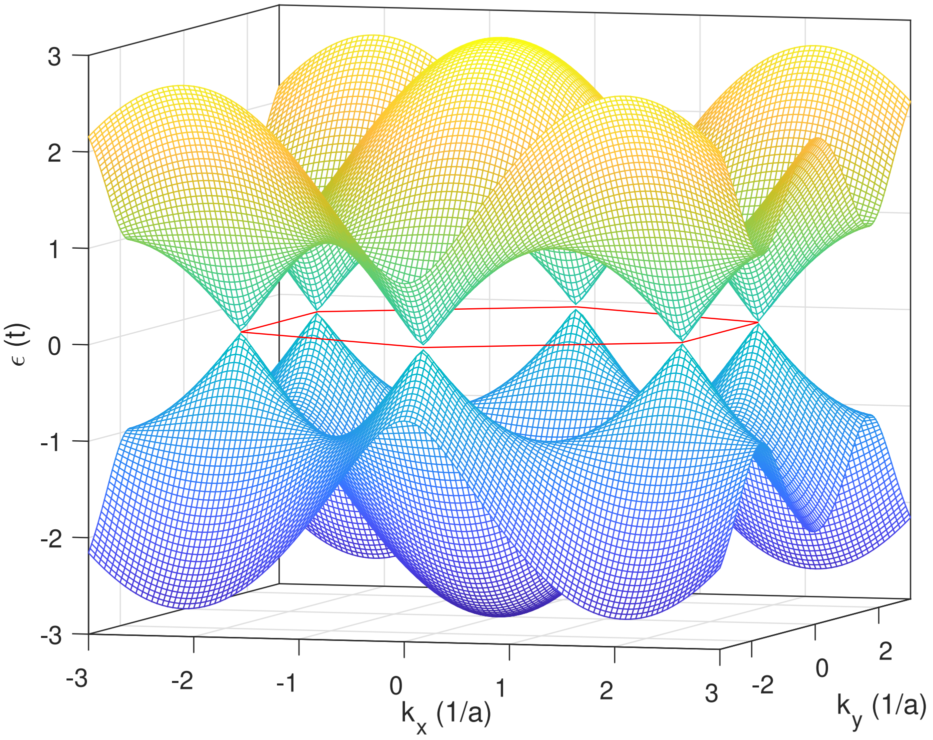

Figure 1.4: Band structure of graphene plotted according to Eq. 1.3.

Now, we shift the coordinate to the $\boldsymbol{K}_1$ point i.e., $\boldsymbol{k'} = \boldsymbol{k} + \boldsymbol{K}_1$ and expand $\epsilon_\pm(\boldsymbol{k'} - \boldsymbol{K}_1)$ up to the first order in $\boldsymbol{k'}$, which results in $E_\pm = \frac{3a}{2}\sqrt{k_x^2 + k_y^2} = \frac{3a}{2}|k| = \hbar k v_F$. In this sense, graphene has a linear low energy-momentum dispersion at the vicinity of Dirac cones and the corresponding electrons obey the Dirac equation.

1.2 Dirac Materials

Dirac materials are a new type of material whose low-energy fermionic excitations obey the Dirac equation instead of the Schrödinger equation and behave as massless Dirac particles. Dirac materials can be classified into several types such as graphene, topological insulators, Dirac semimetals, Weyl semimetals, nodal-ring semimetals and so on [20].

Here, we give a brief introduction to 3D Dirac semimetals, 3D Weyl semimetals and

3D nodal-ring semimetals. For 3D Dirac semimetals, the low energy properties can be characterized by

$$\boldsymbol{H} = v\boldsymbol{\sigma}\boldsymbol{k}, \tag{1.4}$$

where $\boldsymbol{k} = k_x\hat{\imath} + k_y\hat{\jmath} + k_z\hat{k}$ is wave vector, v is the Fermi velocity and $\boldsymbol{\sigma}$ is Pauli matrices defined by

$$\boldsymbol{\sigma} = \sigma_x\hat{\imath} + \sigma_y\hat{\jmath} + \sigma_z\hat{k}, \tag{1.5}$$

$$\sigma_x = \begin{pmatrix} 0 & 1 \\ 1 & 0 \end{pmatrix},$$

$$\sigma_y = \begin{pmatrix} 0 & -i \\ i & 0 \end{pmatrix},$$

$$\sigma_z = \begin{pmatrix} 1 & 0 \\ 0 & -1 \end{pmatrix}.$$

Dot product of $\boldsymbol{\sigma}\boldsymbol{k}$ is given by

$$\boldsymbol{\sigma}\boldsymbol{k} = \sigma_x k_x + \sigma_y k_y + \sigma_z k_z = \begin{pmatrix} k_z & k_x - ik_y \\ k_x + ik_z & -k_z \end{pmatrix}. \tag{1.6}$$

Due to time-reversal (TR) or inversion symmetry, Dirac nodes are double degenerate. If the degeneracy is eliminated by either breaking time-reversal or inversion symmetry, a Dirac node will separate into two-component Weyl nodes. This kind of topological state is named as Weyl semimetals. The low energy of a single Weyl node can be described by the Hamiltonian [21],

$$\boldsymbol{H} = b_0\boldsymbol{I} + v\boldsymbol{\sigma}(\boldsymbol{k} - \boldsymbol{b}). \tag{1.7}$$

where $\boldsymbol{I}$ is a 2×2 identity matrix, b_0 (a scalar) and $\boldsymbol{b}$ (a three-dimensional vector) are the energy and momentum shift respectively. For a Weyl node, a small perturbation can not open a gap because all three Pauli matrices are used. Thus Weyl semimetals is a stable phase. Similar to other kinds of topological materials, Weyl semimetals have protected surface states as well as exotic electromagnetic response.

In Dirac and Weyl semimetals, the conduction band and valence band cross each other at the Fermi level and form Dirac cones. The number of these Dirac cones is finite and usually equals two due to spin degeneracy. If the number becomes infinite, then a new type of material emerges called nodal semimetals. If the Dirac cones form a continuous circle, the nodal semimetals are called nodal-Ring semimetals.

We have mentioned semimetals many times without explaining. Semimetals refer to materials whose conduction band and valence band touch each other at the Fermi level and whose density of states is zero at the Fermi level. In this sense, materials with Dirac cones are usually semimetals.

1.3 Thermionic emission

Thermionic emission is a fundamental process whereby electrons are driven by thermal energy to escape from bulk states, shown in Fig. 1.5(a). In metals and semiconductors, states near the Fermi level are filled with electrons. When the electrons obtain enough thermal energy, they cross the surface barrier (W) resulting in thermionic emission, shown in Fig. 1.5(b). Thermionic emission has been extensively studied in conventional semiconductors with a parabolic energy-momentum dispersion due to its potential applications in thermionic devices such as refrigerators and energy generators [22–24]. The practical applications of thermionic devices are seriously hindered by the lack of low work-function materials [25] and the space charge effect [26], which makes thermionic emission receive decreasing attention from researchers. However, thanks to the recent technological developments in obtaining low work-function materials and the discovery of new materials such as graphene and Dirac semimetals [27–31], thermionic emission now receives increasing attention [32, 33]. For conventional semiconductors, the thermionic emission current (TEC) is described by a universal equation, called Richardson-Dushman law $J_{RD} = A_{RD}T^2\mathrm{e}^{-W/k_BT}$, where $A_{RD} = \frac{qmk_B^2}{2\pi^2\hbar^3} = 120\ \mathrm{Acm}^{-2}\mathrm{K}^{-2}$, q is the absolute charge of an electron, m is the mass of an electron, k_B is the Boltzmann constant, $\hbar$ is the reduced Plank constant, T is the dynamical temperature and W is the work-function of the material [25]. Electrons in graphene obey the Dirac equation instead of the Schrödinger equation, which results in graphene possessing unique properties. One such property is that the TEC of graphene is found to be different to the universal equation, and is instead given as $J_G = A_G T^2 \mathrm{e}^{-W/k_B T}$, where $A_G = \frac{q k_B T}{\pi^2 \hbar^3 v_F^2}$ and v_F is the Fermi velocity [34]. Low energy electrons in graphene are massless particles resulting in A_G is also being mass-independent. Possessing a high Fermi velocity ($v_F \sim 10^6$ m/s) is another feature of graphene, which appears in A_G. As we have mentioned, graphene is an atomically thin 2D material. Therefore, its density of states is much smaller than that of 3D conventional materials resulting in a smaller $A_G \approx 0.02$ A/cm^{-2}K^{-2} [35].

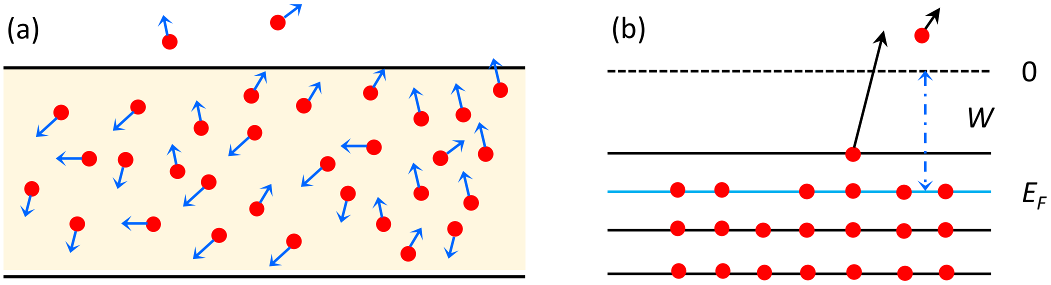

Figure 1.5: Schematic of thermionic emission: (a) electrons are evaporated from a material to vacuum driven by thermal energy, (b) corresponding energy level. States near the Fermi level are filled with electrons. When the electrons obtain enough thermal energy, they cross the surface barrier (W) resulting in thermionic emission.

We follow in Richardson's footsteps to derive the Richardson-Dushman equation in conventional semiconductors. Thermionic current density can be calculated by

$$J_R = \int q n(E) v_z(E) \mathrm{d}E, \tag{1.8}$$

where q is the charge of an electron, $n(E)$ is the density of electrons and $v_z(E)$ is the velocity of the electrons along the barrier direction. We assume the barrier direction is the z direction. The density of electrons can be evaluated by

$$n(E) = N(E) f(E). \tag{1.9}$$

Here $f(E) = \frac{1}{\mathrm{e}^{\beta(E-E_F)}+1}$ is the Fermi function. The Fermi-Dirac distribution can be replaced by the Maxwell-Boltzmann distribution $F(E) = \mathrm{e}^{-\beta(E-E_F)}$ by assuming $E - E_F > 3k_B T$. The assumption is reasonable if the work function W is greater than $3k_B T$ (about 90 meV at $T = 350$ K). It is important to make this assumption since it helps to obtain the thermionic current density analytically. $N(E)$ is density of states and $\beta = 1/(k_B T)$. To evaluate J_z, we need to know $N(E)$ and v_z. These two terms are closely related to energy-momentum dispersion.

Conventional semiconductors refer those materials having a parabolic energy momentum dispersion,

$$E = \frac{\hbar^2 k^2}{2m}. \tag{1.10}$$

The density of states $N(E)$ can be evaluated by using the following equation

$$N(E) = \frac{\mathrm{d}Z(E)}{V\mathrm{d}E}, \tag{1.11}$$

where $Z(E)$ is the total energy states giving as

$$Z(E) = 2\rho(k)\frac{4}{3}\pi k^3 = 2 \times \frac{V}{8\pi^3} \times \frac{4}{3}\pi k^3, \tag{1.12}$$

where factor 2 comes from spin up and spin down. By combining Eq. 1.10 and Eq. 1.12, $Z(E)$ can be written as

$$Z(E) = 2 \times \frac{V}{8\pi^3} \times \frac{4}{3}\pi\frac{(2mE)^{3/2}}{\hbar^3} = \frac{V(2mE)^{3/2}}{3\pi^2\hbar^3}. \tag{1.13}$$

Finally, the density of states is obtained by

$$N(E) = \frac{\mathrm{d}Z(E)}{V\mathrm{d}E} = \frac{(2m)^{3/2}}{2\pi^2\hbar^3}\sqrt{E}. \tag{1.14}$$

In some books, $m^{3/2}$ is denoted as m^*. Additionally, the energy can be related to velocity by following equation,

$$E = \frac{1}{2}mv^2 = \frac{1}{2}m(v_x^2 + v_y^2 + v_z^2). \tag{1.15}$$

Based on the above equations, the current density of 3D conventional materials can be calculated by

$$\begin{aligned} J_R &= \int q\frac{(2m)^{3/2}}{2\pi^2\hbar^3}\sqrt{E}f(E)v_z\mathrm{d}E = \int q\frac{(2m)^{3/2}}{2\pi^2\hbar^3}\sqrt{\frac{m}{2}}vf(E)v_z mv\mathrm{d}v \\ &= \frac{qm^3}{4\pi^3\hbar^3}f(E)\int v_z 4\pi v^2 dv = \frac{qm^3}{4\pi^3\hbar^3}\int_{-\infty}^{+\infty}\int_{-\infty}^{+\infty}\int_{v_{z,min}}^{+\infty} f(E)v_z\mathrm{d}v_x\mathrm{d}v_y\mathrm{d}v_z. \end{aligned} \tag{1.16}$$

Inserting $f(E)$ into the above equation, J_R can be written as,

$$\begin{aligned} J_R = \frac{qm^3}{4\pi^3\hbar^3}e^{\beta q E_F}\int_{-\infty}^{+\infty} e^{-0.5\beta m v_x^2}dv_x \int_{-\infty}^{+\infty} e^{-0.5\beta m v_y^2}dv_y \int_{v_{z,min}}^{+\infty} \\ \times v_z e^{-0.5\beta m v_z^2}dv_z. \end{aligned} \tag{1.17}$$

Here the integrals over x, y and z are independent of each other. Therefore they can be integrated separately. The integral over x and y is obtained by using the following equation

$$I = \int_{-\infty}^{\infty} e^{-x^2} dx = \sqrt{\pi}. \tag{1.18}$$

The integral can be easily evaluated as,

$$\begin{aligned} I^2 &= \int_{-\infty}^{\infty} e^{-x^2} dx \int_{-\infty}^{\infty} e^{-y^2} dy = \int_{-\infty}^{\infty} e^{-r^2} 2\pi r dr \\ &= \pi \int_{-\infty}^{\infty} e^{-r^2} dr^2 = \pi. \end{aligned} \tag{1.19}$$

Before performing the integral over z direction, $v_{z,min}$ should be determined. $v_{z,min}$ is the minimum speed of electrons in z direction, which makes the electrons have enough energy to escape from bulk states to free space. It can be determined by

$$E_{min} = W + E_F = \frac{1}{2} m v_{z,min}^2. \tag{1.20}$$

After some algebraic calculations, the thermionic current density is obtained by

$$J_R(W, T) = \frac{q m k_B^2}{2\pi^2 \hbar^3} T^2 e^{-W\beta} = A_R T^2 e^{-W\beta}. \tag{1.21}$$

where T is the temperature, m is the mass of an electron, k_B is the Boltzmann constant, $\hbar$ is the reduced plank constant, $\beta = 1/(k_B T)$ and $A_R \approx 120$ A cm^{-2} K^{-2} is Richardson's constant.

Recently, the thermionic properties of graphene have been investigated both experimentally [30] and theoretically [34]. The results showed the mass-dependent Richardon-Dushman equation no longer holds for graphene due to the massless energy dispersion, $E = \hbar k v_F$, where v_F is the Fermi velocity. A modified thermionic law was established by assuming graphene to have a linear energy-momentum dispersion within the layer and a parabolic energy-momentum dispersion in the perpendicular direction [29, 34]

$$J_G(W, T) = \frac{q k_B^3 T}{\pi^2 \hbar^3 v_F^2} T^2 e^{-W\beta} = A_G T^2 e^{-W\beta}, \tag{1.22}$$

where A_G is the modified RD constant for graphene. The modified RD law is mass independent. The main difference between graphene and conventional materials is that A_G has a linear temperature dependence. The work function of graphene extracted by the above equation agrees well with results in literature [36,37]. Based on the modified law, graphene-based thermionic devices have been further investigated [29,38].

Although free-standing single-layer graphene has high electron mobility, its thermionic emission ability is limited due to the small density of states and its emission ability would be affected by substrates. Three dimensional Dirac semimetals have similar electronic properties to graphene such as a linear energy-momentum dispersion in low energy region. The density of states of 3D materials is larger than that of 2D materials. Based on the above two factors, the thermionic properties of 3D semimetals should be better than that of graphene. Besides, research showed Cd_3As_2 [39–41] has an unexpectedly low thermal conductivity and extraordinary performance in thermoelectric devices [42].

1.4 Thesis review

Two major topics are investigated in this thesis, namely, thermionic emission in Dirac systems and the transport properties of Dirac systems.

On the topic of thermionic emission, we have investigated:

- Thermionics in Dirac semimetals (Chapter 2).
- Thermionics in nodal-ring semimetals (Chapter 3).
- Thermionic cooling enhanced heat transfer in Dirac semimetals (Chapter 4).

On the topic of transport properties of Dirac systems, we have investigated:

- Hot carrier relaxation in gapped Dirac semimetals (Chapter 5).
- Non-linear electromagnetic response in Semi-Dirac semimetals (Chapter 6).

Chapter 2

Thermionics in Dirac semimetals

* In this chapter, we investigate the thermionics in three dimensional Dirac materials. We demonstrate that 3D Dirac semimetals have advantages over conventional semiconductors and graphene in thermionic applications. The low emission current suffered in graphene due to the vanishing density of states is enhanced by an increased group velocity in 3D Dirac materials. Furthermore, the thermal energy carried by electrons in 3D Dirac semimetals is twice of that in conventional materials. As a result, 3D Dirac semimetals have the best thermal efficiency and coefficient of performance when compared to conventional semiconductors and graphene. The generalized Richardson-Dushman (RD) law in 3D Dirac semimetals is derived. The law exhibits an interplay of the reduced density of states and enhanced emission velocity.

2.1 Introduction

Nowadays, global warming is a serious problem that threatens the future of all human beings. Another similar problem is air pollution. There is no doubt that these problems are caused by burning fossil fuels. After the Second World War, the global population has been continually increasing, and industrialization in developing nations is considerably speeding up. As a result, uncountable fossil fuels are burned day in and day out to drive our cars, heat our homes and keep our factories running. There are two

---

* This chapter is based on S Huang, M Sanderson, Y Zhang Y and C Zhang., High efficiency and non-Richardson thermionics in three dimensional Dirac materials., Applied Physics Letters, 111 (2017) 183902.

main approaches in science to solve the problems caused by burning fossil fuels. The first approach is developing clean and renewable energy to replace fossil fuels. Solar energy is the most promising renewable one. Fossil fuels are also a kind of solar energy that came from the sun several million years ago. The second approach is to improve the energy conversion efficiency. Traditional energy conversion devices such as steam engines and turbofan engines are mechanical devices that produce noise and lose energy due to moving parts. Energy conversion devices that do not have moving parts are one of the potential candidates to improve conversion efficiency.

Energy conversion devices based on electron (or hole) transport have no moving parts, and have been continually researched for more than 100 years. There are two conversion mechanisms; thermoelectrics (TE) and thermionics. Both realize energy conversion between heat and electricity. Thermoelectric materials are characterized by the merit, defined as $ZT = S^2\sigma T(\kappa_L + \kappa_e)^{-1}$, where S is the Seebeck coefficient, σ is the electrical conductivity, T is the temperature, and κ_L (lattice) and κ_e (electronic) are thermal conductivities. The relatively low thermodynamic efficiency of commonly used TE materials has prevented their use in large-scale applications. Advancements of TE materials and devices requires finding materials with a high S, a high σ, and low κ_L and κ_e. The bottleneck is that these quantities are intrinsically connected, as a good electrical conductor is normally a good thermal conductor, thus making further improvement of ZT of bulk materials extremely difficult. Moreover, κ_L of a solid has an amorphous limit [43–46]. Recent developments in nanotechnology allow further reduction of κ_L by using material design, crystal structure design [43, 44, 47, 48] and nanostructuring [45, 49–52], nano-precipitation in PbTe [52] nano-grained Bi_2Te_3 [45, 52], and liquid-like ions in Zn_4Sb_3 [44] and Cu_2Se [43]. These approaches have been the focus of thermoelectric research in the last few decades and have resulted in an increase of peak ZT to 1.5 and higher. Research shows that a high band degeneration [53–55], a low band effective mass [56], and weak scattering strength [57] can lead to an increase in ZT.

Thermionic generators or coolers operate by using two parallel metal electrodes. When the two metals have different temperatures, electrons in the hot metal flow across the barrier into the cold metal, establishing an electrical current. They differ from thermoelectric devices in the way particles travel. In thermoelectric devices, electrons travel diffusively. In thermionic devices, the barrier between the hot and cold regions of the device is shorter than the distance between collisions for electrons, so electrons travel ballistically. The efficiency of both thermoelectric and conventional thermionic devices is lower than the theoretical upper limit, known as Carnot efficiency, for all finite barrier heights [58]. The basic structure of the thermionic cooler consists of two planar electrodes separated by a potential barrier (shown in Fig. 2.1). If there is no external voltage, high energy electrons in the hot side will move to the cold side due to the thermionic effect. In this case, the device can act as a thermionic generator. If there is a moderate external voltage, the work function of the cold side will be reduced and the work function of the hot side will be raised. As a result, high energy electrons in the cold side move to the hot side and electrons in the hot side can not move to the cold side resulting in a cooling effect. Hence the device act as a thermionic cooler.

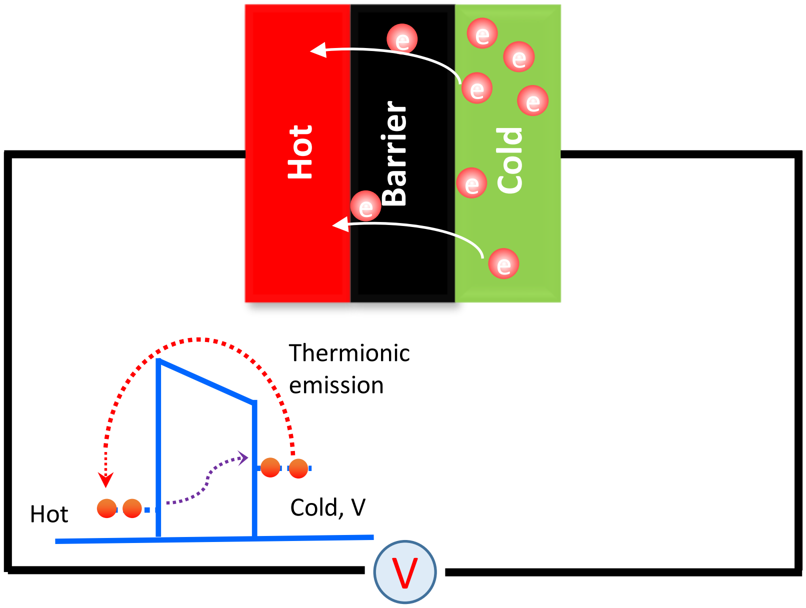

Figure 2.1: Schematic of a thermionic device and the potential energy of an electron in the device. The external voltage reduces the work function of the cold side and raises the work function of the hot side. As a result, high energy electrons in the cold side move to the hot side and electrons in the hot side can not move to the cold side resulting in a cooling effect.

Conventional semiconductor materials were considered as a promising candidate for thermionic devices due to their relatively low work functions. The science of thermionics and its potential application in integrated cooling of electronic and optoelectronic devices has attracted considerable interest. Unfortunately, thermionic materials with a low enough work function are still unavailable.

Newly discovered materials with a linear energy-momentum dispersion such as graphene [59], topological insulators [8] and Dirac semimetals [60] have attracted enormous attention in the past decade. These materials exhibit an incredibly high mobility, strong optical absorption, and fast response, etc. These properties made this class of Dirac materials a promising candidate for applications in electronics and photonics [1,61,62]. However, energy transport in these materials would be less significant because of the zero mass nature of charge carriers. In this chapter, we shall demonstrate that while the thermal emission current of Dirac materials is less than that of conventional materials, and their thermal efficiency is higher compared to that of conventional materials.

2.2 Thermionic current density

For 3D semimetals, the mass-dependent Richardson-Dushman equation that has been discussed in Section 1 no longer holds due to their special energy-momentum dispersions (linear and mass-independent). The energy momentum dispersion is given by

$$E = \hbar k v_F. \tag{2.1}$$

Their total energy states $Z(E)$ can be calculated by

$$Z(E) = 2 \times \frac{V}{8\pi^3} \times \frac{4}{3}\pi k^3 = \frac{V}{3\pi^2}\frac{E^3}{\hbar^3 v_F^3}. \tag{2.2}$$

The density of states $N(E)$ and the density of electrons $n(E)$ in the unit of energy and volume are obtained by

$$N(E) = \frac{\mathrm{d}Z(E)}{V\mathrm{d}E} = \frac{E^2}{\pi^2\hbar^3 v_F^3}, \tag{2.3}$$

$$n(E) = N(E)f(E) = \frac{E^2}{\pi^2\hbar^3 v_F^3} \times \frac{1}{1+\mathrm{e}^{\beta(E-E_F)}} \approx \frac{E^2}{\pi^2\hbar^3 v_F^3} e^{\beta E_F} e^{-\beta E}. \tag{2.4}$$

The energy of electrons can be related to velocity v by

$$v_z = \frac{\partial H}{\partial p_z} = \frac{v_F k_z}{k} = \frac{v_F k_z}{\sqrt{k_x^2 + k_y^2 + k_z^2}}. \tag{2.5}$$

By Inserting these equations the into emission current equation $J_D = \int qn(E)v_z(E)\mathrm{d}E$, we obtain

$$J_D = \frac{q\mathrm{exp}(E_F/k_BT)}{\pi^2\hbar}\int kk_z\mathrm{exp}(-\frac{\hbar v_F k}{k_BT})dk = C\int kk_z e^{-ak}dk, \tag{2.6}$$

where $C = \frac{q\mathrm{exp}(E_F/k_BT)}{\pi^2\hbar}$ and $a = \frac{\hbar v_F}{k_BT}$. The integral can be evaluated in spherical coordinates,

$$J_D = C\int kk_z e^{-ak}dk = C\int\int\int k^2\cos(\theta)e^{-ak}\frac{1}{4\pi}\sin(\theta)d\theta d\phi dk. \tag{2.7}$$

Integrating over ϕ

$$\begin{aligned} J_D &= \frac{C}{2}\int_{k_{min}}^{\infty}\int_0^{\theta_{max}} k^2\cos(\theta)e^{-ak}\sin(\theta)d\theta dk \\ &= \frac{C}{4}\int_{k_{min}}^{\infty} k^2 e^{-ak}\int_0^{\theta_{max}}\sin(2\theta)d\theta dk, \end{aligned} \tag{2.8}$$

where $k_{min} = \frac{E_F+W}{\hbar v_F}$ and $\cos^2(\theta_{max}) = \frac{k_{min}}{k}$, which guarantee the electrons to have enough energy to overcome the potential barrier. By Integrating over k and θ, the thermionic current density of 3D semimetals is obtained by

$$\begin{aligned} J_D &= \frac{C}{4}\int_{k_{min}}^{\infty} k^2 e^{-ak}(1-\frac{k_{min}}{k})dk \\ &= \frac{C}{4}(\frac{k_{min}}{a^2}+\frac{2}{a^3})e^{-ak_{min}} = A_D T^2\mathrm{e}^{-W\beta}, \end{aligned} \tag{2.9}$$

with modified Richardson's coefficient

$$A_D = \frac{qk_B^2}{4\pi^2\hbar^3 v_F^2}(W + E_F + 2k_BT). \tag{2.10}$$

While the $J_R = \frac{qmk_B^2}{2\pi^2\hbar^3}T^2\mathrm{e}^{-W\beta}$ is mass dependent, $J_G = \frac{qk_B^3 T}{\pi^2\hbar^3 v_F^2}T^2\mathrm{e}^{-W\beta}$ and J_D are mass independent which stems from the parabolic and linear energy-momentum dispersion. The temperature dependence of the thermionic current densities for conventional materials (J_R), single graphene (J_G) and 3D Dirac semimetals (J_D) are shown in Fig. 2.2, where $E_F = 0.1$ eV and $W = 0.3$ eV for all three systems. J_G is much smaller compared to J_R and J_D. So we plot $10J_G$ in the figure. The figure shows $J_R > J_D > J_G$, which indicates conventional materials having the highest rate of thermionic emission and single layer graphene having the lowest rate. The emission current from a 3D Dirac semimetals is greater than that of graphene by an amount,

$$\Delta J = J_D - J_G = \frac{qk_B^2}{2\pi^2\hbar^3 v_F^2}(W + E_F - 2k_BT)T^2 e^{-W\beta}. \tag{2.11}$$

The negative term $-2k_BT$ comes from the valley degree of graphene. The terms W and E_F have the same form as J_R in terms of the temperature dependence. In the calculation of J_G, the carriers are assumed to have a linear energy dispersion in the direction perpendicular to the emission direction and a parabolic dispersion in the emission direction. The current is relatively smaller than J_R. The energy dispersion of 3D Dirac semimetals is linear in all directions. We analyze this change by considering both the density of states and the group velocity of emitted electrons. The emission current increases with both the density of states and the emission velocity. When the in-plane energy dispersion changes from parabolic to linear, the density of states is significantly reduced near the bottom of the conduction band. This is the origin of J_G being much smaller than J_R. On the other hand the group velocity of the emitted electrons along the emission direction, given by $\partial E/\partial k_z$ increases when the energy dispersion along the k_z-direction changes from parabolic to linear. For a parabolic dispersion, the group velocity goes to zero as k_z goes to zero. For linear dispersion, the group velocity can be finite when k_z goes to zero if k_x and k_y both go to zero. In the case of 3D Dirac semimetals, the enhancement of group velocity along the emission direction compensates the vanishing in-plane density of states. Our result indicates that the materials with the highest emission current would be those with a parabolic in-plane energy dispersion and linear energy dispersion along the emission direction.

2.3 Thermionic energy flow density

In the previous section, we have derived a modified Richardson's equation to describe the thermionic charge current density in 3D Dirac semimetals. In the present section, we are going to show how to describe the energy flow in 3D Dirac semimetals. To see the difference in energy flow between conventional materials and Dirac semimetals, we revisit the energy flow in a conventional material. Thermionic energy flow and current density are both carried by electrons, which makes them rather similar to each other. The charge carried by an electron is q, while the net energy carried by an electron is $E = \frac{1}{2}m(v_x^2 + v_y^2 + v_z^2) - E_F$. Therefore, thermionic energy flow can be obtained by

$$Q_R = \int \frac{E}{q} qn(E)v_z(E)\mathrm{d}E, \tag{2.12}$$

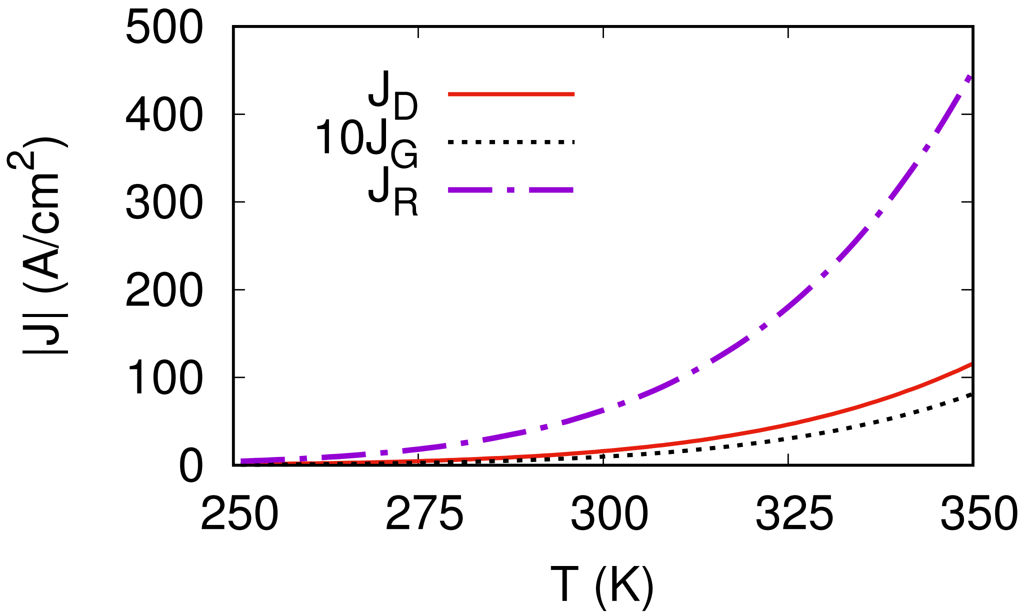

Figure 2.2: Temperature dependence of thermionic current density (absolute value) for conventional materials (J_R), single-layer graphene (J_G) and 3D Dirac materials (J_D), where $E_F = 0.1$ eV and $W = 0.3$ eV. In addition, we plot $10J_G$ instead of J_G to make it visible.

where $n(E) \approx \frac{E^2}{\pi^2\hbar^3 v_F^3}\mathrm{e}^{\beta E_F}\mathrm{e}^{-\beta E}$ is the electron density states for 3D conventional materials which has been already obtained in the previous section. Inserting everything in, the energy flow can be written as

$$\begin{aligned} Q_R = \frac{qm^3}{4\pi^3\hbar^3}e^{\beta E_F}\int_{-\infty}^{+\infty}\int_{-\infty}^{+\infty}\int_{v_{z,min}}^{+\infty}\frac{m(v_x^2+v_y^2+v_z^2)-2E_F}{2q} \\ \times\, e^{-0.5\beta m(v_x^2+v_y^2+v_z^2)}v_z\mathrm{d}v_x\mathrm{d}v_y\mathrm{d}v_z = A_x + A_y + A_z - \frac{E_F}{q}J_R. \end{aligned} \tag{2.13}$$

Where A_x , A_y and A_z are given by

$$\begin{aligned} A_x = \frac{m^4}{8\pi^3\hbar^3}e^{\beta E_F}\int_{-\infty}^{+\infty}\int_{-\infty}^{+\infty}\int_{v_{z,min}}^{+\infty} v_x^2 v_z \\ \times\, e^{-0.5\beta m(v_x^2+v_y^2+v_z^2)}\mathrm{d}v_x\mathrm{d}v_y\mathrm{d}v_z, \end{aligned} \tag{2.14}$$

$$\begin{aligned} A_y = \frac{m^4}{8\pi^3\hbar^3}e^{\beta E_F}\int_{-\infty}^{+\infty}\int_{-\infty}^{+\infty}\int_{v_{z,min}}^{+\infty} v_y^2 v_z \\ \times\, e^{-0.5\beta m(v_x^2+v_y^2+v_z^2)}\mathrm{d}v_x\mathrm{d}v_y\mathrm{d}v_z, \end{aligned} \tag{2.15}$$

$$\begin{aligned}A_z = \frac{m^4}{8\pi^3\hbar^3}e^{\beta E_F}\int_{-\infty}^{+\infty}\int_{-\infty}^{+\infty}\int_{v_{z,min}}^{+\infty} v_z^3 \\ \times e^{-0.5\beta m(v_x^2+v_y^2+v_z^2)}\mathrm{d}v_x\mathrm{d}v_y\mathrm{d}v_z.\end{aligned} \tag{2.16}$$

Since the integral variables x, y and z are independent of each other. Therefore they can be integrated separately.

$$\begin{aligned}A_x &= \frac{m^4}{8\pi^3\hbar^3}\mathrm{e}^{\beta E_F}\int_{-\infty}^{+\infty} v_x^2 e^{-0.5\beta m v_x^2}\mathrm{d}v_x\int_{-\infty}^{+\infty} e^{-0.5\beta m v_y^2}\mathrm{d}v_y \\ &\times \int_{v_{z,min}}^{+\infty} v_z e^{-0.5\beta m v_z^2}\mathrm{d}v_z = \frac{m^4}{8\pi^3\hbar^3}\mathrm{e}^{\beta E_F}\frac{\sqrt{\pi}}{2}a^3\sqrt{\pi}a\frac{a^2}{2}\mathrm{e}^{-v_{z,min}^2/a^2} \\ &= \frac{qmk_B^2}{2\pi^2\hbar^3}T^2\mathrm{e}^{-W\beta}\times\frac{k_BT}{2q} = \frac{k_BT}{2q}J_z,\end{aligned} \tag{2.17}$$

$$\begin{aligned}A_z &= \frac{m^4}{8\pi^3\hbar^3}e^{\beta E_F}\int_{-\infty}^{\infty} e^{-0.5\beta m v_x^2}\mathrm{d}v_x\int_{-\infty}^{\infty} e^{-0.5\beta m v_y^2}\mathrm{d}v_y\int_{v_{z,min}}^{\infty} v_z^3 e^{-0.5\beta m v_z^2}\mathrm{d}v_z \\ &= \frac{m^4}{8\pi^3\hbar^3}e^{\beta E_F}\sqrt{\pi}a\sqrt{\pi}a\frac{1}{2}a^4(\frac{v_{z,min}^2}{a^2}+1)\mathrm{e}^{-v_{z,min}^2}a^2 \\ &= \frac{qmk_B^2}{2\pi^2\hbar^3}T^2\mathrm{e}^{-W\beta}\frac{(W+E_F+k_BT)}{q} = \frac{(W+E_F+k_BT)}{q}J_z,\end{aligned} \tag{2.18}$$

$$I_1 = \int_{-\infty}^{+\infty} e^{-x^2/a^2}dx = \sqrt{\pi}a, \tag{2.19}$$

$$I_2 = \int_{m}^{+\infty} xe^{-x^2/a^2}dx = \frac{a^2}{2}\mathrm{e}^{-m^2/a^2}, \tag{2.20}$$

$$I_3 = \int_{-\infty}^{+\infty} x^2e^{-x^2/a^2}dx = \frac{\sqrt{\pi}}{2}a^3, \tag{2.21}$$

$$\begin{aligned}I_4 &= \int_{m}^{+\infty} x^3\mathrm{e}^{-x^2/a^2}dx = \frac{1}{2}\int_{m}^{+\infty} x^2\mathrm{e}^{-x^2/a^2}\mathrm{d}x^2 \\ &= \frac{1}{2}a^4(\frac{m^2}{a^2}+1)\mathrm{e}^{-m^2}a^2.\end{aligned} \tag{2.22}$$

Where we have used the standard formulae I_1, I_2, I_3 and I_4, which can be found in the majority of math handbooks or websites. Here $v_{z,min}$ is the minimum speed of electrons in the z-direction, which makes the electrons have enough energy to escape from bulk states to free space. It is determined by

$$E_{min} = W + E_F = \frac{1}{2} m v_{z,min}^2. \tag{2.23}$$

According to the symmetry of integral variables x and y, A_y is equal to A_x. Now we can write down the energy flow in conventional materials as

$$Q_R = A_x + A_y + A_z - \frac{E_F}{q} J_z = \frac{W + 2k_B T}{q} J_z. \tag{2.24}$$

The result can be explained by the average thermal energy per degree of freedom. The average thermal energy per freedom degree in a 1D material with a parabolic energy dispersion can be calculated by

$$\begin{aligned}\bar{E} &= \frac{\int_{-\infty}^{+\infty} E \mathrm{e}^{-\beta E} \mathrm{d}v}{\int_{-\infty}^{+\infty} \mathrm{e}^{-\beta E} \mathrm{d}v} = \frac{\int_{-\infty}^{+\infty} 0.5 m v^2 \mathrm{e}^{-0.5\beta m v^2} \mathrm{d}v}{\int_{-\infty}^{+\infty} \mathrm{e}^{-0.5\beta m v^2} \mathrm{d}v} = 0.5m \frac{\int_{-\infty}^{+\infty} v^2 \mathrm{e}^{-v^2/b^2} \mathrm{d}v}{\int_{-\infty}^{+\infty} \mathrm{e}^{-v^2/b^2} \mathrm{d}v} \\ &= 0.5m \frac{2\,(0.5b)^3 \sqrt{\pi}}{0.5b\sqrt{\pi}} = 0.5 k_B T,\end{aligned} \tag{2.25}$$

where $\beta = 1/(k_B T)$ and $b^2 = 1/(0.5m\beta) = 2k_B T/m$. For 2D and 3D material with a parabolic energy dispersion, the average thermal energy per degree can be calculated in a similar way and the result is also $0.5k_B T$. The result is well known and can be found in thermodynamics books. In 3D thermionic materials, there are four freedom degrees, namely v_x, v_y, v_z and ϕ_z. Therefore the average net energy carried by an electron that jumped over the potential barrier is $2k_B T + W$. Then the thermal energy flow can be written as $\frac{W+2k_B T}{q} J_z$, which agrees with the above result.

Similarly, the energy flow for 3D Dirac semimetals is

$$Q_D = \frac{W + 4k_B T}{q} J_z. \tag{2.26}$$

The term $4k_B T$ is the average energy for four degree of freedoms, which is different from their counterparts $2k_B T$ in conventional materials due to the average energy for one degree of freedom being $0.5k_B T$ in conventional materials and $k_B T$ in Dirac semimetals, which is obtained by

$$< \epsilon >= \hbar v_F \frac{\int_0^\infty k e^{-ak} dk}{\int_0^\infty e^{-ak} dk} = k_B T, \tag{2.27}$$

where $\hbar v_F k$ is the energy of a particle and e^{-ak} is the Maxwell-Boltzmann Distribution.

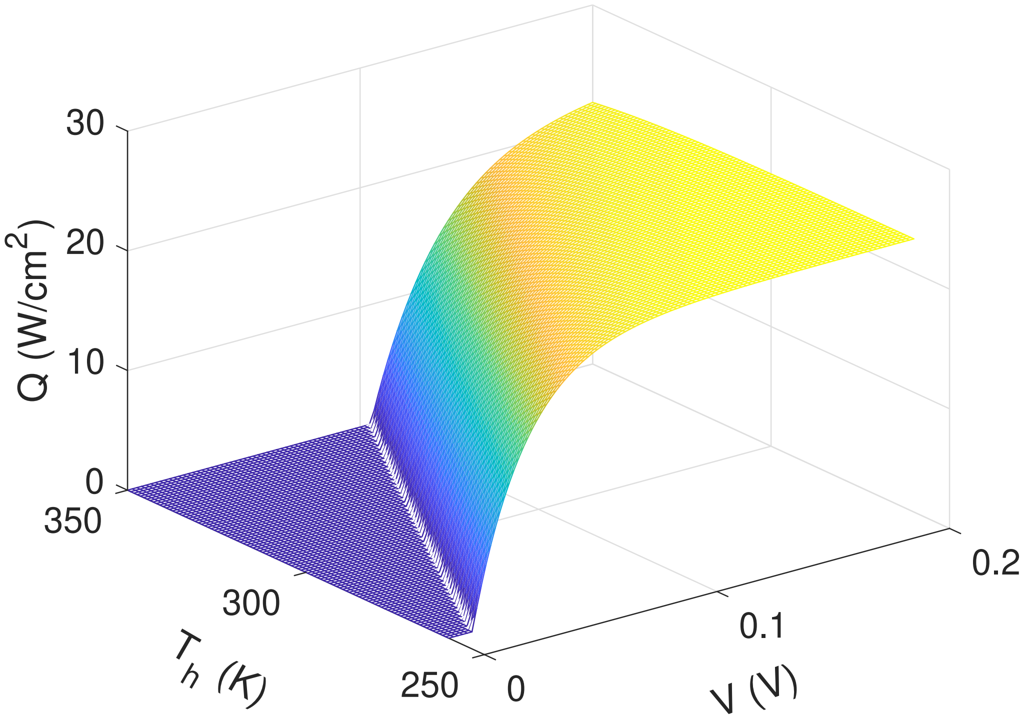

Figure 2.3: Voltage and the hot side temperature dependence of energy flow (Q) where $T_c = 250$ K, $E_F = 0.1$ eV and $W = 0.2$ eV.

2.4 Thermionic refrigerators

Based on the above results, we consider a thermionic refrigerator made up of Dirac semimetals. The net charge current and the net energy current can be written as [25]

$$I = I_c - I_h, \tag{2.28}$$

$$I_c = J_D(W, T_c), \tag{2.29}$$

$$I_h = J_D(W, T_h)e^{qV\beta}, \tag{2.30}$$

$$Q = [(W + 4k_BT_c)I_c - (W + 4k_BT_h)I_h]/q, \tag{2.31}$$

where the positive direction is from the cold side to the hot side.

Voltage and hot side temperature dependence of the energy flow are investigated (shown in Fig. 2.3.). The energy flow is negative when the voltage is absent or small since the energy tends to flow from the hot side to the cold side. Here we have set the negative Q to zero for visual effect (the left corner of Fig. 2.3.). As the voltage increases, Q firstly increases dramatically and then approaches a constant. The reason is that the voltage only weakens the emission ability of the hot side and keeps the cold side unchanged. Hence Q will solely be determined by the cold side and stay constant with the increase of voltage.

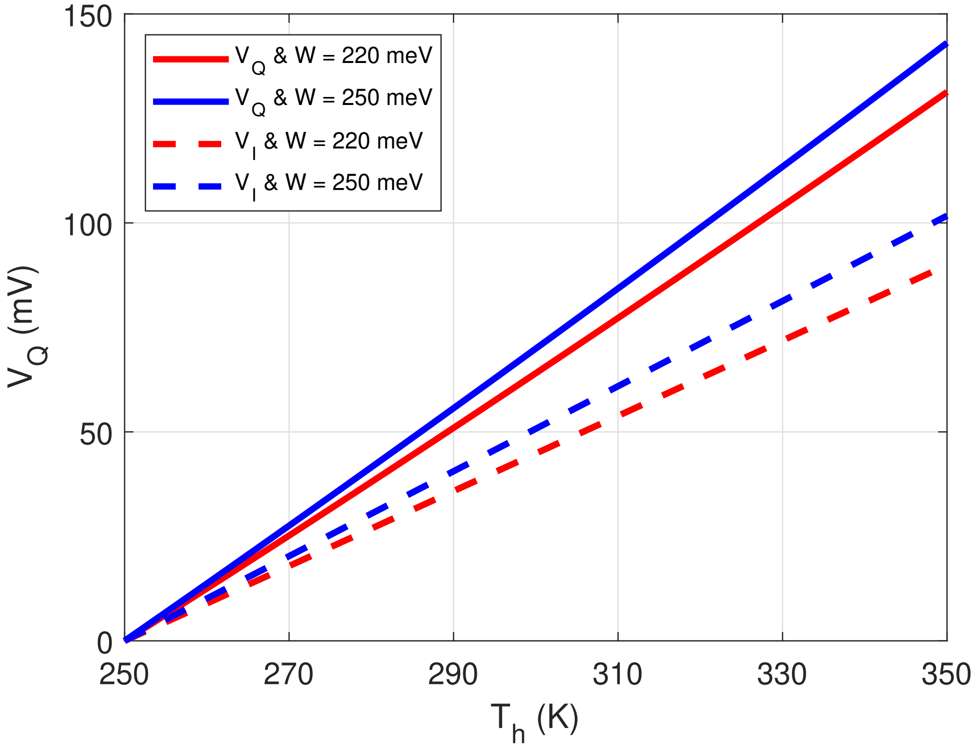

Figure 2.4: The hot side temperature dependence of V_Q and V_I at two different work functions, where $E_F = 0.1$ eV and $T_c = 250$ K.

The threshold voltage that separates the value of Q from negative to positive increases with the hot side temperature due to the rise of the temperature difference between the hot and cold sides. By setting $Q = 0$, the threshold voltage (V_Q) is obtained by

$$V_Q = [\frac{W(T_h - T_c)}{k_B T_h T_c} + 4\ln(\frac{T_h}{T_c}) + \ln(\frac{W + 2k_B T_h}{W + 2k_B T_c}) + \ln(\frac{W + E_F + k_B T_h}{W + E_F + k_B T_c})]\frac{k_B T_h}{q}. \tag{2.32}$$

The result shows that V_Q has a complicated dependence on T_h. Fig. 2.4 shows V_Q versus T_h at two different work functions. It is a surprising fact that V_Q has a linear dependence on T_h in the plotted range. When $T_h = 250$ K, i.e., no temperature difference between the hot and cold side, the value of V_Q is zero. The result agrees with the obvious law that there is no thermionic energy flow between two substance if there is no temperature difference and external voltage. According to the second law of thermodynamics, thermal energy would go from the hot material to the cold material. In order to stop this spontaneous movement, an external voltage is needed. As we can see, a bigger voltage is needed when the temperature difference is increased. Furthermore, V_Q also dependents on W. To be more specific, for a fixed temperature difference, V_Q increases with W. There is another threshold voltage V_I that separates the value of I from negative to positive. By setting $I = 0$, we obtain the threshold voltage as

$$V_I = \frac{1}{q}[k_B T_h \ln\frac{W + 2k_B T_c}{W + 2k_B T_h} + \frac{T_c - T_h}{T_c}W] \tag{2.33}$$

The value of V_I is less than the value of V_Q, shown in Fig. 2.4, since the energy carried by a hot side electron is greater than that of a cold side electron. Therefore, the energy flow comes from hot side to cold side when $I = 0$.

The efficiency (η) of the refrigerator is calculated by $\eta = -Q/(IV)$. In order to characterise the performance of the refrigerator, the relative ratio of η and Carnot efficiency $\eta_c = T_c(T_h - T_c)^{-1}$ is calculated

$$\frac{\eta}{\eta_c} = -\frac{1}{qV}(W + 4k_B T \times \frac{T_h - T_c I_{ch}}{1 - I_{ch}}). \tag{2.34}$$

where $I_{ch} = I_c/I_h$. The voltage and hot side temperature dependence of the efficiency η is investigated (shown in Fig. 2.5), where the value of the efficiency is given in color ranging from 0 to η_c. No cooling takes place when the voltage is too low or the hot side temperature is too high (the top left corner). As the voltage goes up, the efficiency firstly increases to a maximum value dramatically and then gradually decreases. As we discussed earlier, Q will be independent of voltage when the voltage is high enough.

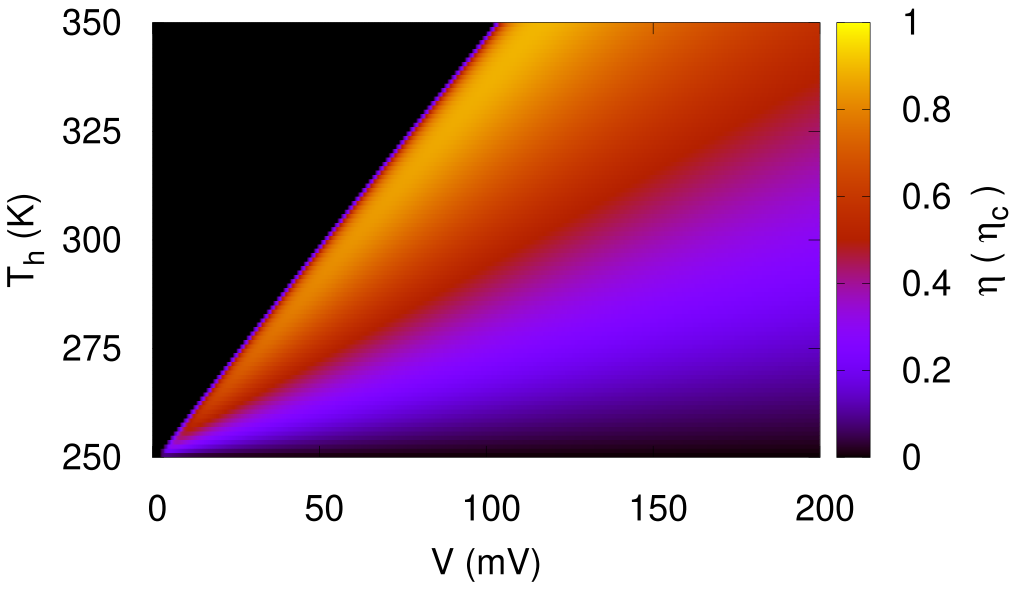

Figure 2.5: Voltage and hot side temperature dependence of efficiency (η) where E_F = 0.1 eV and W = 0.2 eV. The color indicates the value of η arrange from 0 to η_c.

The current (I) has the same trend as Q. Hence, the efficiency will gradually decrease with the voltage after the initial increment, which can also be seen from Eq. 2.34.

The performance of Dirac semimetals (labeled by subscript D) and conventional materials (labeled by subscript R) in thermionic refrigeration is compared in Fig. 2.6 and Fig. 2.7. Although the energy flow Q_R is larger than Q_D by about four times, the efficiency of Dirac semimetals is considerably higher than that of conventional materials. The main reason behind the higher efficiency of 3D Dirac semimetals is the energy-carrying capability of electrons in the different materials. As shown in Eq. 2.27, the energy carried by Dirac particles per degree of freedom is twice that of a particle with a parabolic energy dispersion. Carriers with a parabolic dispersion have the highest charge current, as shown in Fig. 2.2. However, the energy current in 3D materials is enhanced. As a result, 3D Dirac semimetals have the highest thermal efficiency, compared to both parabolic materials and graphene. Therefore, together with their low thermal conductivity and high electron mobility, it is somewhat reasonable to expect that 3D Dirac semimetals would make excellent candidates for thermionic devices. It should be pointed out that we only considered the ideal case of no heat backflow. In a

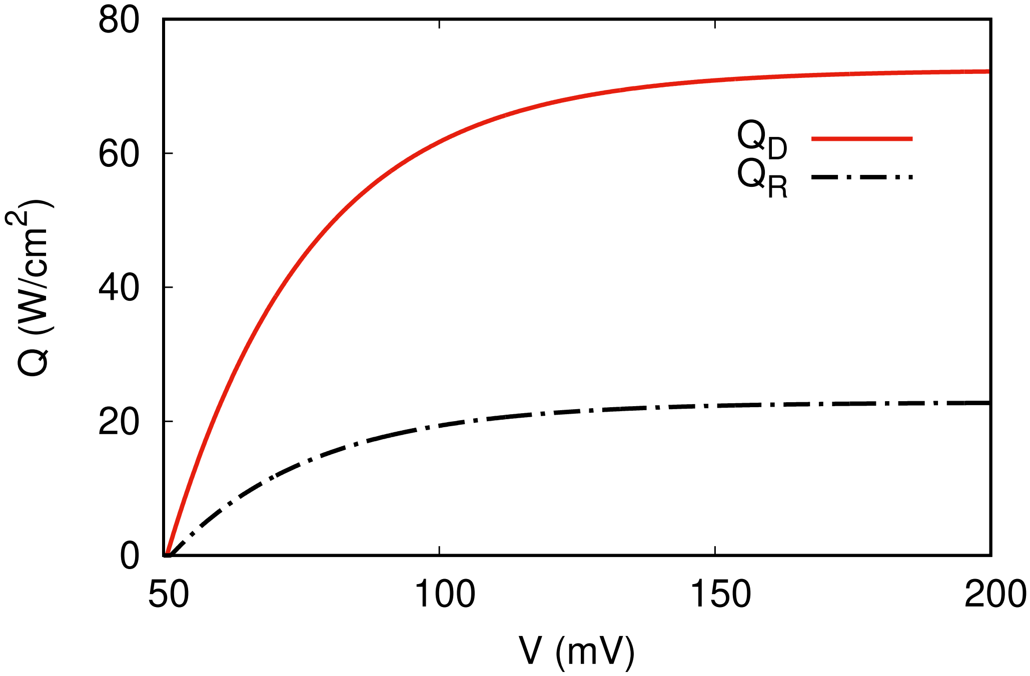

Figure 2.6: The voltage dependence of energy flow Q where the solid red line and the dashed black line are for Dirac materials and conventional materials. Here $T_c = 250$ K, $T_h = 300$ K, $E_F = 0.1$ eV and $W = 0.2$ eV.

practical device, there is a heat backflow due to phonon conduction $Q_p = (T_h - T_c)/R_{th}$ where R_{th} is the thermal resistance. The heat backflow will significantly reduce the thermal efficiency in all three systems discussed.

Now we study the dependence of energy flow and efficiency on external voltage. For both Dirac and conventional materials, the energy flow firstly increases with the external voltage and then reaches a maximum value. The reason is that the external voltage only suppresses the thermal energy of the hot side going to the cold side, which can be seen from Eq. 2.28 - Eq. 2.31. Hence further increasing the external voltage will make no changes to the entire energy flow if the external voltage is already large enough to completely suppress the energy of the hot side flowing into the cold side. Unlike the energy flow, the efficiency firstly increases rapidly with the increase of external voltage to a maximum value and then gradually decreases with the external voltage. The main reason is that the energy flow and total current would reach a constant value as the increase of external voltage while the total energy consumption per unit time $V \times I$

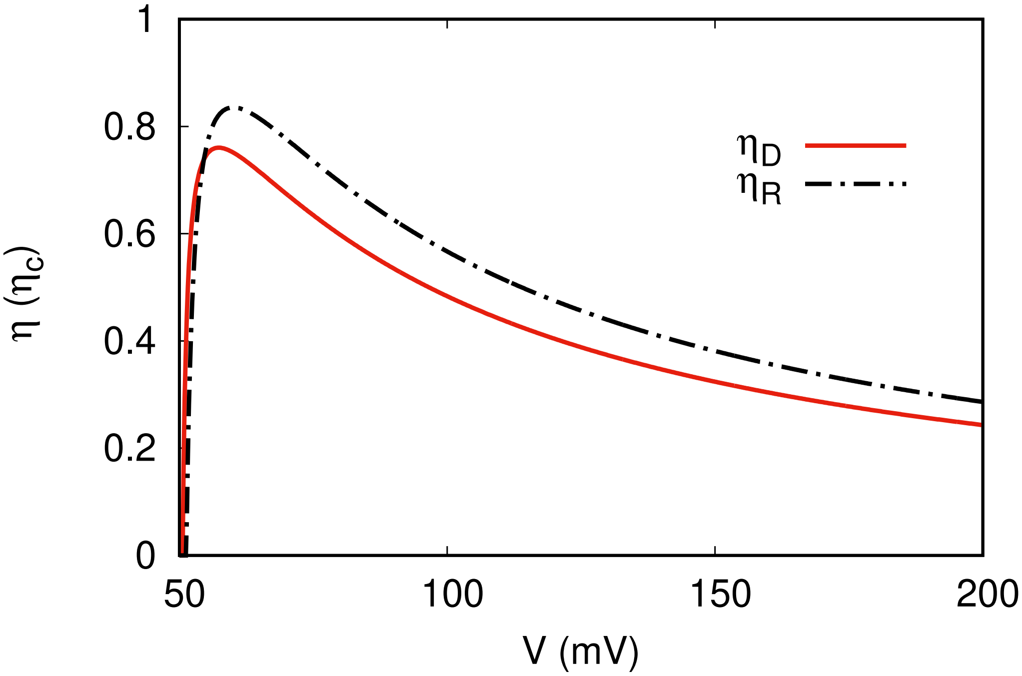

Figure 2.7: The voltage dependence of efficiency η where the solid red line and the dashed black line are for Dirac materials and conventional materials. Here $T_c = 250$ K, $T_h = 300$ K, $E_F = 0.1$ eV and $W = 0.2$ eV.

would continually increase with the external voltage V.

Refrigerators usually work at different temperatures. In different work temperatures, their performance would be different. In order to see the influence of temperature on their performance, external voltage V dependence of energy flow and efficiency η at two different hot side temperatures (T_h) are investigated (shown in Fig. 2.8), where solid line and dashed line are Q and η, respectively. Red line is for $T_h = 300$ K, and black line is for $T_h = 350$ K. In addition, $T_c = 250$ K, $E_F = 0.1$ eV and $W = 0.28$ eV are used for the calculations. The results show that the maximum efficiency and energy flow are nearly identical at the two work temperatures. However, the external voltage that is required to achieve maximum efficiency is considerably different for the two work temperatures. This means that in order to work efficiently, the external voltage should change with the working temperature. In practical applications, a low energy consumption device can be realized by applying a variable external voltage. The value of the external voltage is set according to the working temperature to realize the best

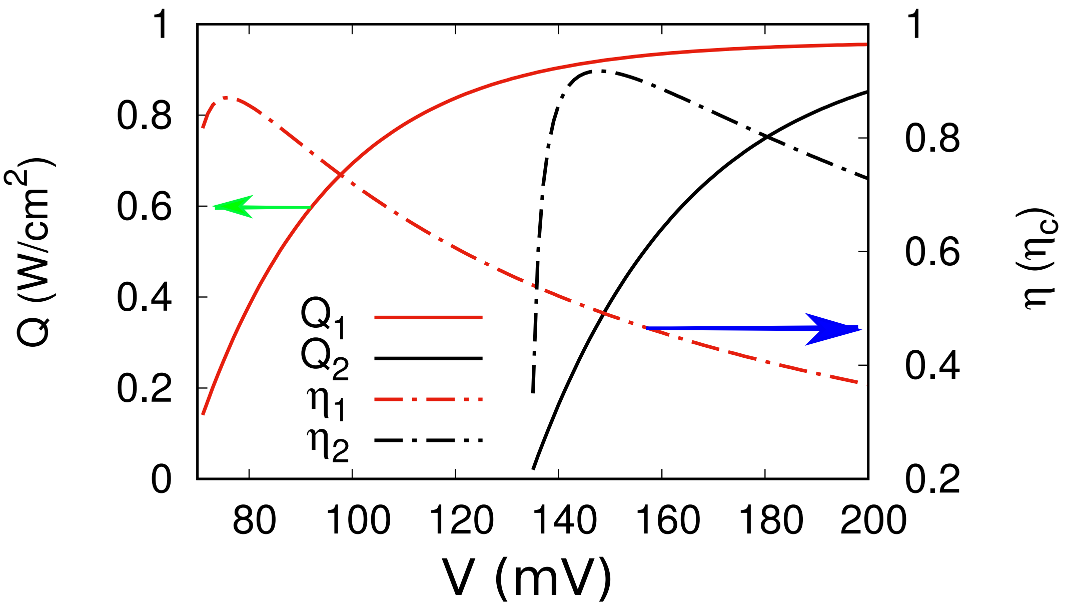

Figure 2.8: External voltage V dependence of energy flow (Q) and efficiency η at two different hot side temperatures (T_h), where the solid line and dashed line are Q and η, respectively. The red line is for T_h = 300 K, and black line is for T_h = 350 K. Here T_c = 250 K, E_F= 0.1 eV and W = 0.28 eV are used for the calculation.

work efficiency.

2.5 Outlook

The absolute value of the standard Richardsons coefficient is about 120A/cm^{2}K^2. The modificatory one for 3D Dirac semimetals would less than that by several times and the modificatory one for graphene even would less than that by two orders of magnitude. Therefore, one may think why not use the conventional materials as the cathode (cold side) of refrigerator devices and Dirac semimetals (graphene) as the anode (hot side), shown in Fig. 2.9.

It is reasonable to argue that such a device would have a better performance compared to its counterparts that are based on one kind of material. The argument is that the total net current may be enlarged in such a device. However, we would like to point out that the conventional method that is used to describe the performance of thermionic refrigerator or generator breaks down. The first reliable evidence is that it breaks the second law of thermodynamics. The law tells us that thermal energy always flows from

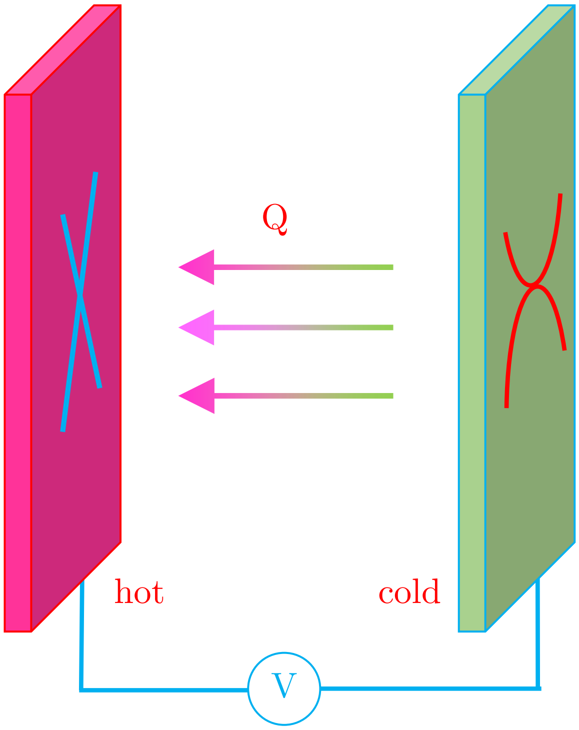

Figure 2.9: Schematic diagram of the refrigerator that is based on conventional and Dirac semimetals.

the hot side into the cold side. However, as we can see from Fig. 2.9, the thermal energy flows from the cold side into the hot side without an external voltage when the temperature difference is smaller than 50 K. The physical reason is that even though conventional materials can emit more electrons than 3D Dirac semimetals (graphene), many of the electrons would be reflected by 3D Dirac materials (graphene) and make no contribution to the thermionic current.

2.6 Conclusion

We have shown the TEC of 3D Dirac semimetals can be calculated by $J_D = A_D T^2 \mathrm{e}^{-W/k_BT}$ where $A_D = \frac{qk_B^2}{4\pi^2\hbar^3 v_F^2}(W + E_F + 2k_BT)$. As we expected, A_D is considerably larger than A_G. However, it is still smaller than A_{RD}. The underlying reason is that the density of states of 3D semimetals $g(\epsilon) = \frac{\epsilon^2}{\pi^2\hbar^3 v_F^2}$ is smaller than that of 3D conventional semiconductors $g(\epsilon) = \frac{(2m)^{3/2}}{2\pi^2\hbar^3}\sqrt{\epsilon}$. Although A_G and A_D are smaller than A_{RD}, the thermionic emission in Dirac systems has one fundamental advantage in that the average energy carried by per freedom of electrons in Dirac systems is twice that of conventional semiconductors. We have noted that the exponential term e$^{-W/k_BT}$ present in J_G, J_D and J_{RD} is due to the Maxwell-Boltzmann distribution function e$^{(E_F-\epsilon)/k_BT}$. Dirac semimetals exhibit excellent properties with respect to thermionic cooling. Due to an enhanced group velocity along the emission direction, the thermionic current is enhanced compared to graphene. Due to the higher energy carrying capability, the efficiency of thermionic cooling is higher than that in graphene and conventional materials.

Chapter 3

Thermionics in nodal-ring semimetals

In this chapter, we theoretically investigate the thermionic emission from nodal-ring semimetals. The thermionic emission is found to be anisotropic in the x and y directions. The anisotropic emission can be enhanced by increasing the radius of nodal-ring $\epsilon_0/(\hbar v_F)$. Nodal-ring not only results in an anisotropic thermionic emission current but also affects the value of thermionic emission current (TEC). The TEC of the lower branch of energy-momentum dispersion increases with ϵ_0, while the TEC of the upper branch decreases with ϵ_0. In the limit of $\epsilon_0 = 0$, a nodal-ring semimetal becomes to a Dirac semimetal resulting in a Dirac TEC. Unlike in conventional materials, the TEC in nodal-ring semimetals depends on the Fermi energy, similar to the situation in graphene and Dirac semimetals. The underlying reason is that graphene, Dirac semimetals and nodal-ring semimetals have a linear or linear-like energy-momentum dispersion while conventional materials have a parabolic energy-momentum dispersion. The TEC of nodal-ring semimetals slightly depends on ϵ_0 and E_F, while it heavily depends on the work function and temperature. By Increasing the value of ϵ_0, a positive effect on the performance of thermionic refrigerators is observed.

3.1 Introduction

Materials with a linear energy-momentum dispersion such as graphene [63–65], Dirac semimetals and Weyl semimetals [66, 67] have received much attention in recent years [68–73]. Dirac materials are a type of topological material, which are protected by time-reversal and spatial inversion symmetries [74]. If one of the above symmetries is broken, Dirac semimetals turn into Weyl semimetals [75]. Recently, a new type of 3D topological semimetal has been theoretically predicted [76, 77] and experimentally realized in ZrSiSe [78]. This new type of topological material is called nodal-line semimetals, which is also protected by the time-reversal and the inversion symmetries [79]. Additionally, it is protected by mirror reflection and nonsymmorphic symmetries [80, 81]. Its conduction and valence band cross each other at many points which form a continuous ring (shown in Fig. 3.1) instead of a single point in Dirac semimetals. The radius of the ring b is a key material parameter of nodal-ring semimetals. The value of b can be measured by angle-resolved photoemission spectroscopy [82]. However, direct physical property measurements associated with b are highly desired. Researchers have proposed a magneto-optical way to determine b accurately [83]. By applying a magnetic field along the ring axis, the axial magnet-optical response is found to have a giant peak at the position of $2b$, which is independent of the strength of the magnetic field and can be used to determine the value of b. In the limit $\epsilon_0 = 0$, nodal-ring semimetals turn to Dirac semimetals. In this sense, nodal-ring and Weyl semimetals are variations of Dirac semimetals.

Magnetic susceptibility [84], Landau quantization [85], Lifshitz transitions [86] and quantum anomalies [87] have been investigated in nodal-ring systems [88–90]. Thermionic emission in such systems is still not studied. In this chapter, we are going to investigate thermionic emission in such systems and explore their potential applications in thermionic devices. In the low-energy region, the density of states of nodal-ring semimetals is usually larger than that of Dirac semimetals. Additionally, the low energy-momentum dispersion in nodal-ring semimetals is anisotropic in the x- and y-directions. These features would make the thermionic emission different from its previous counterparts. We firstly develop the necessary formulas to describe the density of states

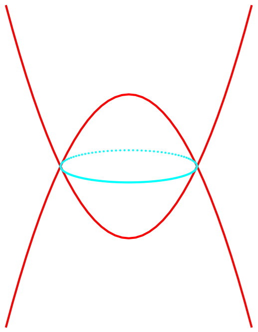

Figure 3.1: Schematic diagram of the energy-momentum dispersion of nodal-ring semimetals, where the green circle stands for the nodal ring.

and the TEC. Then thermionic emission is discussed in many situations. Finally, the performance of thermionic refrigerator made of nodal-ring semimetals is investigated.

3.2 Formalism

The energy-momentum dispersion of nodal-ring semimetals is given by [91]

$$\epsilon = s\hbar v_F \sqrt{k_x^2 + (\sqrt{k_y^2 + k_z^2} + s'b)^2}, \tag{3.1}$$

where $s = \pm$ and $s' = \pm$ are the band indexes. Using the equation, we plot the energy-momentum dispersion of nodal-ring semimetals in Fig. 3.2, where $k_x = 0$, $k_\perp = \sqrt{k_y^2 + k_z^2}$, $\epsilon_0 = \hbar v_F b$ and the dashed horizontal line is the Fermi level. We label the conduction bands as lower branch ϵ_1 $(s = +, s' = -)$ and upper branch ϵ_2 $(s = +, s' = +)$, and valance band as ϵ_3 $(s = -, s' = -)$ and ϵ_4 $(s = -, s' = +)$, respectively. The conduction band ϵ_1 touches the valence band ϵ_3 at points ($k_x = 0$, and $k_\perp = b$) forming a nodal-ring of radius b. The minimum value of ϵ_2 is ϵ_0, which means there is no density of states for ϵ_2 when $\epsilon_2 < \epsilon_0$. Here we only investigate the thermionic emission in conduction bands ϵ_1 and ϵ_2 since conduction bands make the main contribution to material properties. According to its definition, the density of states can be calculated by

$$g(\epsilon) = 2\frac{1}{(2\pi)^3} \int\int\int \delta(\epsilon - \epsilon(k_x, k_y, k_z)) \mathrm{d}k_x \mathrm{d}k_y \mathrm{d}k_z. \tag{3.2}$$

In the following discussion, we omit the indices in ϵ_1 and ϵ_2 for simplicity. For example, we write the density of states of ϵ_1 as $g_1(\epsilon)$ instead of $g_1(\epsilon_1)$. After some algebra, the density of states for ϵ_1 and ϵ_2 (Calculation details can be found in Appendix A.2) are obtained by

$$g_1(\epsilon) = \begin{cases} \frac{b\epsilon}{\pi\hbar^2 v_F^2} & \epsilon < \epsilon_0, \\ \frac{b\epsilon}{\pi^2\hbar^2 v_F^2}\arcsin(\frac{\epsilon_0}{\epsilon}) + \frac{\epsilon}{\pi^2\hbar^3 v_F^3}\sqrt{\epsilon^2 - \epsilon_0^2} + \frac{b\epsilon}{2\pi\hbar^2 v_F^2} & \epsilon \geq \epsilon_0, \end{cases} \tag{3.3}$$

$$g_2(\epsilon) = \frac{b\epsilon}{\pi^2\hbar^2 v_F^2}\arcsin(\frac{\epsilon_0}{\epsilon}) + \frac{\epsilon}{\pi^2\hbar^3 v_F^3}\sqrt{\epsilon^2 - \epsilon_0^2} - \frac{b\epsilon}{2\pi\hbar^2 v_F^2}. \tag{3.4}$$

When $\epsilon = \epsilon_0$, $g_1(\epsilon) = \frac{b\epsilon}{\pi^2\hbar^2 v_F^2} \times \frac{\pi}{2} + \frac{b\epsilon}{2\pi\hbar^2 v_F^2} = \frac{b\epsilon}{\pi\hbar^2 v_F^2}$ indicates that the density of states is continuous. In the limit $\epsilon_0 = 0$, $g_1(\epsilon) = \frac{\epsilon^2}{\pi^2\hbar^3 v_F^3}$ agrees well with the density of states of 3D Dirac materials.

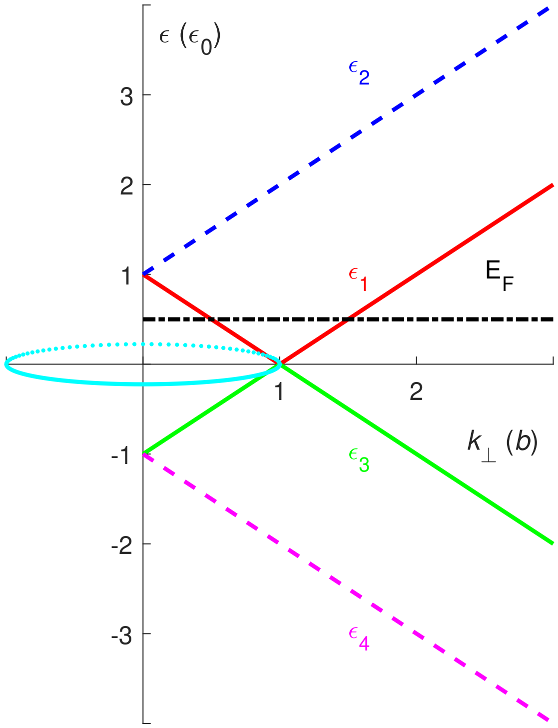

Figure 3.2: Schematic diagram of the energy-momentum dispersion of nodal-ring semimetals plotted by using Eq. 3.1, where $k_x = 0$, $k_\perp = \sqrt{k_y^2 + k_z^2}$ and $\epsilon_0 = \hbar v_F b$.

The energy-momentum dispersion is isotropic in the k_y and k_z directions, which results in the same TEC and the same form of component energy in the y- and z-directions. Therefore, only the TEC in the x- and y-directions needs to be calculated. The TEC in the m direction ($m = x$ or y) and n band ($n = 1$ or 2) is calculated by

$$J_{m,n} = \int q v_{m,n}(\epsilon) f(\epsilon_{k_x,k_y,k_z} - E_F) \mathrm{d}k_x \mathrm{d}k_y \mathrm{d}k_z, \tag{3.5}$$

where $f(\epsilon - E_F) = \frac{1}{1+\mathrm{e}^{\frac{\epsilon - E_F}{k_B T}}}$ is the Fermi-Dirac distribution function, q is the charge of one electron, and $v_{m,n}$ is the velocity component in the m dirction for n band, which is calculated by

$$v_{m,n} = \frac{1}{\hbar}\frac{\partial \epsilon_n}{\partial k_m}. \tag{3.6}$$

The velocity v_{x1} and v_{x2} are calculated by

$$v_{x1} = \frac{\hbar v_F}{\hbar}\frac{2k_x}{2\sqrt{k_x^2 + (\sqrt{k_y^2 + k_z^2} - b)^2}} = \frac{\hbar v_F^2 k_x}{\epsilon}, \tag{3.7}$$

$$v_{y1} = \frac{\hbar v_F^2 k_y}{\epsilon}(1 - \frac{b}{\sqrt{k_y^2 + k_z^2}}). \tag{3.8}$$

In the integral, the k_x, k_y and k_z should make $\epsilon_{m,n} > W + E_F$, which guarantees that we only count the electrons that have enough energy to cross the surface barrier in the m direction. Here, $\epsilon_{x,n}$ and $\epsilon_{y,n}$ are given by

$$\epsilon_{x,n} = \hbar k_x v_{x,n}, \tag{3.9}$$

$$\epsilon_{y,n} \quad = \hbar(k_y + (-)^n \tfrac{b}{2k_y}\sqrt{k_y^2 + k_z^2}) v_{y,n}. \tag{3.10}$$

For band ϵ_1, the energy components are given as

$$\epsilon_{x1} = \frac{\hbar^2 k_x^2 v_F^2}{\epsilon_1}, \tag{3.11}$$

$$\epsilon_{y1} \quad = \hbar(k_y - \tfrac{b}{2k_y}\sqrt{k_y^2 + k_z^2}) v_y. \tag{3.12}$$

The sum of the component energy in the x-, y- and z-directions is the total energy i.e., $\epsilon_n = \epsilon_{x,n} + \epsilon_{y,n} + \epsilon_{z,n}$. In our calculations, the Fermi velocity v_F is set to 10^6 m/s. For E_F, ϵ_0 and W, their default value is set to 0, 30 meV and 300 meV, respectively.

3.3 Thermionic emission

In the limit $\epsilon_0 = 0$, nodal-ring semimetals go to Dirac semimetals. By replacing the Fermi-Dirac distribution function with the Maxwell-Boltzmann distribution function that is rather reasonable for $\epsilon - E_F > 3k_BT$, the thermionic emission current can be analytically obtained by

$$J^0_{x1} = \frac{qk_B^2}{4\pi^2\hbar^3 v_F^2}(W + E_F + 2k_BT)T^2 \mathrm{e}^{-W/(k_BT)}. \tag{3.13}$$

The analytical and numerical results are shown by the black dashed line and solid circles in Fig. 3.3(a), respectively, which agree well with each other. When $\epsilon_0 \neq 0$, the TEC is numerically calculated. The results at three values of $\epsilon_0 = 30$ meV, 60 meV and 90 meV are shown in Fig. 3.3(a), which indicates the TEC increases with ϵ_0. A large ϵ_0 means a large nodal-ring, which results in a large density of states (shown in Fig. 3.3(d)). This is the underlying reason for the increase of the TEC.

As can be seen from Eq. 3.13, the TEC depends on the Fermi energy (E_F). The TEC dependence of E_F only comes from the density of states since the velocity (shown in Eq. 3.8) does not depend on E_F. The majority of electronic properties of a material are determined by the electrons near the Fermi level since they are more active and energetic. This is also true for the TEC. The electrons near the Fermi level have a higher average energy, which results in a larger chance to escape from the material. When E_F is increased by doping or an external voltage, there are more electrons near the Fermi level because the density of states increases with energy (shown in Fig. 3.3(d)). The temperature dependence of the TEC at three values of E_F is shown in Fig. 3.3(b). At a fixed temperature, the TEC increases with E_F.

In a thermionic process, electrons are driven by thermal energy to overcome the surface barrier. In this sense, the TEC would be heavily affected by the height of the surface barrier, i.e. work function W. As can be seen from Eq. 3.13, J^0_{x1} is proportional to $(E_F + W + 2k_BT)\mathrm{e}^{-W/(k_BT)}$, which indicates J^0_{x1} would decrease significantly with W. For $\epsilon_0 \neq 0$, the decrease still exists, shown in Fig. 3.3(c). At $T = 250$ K, J^0_{x1} drops almost five orders when W changes from 300 meV to 400 meV. When the temperature is increased from 250 K to 350 K, the dropping tendency slows down slightly. Increasing temperature means more electrons have sufficient energy to overcome the surface

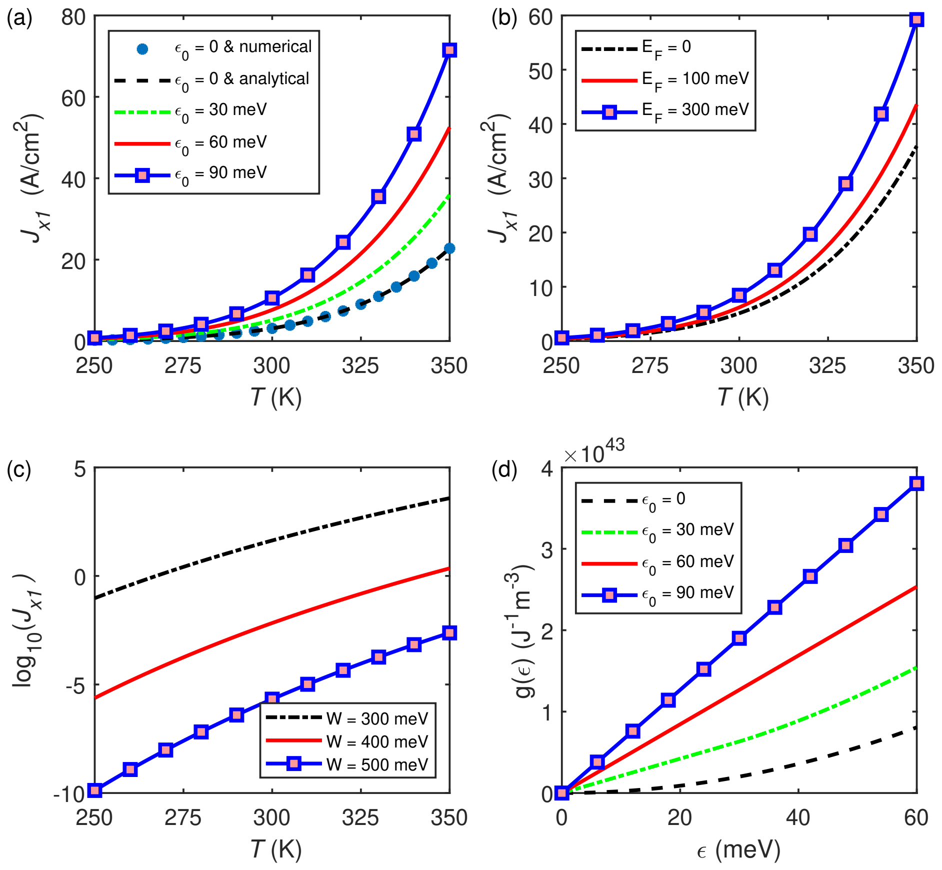

Figure 3.3: Thermionic emission of the lower branch. (a) Temperature dependence of J_{x1} at four values of ϵ_0 from 0 to 90 meV. For the limit ϵ_0 =0, J_{x1} is obtained both analytically and numerically, and the results agree with each other perfectly. (b) Temperature dependence of J_{x1} at three values of E_F from 0 to 300 meV. (c) $\log_{10}(J_{x1})$ as a function of T at three values of W. (d) Density of states against ϵ at four values of ϵ_0.

barrier. For conventional materials with a parabolic energy dispersion, the TEC has $T^2 \mathrm{e}^{-W/(k_BT)}$ dependence [22]. For single layer graphene with a parabolic energy dispersion perpendicular to the graphene layer and a linear energy dispersion in the layer, the TEC has $T^3 \mathrm{e}^{-W/(k_BT)}$ dependence [34]. For Dirac semimetals with a linear energy dispersion, the TEC has a $(E_F + W + 2k_BT)\mathrm{e}^{-W/(k_BT)}$ dependence. For nodal-ring semimetals, the TEC is supposed to show a similar temperature dependence with Dirac semimetals. The TEC in the above systems increases rapidly with temperature since T emerges in the exponent part (e^{-W/k_BT}). To see this clearly, $\log_{10}(J_{x1})$ against $\log_{10}(T)$

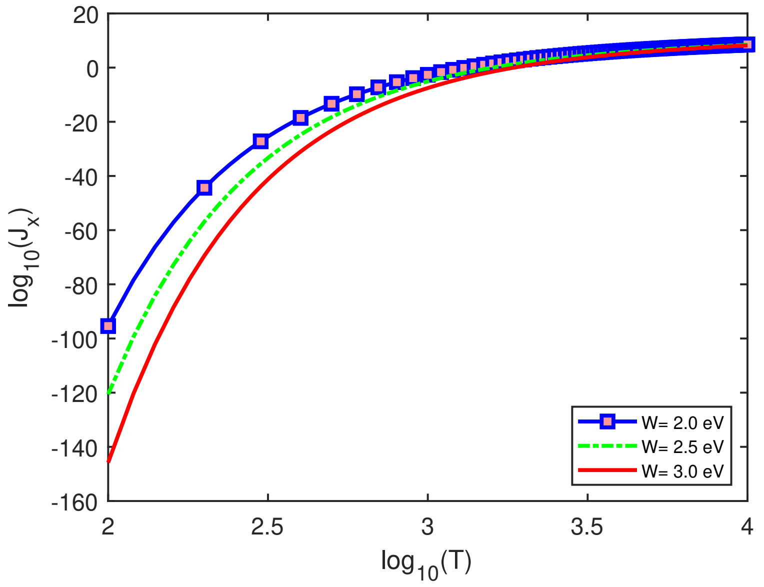

Figure 3.4: $\log_{10}(J_{x1})$ as a function of $\log_{10}(T)$ at three values of W from 2.0 eV to 3.0 eV.

is plotted in Fig. 3.4 at three values of W from 2.0 eV to 3.0 eV. When T increases from 100 K to 10,000 K, the TEC is increased by almost 100 orders.

Above all, the TEC slightly increases with E_F and ϵ_0. In our work, the increment is less than five times. However, the TEC decreases and increases dramatically with W and T, respectively. The decrement and increment can be as high as 100 orders. In a practical application, a minimum TEC, usually in the order of A/cm^2, is required and the working temperature is fixed in some range. For example, the working temperature is around 250 K ∼ 350 K when the thermionic effect is employed to make air-conditions and refrigerators—this is why our discussion is mainly focussed on 250 K ∼ 350 K. The temperature is around 500 K∼ 1000 K when the thermionic effect is employed to harvest thermal heat. In this sense, a proper work function should be chosen according to the working temperature and the minimum TEC. In a thermionic refrigerator, the work function usually needs to be less than 300 meV. This is the main barrier that hinders the practical applications of thermionic devices.

The energy-momentum dispersion of nodal-ring systems is anisotropic in the x- and y-directions and isotropic in the y- and z-directions, shown in Eq. 3.1. This results in that the thermionic emission is different in the x and y directions and is the same in the

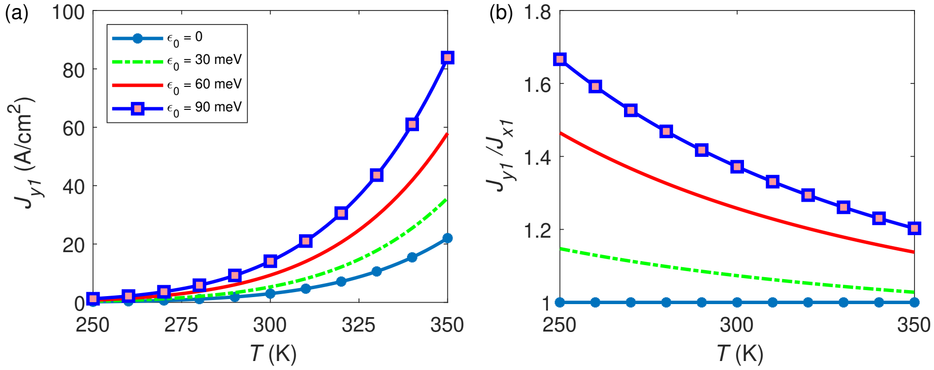

Figure 3.5: J_{y1}/J_{x1} as a function of T at four values of ϵ_0 from 0 to 90 meV.

y- and z-directions. To see the anisotropic thermionic emission, J_{y1}/J_{x1} as a function of T is calculated and shown in Fig. 3.5. In the limit $\epsilon_0 = 0$, the value of J_{y1}/J_{x1} is equal to one over the entire temperature range. Indeed, this is expected since the thermionic emission is isotropic in Dirac systems ($\epsilon_0 = 0$). For $T = 250$ K, J_{y1}/J_{x1} increases with ϵ_0, and the maximum value reaches 1.68, indicating anisotropic thermionic emission. The value of J_{y1}/J_{x1} decreases with T, which indicates J_y and J_x having different temperature dependence. Above all, thermionic emission in nodal-ring systems displays a temperature dependent anisotropic response in the x- and y-directions.

Now we move to the thermionic emission of the upper branch ϵ_2. The thermionic emission current J_{x2} as a function of T at four values of ϵ_0 is plotted in Fig. 3.6(a). The results are fundamentally different from the results of the lower branch. J_{x2} decreases with ϵ_0, while J_{x1} increases with ϵ_0. This dependence can also be understood by the decrease of the density of states. For the upper branch, the density of states is zero when $\epsilon < \epsilon_0$. In this sense, the density of states near the Fermi surface ($E_F = 0$) decreases with ϵ_0, which leads to the number of thermal driven electrons decreasing with ϵ_0. For $T = 350$ K, J_{x2} drops by more than eight times when ϵ_0 changes from 0 to 90 meV. Besides, the zero density of states results in a smaller J_{x2} compared with J_{x1}. To visualise this, J_{x1} and J_{x2} together with $J_{xT} = J_{x1} + J_{x2}$ as a function of T are plotted in Fig. 3.6(d). The results show J_{x1} is considerably larger than J_{x2}, which indicates that the total TEC is mainly contributed by the lower branch of energy-momentum dispersion. For example, J_{x1} contributes about 75% to J_{xT} when $T = 350$ K.

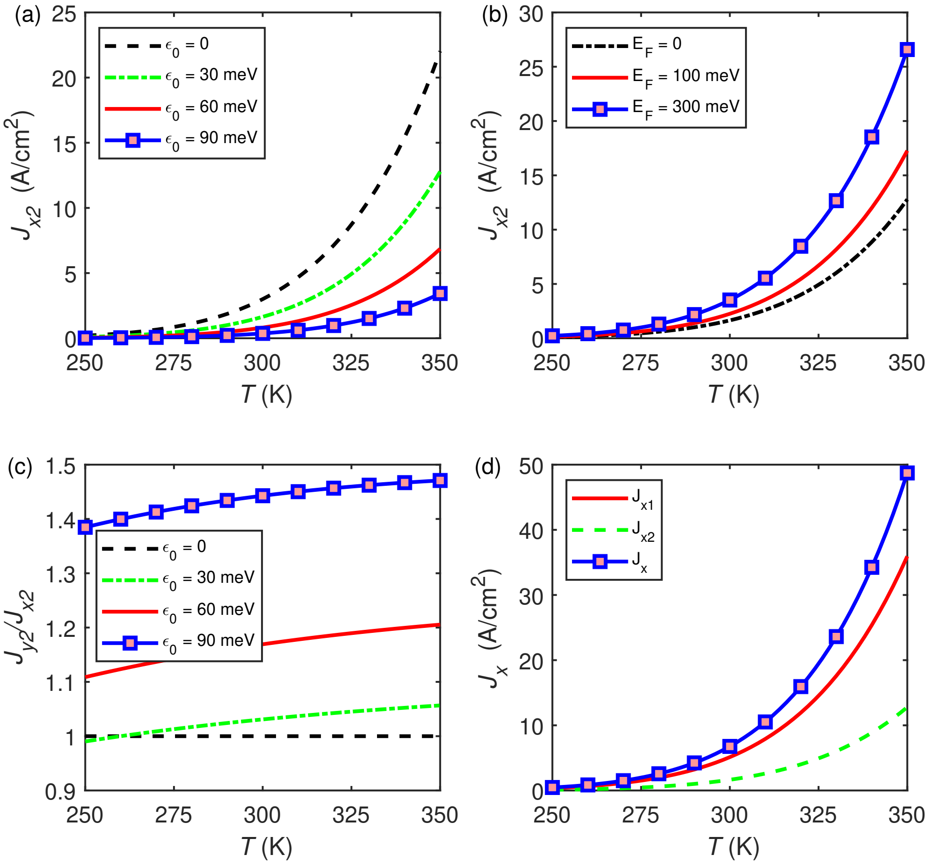

Figure 3.6: Thermionic emission of the upper branch. (a) Temperature dependence of J_{x2} at four values of ϵ_0 from 0 to 90 meV. (b) Temperature dependence of J_{x2} at three values of E_F. (c) J_{x2}/J_{y2} against T at three values of ϵ_0. (d) J_{x1}, J_{x2} and J_{xT} as a function of T.

The Fermi energy dependence of J_{x2} is also investigated and shown in Fig. 3.6(b). The results are similar to that of the lower branch, i.e., J_{x2} increases with E_F. When E_F is increased, the density of states near the Fermi surface is increased. This would increase J_{x2}. For the upper branch, the anisotropic thermionic emission is still expected due to the anisotropy of the energy-momentum dispersion. The temperature dependence of J_{y2}/J_{x2} at four values of ϵ_0 is plotted in Fig. 3.6(c). In the limit of $\epsilon_0 = 0$, J_{y2}/J_{x1} is equal to one which is rather reasonable since thermionic emission in Dirac systems is isotropic. When ϵ_0 is increased, J_{y2}/J_{x2} is larger than one showing an anisotropic thermionic emission in the x- and y-directions. Additionally, the anisotropic emission increases with ϵ_0. Unlike in the lower branch, the anisotropy shows little temperature dependence in the temperature range 250 K ∼ 350 K.

3.4 Thermionic devices

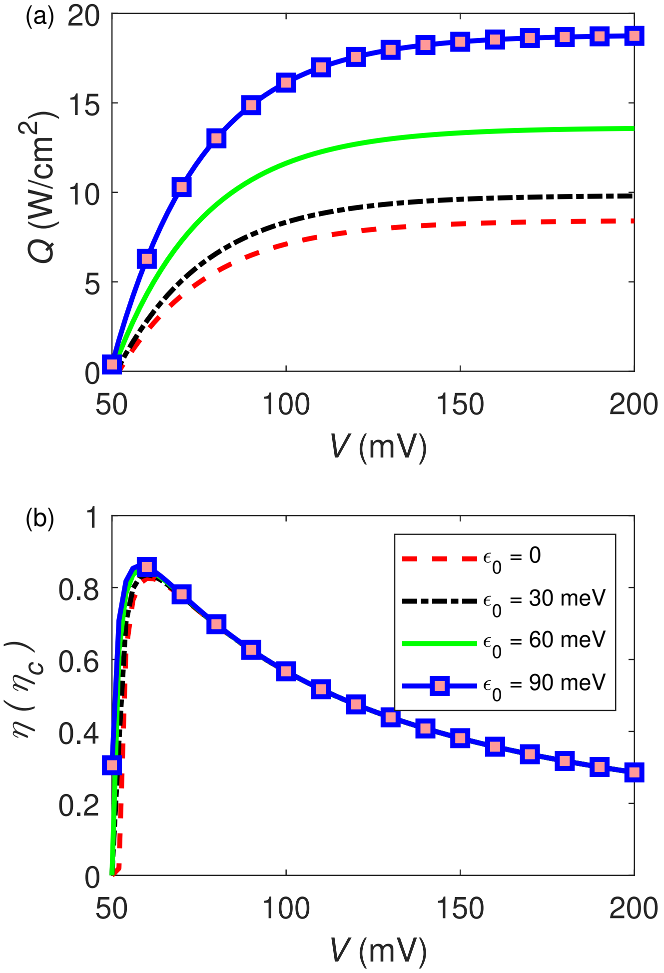

Figure 3.7: Impact of ϵ_0 on the performance of the thermionic refrigerator. (a) energy flow Q and (b) efficiency η as a function of external voltage at four values of ϵ_0 from 0 to 90 meV, where $E_F = 0$ and $W = 200$ meV.

In this section, we investigate the effect of ϵ_0 on the net energy flow Q and the ideal efficiency η of a thermionic refrigerator, which is made of nodal-ring semimetals. In the calculation, other energy losses such as radiation and heat conduction are ignored, and the space charge effect is not taken into consideration. Based on the above assumptions, the net energy flow and the ideal efficiency can be calculated by [92]

$$Q = [(W + 4k_BT_c)I_c - (W + 4k_BT_h)I_h]/q, \tag{3.14}$$

$$\frac{\eta}{\eta_c} = -\frac{Q}{P} \times \frac{T_h - T_c}{T_c}, \tag{3.15}$$

where $I_c = J_{xT}(T_c)$, $I_h = J_{xT}(T_h)\mathrm{e}^{qV/k_BT_h}$, V is the external voltage, T_c and T_h are the temperatures of cold side and hot side respectively. $\eta_c = \frac{T_c}{T_h - T_c}$ is the Carnot efficiency, and $P = IV = (I_c - I_h)V$ is the external power.

Energy flow and efficiency as a function of external voltage at four values of ϵ_0 from 0 to 90 meV are plotted in Fig. 3.7(a) and Fig. 3.7(b), respectively. Here the work function is chosen to be 200 meV in order to produce enough large net energy flow in the order of W/cm^2. The Fermi energy is set to 0 to keep the thermionic emission near the nodal-ring. The cold side and hot side temperatures are 250 K and 300 K, respectively, which is the work temperature range of the most refrigerators. The results show that nodal-ring size ϵ_0 can significantly affect the net energy flow. At $V = 200$ mV, the value of Q is tripled when ϵ_0 changes from 0 to 90 meV. Although ϵ_0 only has a limited effect on the ideal efficiency, a small enhancement of η is observed when ϵ_0 is increased.

3.5 Conclusion

We have investigated the thermionic emission in nodal-ring systems and its potential applications in thermionic refrigerators. The thermionic emission shows anisotropy in the x- and y-directions in both the lower and upper branches of the energy-momentum dispersion. The anisotropic emission can be enhanced by increasing ϵ_0. TEC increases with ϵ_0 in the lower branches, while it decreases with ϵ_0 in the upper branch. However, TEC increases with E_F for both of the situations. Although the value of TEC can be tuned by E_F and ϵ_0, the change is limited, usually less than one order of magnitude. T and W can significantly change the value of TEC, which can be as high as 100 orders of magnitude. If material parameters such as W, E_F and v_F have the same values, TEC of nodal-ring systems is larger than that in Dirac systems due to the larger density of states. In thermionic refrigerators made of nodal-ring semimetals, increasing the value of ϵ_0 has a positive effect on both Q and η. Our results are helpful to understand the thermionic emission in nodal-ring systems.

Chapter 4

Thermionical enhacned heat transfer in Dirac semimetal based devices

* We calculate the heat transfer from electronic devices without and with thermionic cooling. Without thermionic cooling, the internal temperature of the devices is at best equal to and usually higher than the temperature of the surrounding environment. However, when thermionic cooling is employed to transport heat, the internal temperature can be considerably lower than the environmental temperature. Below a critical environmental temperature (T_{c1}), the internal heat can be well transferred to the surrounding environment by thermal radiation and thermal conductivity alone; *i.e.* the device can operate well without thermionic cooling. When the environmental temperature is higher than T_{c1}, thermionic cooling can be used to accelerate the heat transfer processes to keep low internal temperature. When the environmental temperature is higher than a second critical environmental temperature, T_{c2}, the device cannot operate well even with thermionic cooling. T_{c1} increases with the thermal resistance K, while T_{c2} decreases with K. In the proposed thermionic cooling process, the energy efficiency can be as high as 75% of the Carnot efficiency.

---

* This chapter is based on S Huang, R Lewis and C Zhang., Thermionic enhanced heat transfer in electronic devices based on 3D Dirac materials., Journal of Applied Physics, 126(2019) 165105.

4.1 Introduction

The heat power density of electronic devices increases rapidly with their miniaturization and integration, which are the main developments of future devices. The high density of heat power demands more powerful methods to transport heat. Otherwise, a high internal temperature will result. For electronic devices, a high internal temperature reduces not only their efficiency but also their lifetime [93]. There are several cooling schemes to overcome these problems, such as high-flux heat pipes, air-cooled heat sinks, direct liquid immersion and thermionic cooling [94, 95]. Thermionic cooling is based on thermionic emission that was discovered by Richardson in 1901. Thermionic emission refers to the process where electrons are driven by thermal energy across a surface barrier, which is a hot research topic [96–100]. For conventional materials with a parabolic energy-momentum dispersion, the thermionic emission density is described by the Richardson-Dushman (RD) law:

$$J_R(T) = \frac{qmk_{\mathrm{B}}^2}{2\pi^2\hbar^3}T^2\mathrm{e}^{-q\phi\beta}, \tag{4.1}$$

where q is the electron charge, m is the electron mass, k_{B} is the Boltzmann constant, $\hbar$ is the reduced Plank's constant, ϕ is the surface potential and $\beta = 1/(k_{\mathrm{B}}T)$, where T is the thermodynamic temperature. Graphene, a single layer 2D material, has been reported to have many remarkable properties, such as ultra-high mobility, excellent conductivity and a linear energy-momentum dispersion [11, 18, 101]. Its thermionic emission cannot be described by the RD law, due to the linear energy-momentum dispersion. A modified law has been developed to describe thermionic emission in graphene by assuming that it has a linear energy-momentum dispersion within the plane and a parabolic dispersion perpendicular to the plane. In this case [29, 34, 38],

$$J_G(T) = \frac{qk_{\mathrm{B}}^3T}{2\pi^2\hbar^3v_{\mathrm{F}}^2}T^2\mathrm{e}^{-q\phi\beta}, \tag{4.2}$$

where v_{F} is the Fermi velocity. The thermionic emission current density is lower than in its counterpart in 3D conventional materials since the density of states is lower than that of 3D materials. The low thermionic emission current of graphene can be increased in 3D Dirac materials. As in graphene, the low-energy fermionic excitations in Dirac materials behave as massless Dirac particles [20]. Additionally, their low energy-momentum is linear along all three momentum directions. A 3D Dirac semimetal phase has been experimentally observed in Cd_3As_2 by means of angle-resolved photoemission spectroscopy [102]. The material has attracted considerable attention [68, 103–105] and has been found to have many astounding properties such as the extraordinarily high mobility of electrons (10,000 $\mathrm{cm}^2/\mathrm{V\ s}$ at room temperature) [106], tunable mid-infrared optical switching [69], low thermal conductivity [42] and high efficiency and non-Richardson thermionics [92]. Therefore, it is regarded as a building block of future devices. Starting with the 3D linear energy-momentum dispersion, the thermionic emission of 3D Dirac materials is determined to be [92]

$$J(T) = \frac{q k_{\mathrm{B}}^2}{4\pi^2 \hbar^3 v_{\mathrm{F}}^2} (q\phi + E_{\mathrm{F}} + 2k_{\mathrm{B}}T) T^2 \mathrm{e}^{-q\phi\beta}, \tag{4.3}$$

where E_{F} is the Fermi energy.

Based on thermionic emission processes, two kinds of devices, namely thermionic generators and thermionic coolers, have been proposed [31, 95, 107]. Thermionic generators show promising applications in harvesting thermal energy [33, 108]. Besides, they have been used to convert solar energy to electricity [109]. The investigation of thermionic cooling can be dated back to 1994 when G. D. Mahan described thermionic refrigeration [25]. The thermionic cooler is made of two parallel planes and a thermal barrier. Theoretically, the cooler can work as a room temperature refrigerator if the work function of its anode is about 0.3 eV. A few years later, Mahan extended the work to multilayer thermionic refrigeration [22]. Since then, thermionic cooling has attracted a great deal of attention and has been studied extensively [23, 24, 110]. Recently, much experimental work has been carried out [27, 111, 112], and a large thermionic cooling has been observed. This work paves the way for practical applications of thermionic refrigeration.

In this chapter, we demonstrate that thermionic emission in 3D Dirac materials can be used to cool electronic devices effectively. Additionally, the energy (power) consumed by the process is low, and the cooling efficiency is high.

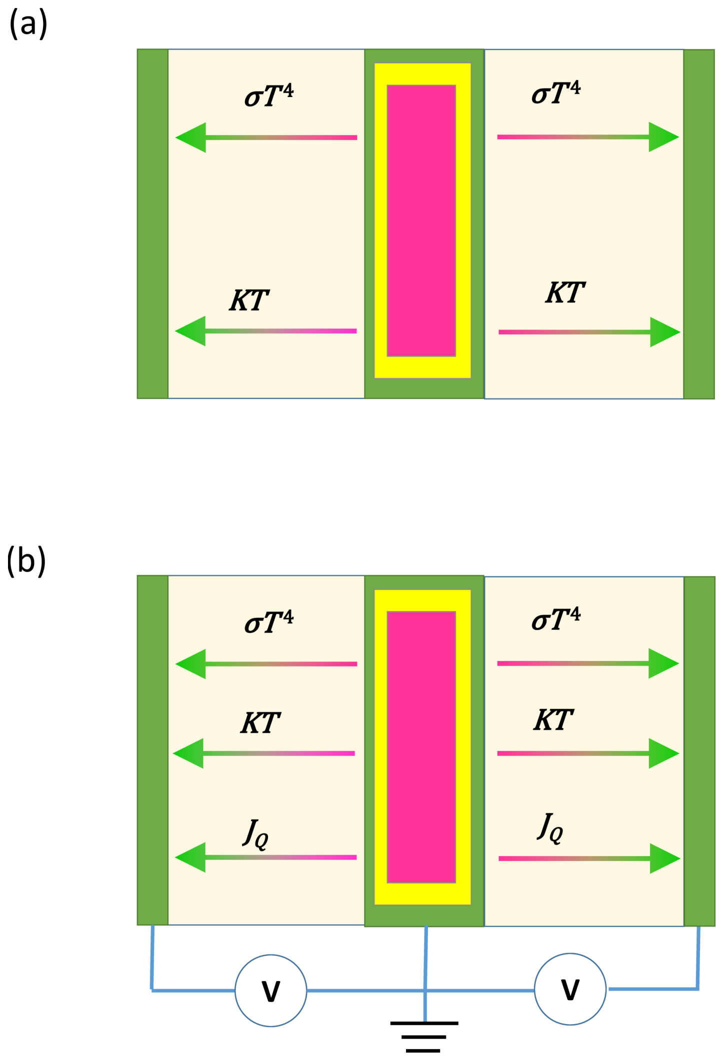

Figure 4.1: A schematic diagram of the electric devices (a) without thermionic cooling (b) with thermionic cooling. The red part of the center plane is the heart of the device, which is coated by a layer of insular materials indicated by yellow. The green outer layer of the center plane is the cathode giving out thermionic emission, and its temperature (T) is the internal temperature. The left and right green planes are the boundaries of the device, which have constant temperature T_E, named as environmental temperature. The green part of the planes is made of Dirac semimetal. The center green plane is grounded, and the green boundary planes are positively biased. (a) and (b) have the same structure except for the external voltage.

4.2 Model

A schematic diagram of electric devices without and with thermionic cooling is shown in Fig. 4.1(a) and (b), respectively. The red part of the center plane is the heart of the electronic device that realizes all electronic functions, which is coated by a layer of insular materials indicated by yellow. The green outer layer of the center plane is the cathode giving out thermionic emission, and its temperature is the internal temperature. The left and right green planes are the boundaries of the device and provide mechanical protection. Between the center plane and the boundary planes, there is a thermal barrier. This can be a vacuum gap or a barrier material. The center plane will produce heat at a constant power Pin while the device runs. For devices without thermionic cooling, the heat is transferred to the boundary planes by thermal radiation and thermal conduction. For devices with thermionic cooling, the heat is also transferred to the boundary planes by thermionic cooling. In our model, the temperature of the center plane (the internal temperature, T) is assumed to be uniform, and the temperature of boundary planes (the environmental temperature, T_E) is assumed to be both uniform and constant. According to the Stefan-Boltzmann law, the thermal radiation heat is approximately given by $2A\epsilon\sigma(T^4 - T_{\mathrm{E}}^4)$, where $\sigma = 5.67 \times 10^{-8}$ Js^{-1}m^{-2}K^{-4} is the Stefan-Boltzmann constant, ϵ is the emissivity and $2A$ (here 2 for the left and right sides) is the surface area of the centre plane. The thermal conduction heat is given by $2AK(T - T_{\mathrm{E}})$, where K is the thermal coefficient. The thermionic cooling is realized by carefully choosing materials and applying an external voltage (V) between the centre plane and the boundary planes. We assume both centre and boundary planes are made up of the 3D Dirac material $\mathrm{Cd_3As_2}$. In our devices, the thermionic cooling can be turned on and off by controlling the external voltage, while the thermal radiation and thermal conduction will always be present. In our calculations, the following parameters are used, $K_0 = 2 \times 10^3$ W/cm^{2}K, $V = 55$ mV and $q\phi = 250$ meV.

4.3 Results and discussion

At the outset, we discuss the heat transfer in devices without thermionic cooling. The heat is transferred by two kinds of mechanism, i.e. thermal radiation and thermal conduction. The entire heat transfer processes can be described by the following equation

$$\Delta Q = mC_v\Delta T = AP_{\mathrm{in}}\mathrm{d}t - 2A\epsilon\sigma(T^4 - T_{\mathrm{E}}^4)\mathrm{d}t - 2AK(T - T_{\mathrm{E}})\mathrm{d}t, \tag{4.4}$$

where ΔQ is the heat change of the centre plane in a small period of time dt, $m = \rho A d$ is the mass of the centre plane, $\rho = 3.03 \times 10^3$ kg/cm^3 is the volumetric mass density of Cd$_3$As$_2$, $d = 1$ mm is the thickness of the centre plane, ΔT is the change of the internal temperature, K is the thermal resistance and C_v is the specific heat capacity of Cd$_3$As$_2$. Since this value is not available, we assume it can be approximately calculated by

$$C_v = \frac{3m_{Cd}C_v^{Cd} + 2m_{As}C_v^{As}}{3m_{Cd} + 2m_{As}}, \tag{4.5}$$

where $C_v^{Cd} = 230$ J/kg K and $C_v^{As} = 330$ J/kg K are the specific heat capacity at room temperature of cadmium (Cd) and arsenic (As), respectively, and m_{Cd} and m_{As} are the standard atomic weights of Cd and As. The calculated C_v is 260 J/kg K and we assume it is constant in our calculation. After some algebra, Eq. 4.4 can be rewritten as

$$\Delta T = \frac{2}{\rho d C_v}[\frac{P_{\mathrm{in}}}{2} - \epsilon\sigma(T^4 - T_{\mathrm{E}}^4) - K(T - T_{\mathrm{E}})]\mathrm{d}t, \tag{4.6}$$

where $P_{in} = 1$ W/cm^2 and $\epsilon = 0.5$. There are only two unknown parameters i.e. ΔT and dt. In this sense, the time dependence of the internal temperature can be calculated.

Time dependence of the internal temperature at three different values of K are shown in Fig. 4.2(a) and (b) for $T_E = 25\,°$C and $60\,°$C, respectively. In the present work, $40\,°$C is assumed to be the highest internal running temperature of the devices. For $K = 0.2K_0$ and $T_E = 25\,°$C, the device cannot operate at all since the internal temperature will reach $40\,°$C in just one second and then reach a maximum temperature of $50\,°$C. When $T_E = 25\,°$C, the maximum internal temperatures for $K = K_0$ and $K = 5K_0$ are about $30\,°$C and $26\,°$C, respectively, which indicates the devices run well at an environmental temperature of $T_{\mathrm{E}} = 25\,°$C. When $T_E = 60\,°$C, the internal temperatures for all three K-values shown are greater than $40\,°$C, to be more precise, greater than $60\,°$C. From the results, three conclusions can be drawn. Firstly, a large K is highly desirable in devices without thermionic cooling since it means better thermal conduction that can quickly transport heat into surroundings. Secondly, the internal temperature may reach the maximum temperature in just a few seconds. Lastly, no matter how large K is, the internal temperature is higher than or equal to the environmental temperature. Before the device is turned on, the internal temperature equals the environmental temperature. When the device is turned on, the internal temperature will gradually become higher than the environmental temperature. This feature

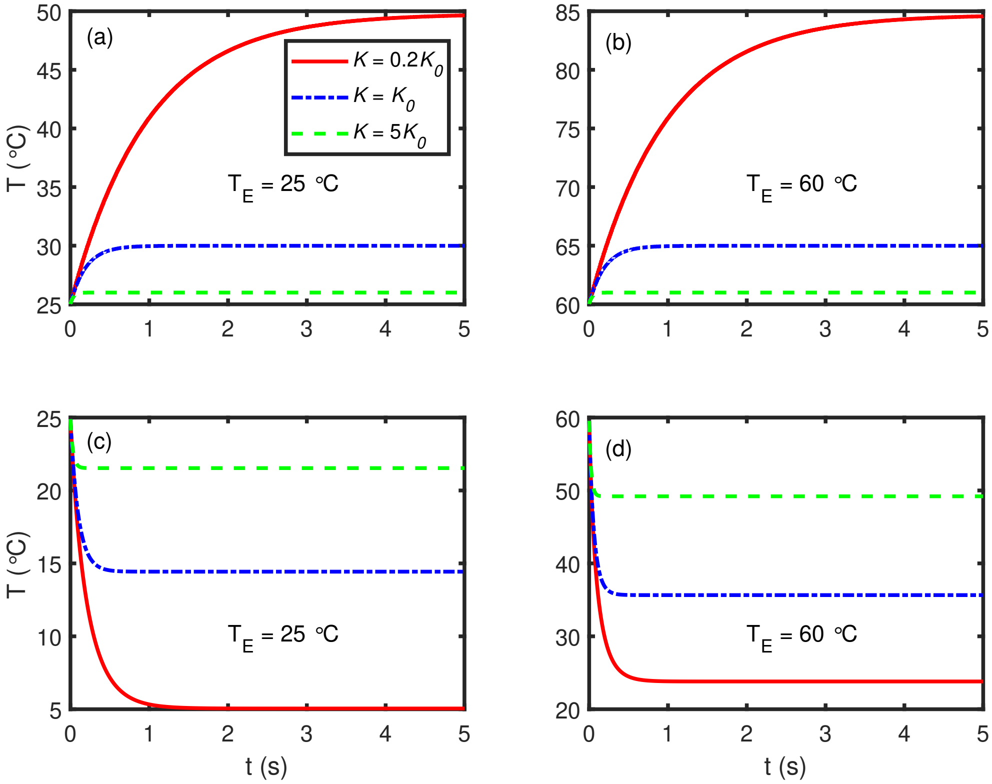

Figure 4.2: Time dependence of the internal temperature at three different values of K where the (a), (b) and (c), (d) are for the devices without and with thermionic cooling, respectively. In (a) and (b), the only difference is the environmental temperature; $T_E = 25\,°\mathrm{C}$ for (a) and $T_E = 60\,°\mathrm{C}$ for (b).

considerably hinders the applications of the devices. For example, if the environmental temperature is higher than 40 °C, then the internal temperature will always be higher than the highest working temperature.

To further study heat transfer in devices without thermionic cooling, the environmental temperature dependence of the maximum internal temperature is investigated. As it can be seen from Fig. 4.2, the internal temperature reaches the maximum temperature in just a few seconds. Therefore the maximum temperature can be obtained by measuring the internal temperature after the device has been operating for five seconds. The results are shown in Fig. 4.3. The maximum internal temperature shows a linear dependence on the environmental temperature and the slope is almost the same for three values of K. This is because the thermal conduction makes an overwhelm-

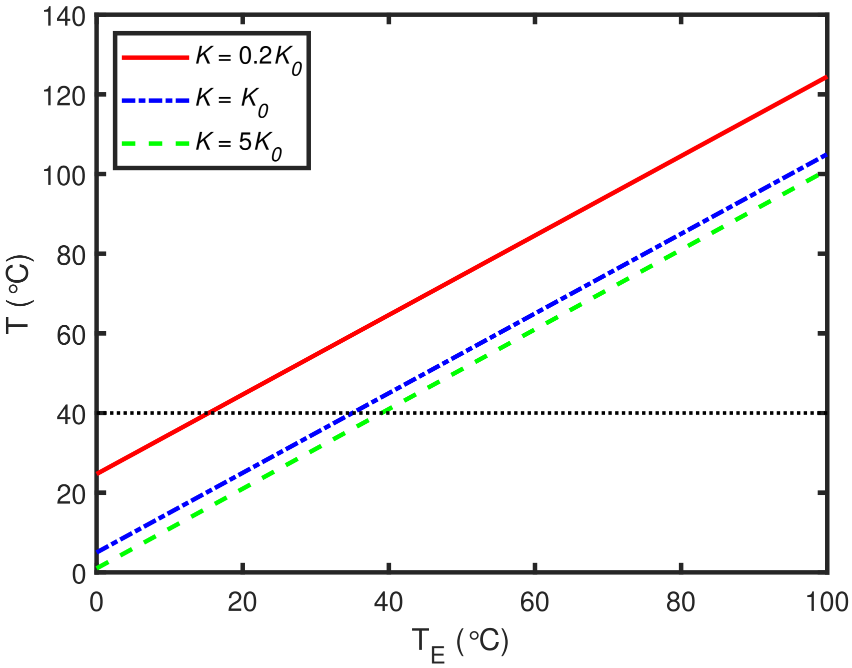

Figure 4.3: The environmental temperature dependence of the maximum internal temperature in devices without thermionic cooling.

ing contribution to the heat transfer. If we take away the contribution of the thermal radiation to the heat transfer, Eq. 4.6 can be analytically solved as

$$T = T_E + \frac{P_{in}}{2K} - \frac{P_{in}}{2K} \mathrm{e}^{\frac{-2Kt}{\rho d C_v}}. \tag{4.7}$$

When t goes to positive infinity, T has the maximum value, *i.e.* $T_{max} = T_E + P_{in}/2K$. The result indicates why the maximum internal temperature has a linear dependence on the environmental temperature, and the slope is independent of K. When $T_E = 0$, $T_{max} = P_{in}/2K$ also agrees with the result in Fig. 4.3. As we have mentioned, the maximum internal temperature should be lower than 40 °C to keep the device running well, resulting in a maximum environmental temperature T_{c1}. For $K = 0.2K_0, K_0$ and $5K_0$, the values of T_{c1} are 15 °C, 35 °C and 39 °C, respectively. The results indicate a larger K has a larger T_{c1}. This agrees well with intuitive physics since larger thermal conduction can transport internal heat into the environment more quickly than a smaller one. However, the value of K is limited by material properties and device structures.

Now, we are going to demonstrate that the maximum environmental temperature

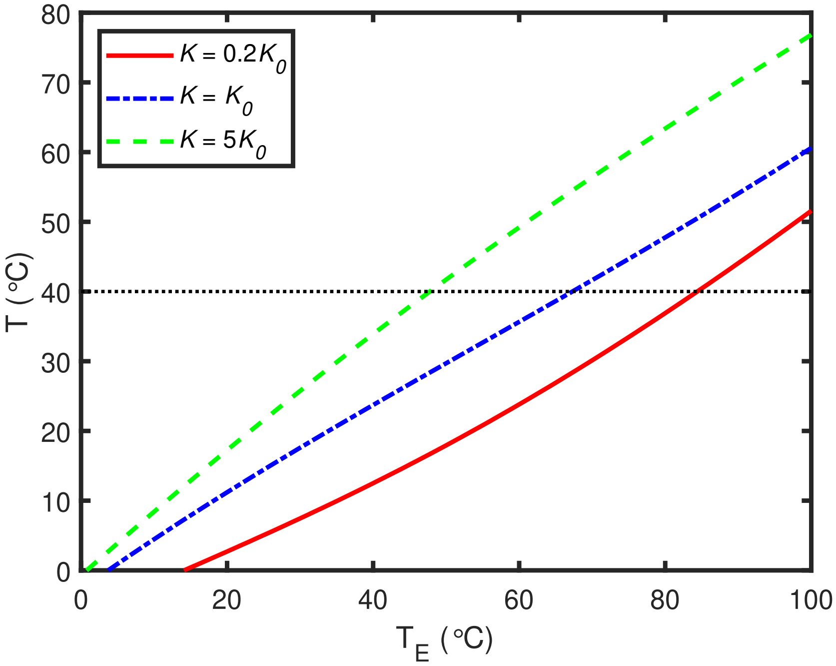

Figure 4.4: The environmental temperature dependence of the maximum internal temperature in devices with thermionic cooling.

that the device can operate well may be increased by employing thermionic cooling to transport heat. Unlike thermal radiation and thermal conduction, thermionic cooling can transport net heat from a cold object to a hot object [92]. This means the internal temperature can lower than the environmental temperature. When thermionic cooling is introduced, Eq. 4.6 can be rewritten as

$$\Delta T = \frac{2}{\rho d C_v}[\frac{P_{\mathrm{in}}}{2} - \epsilon\sigma(T^4 - T_{\mathrm{E}}^4) - K(T - T_{\mathrm{E}}) - J_Q]\mathrm{d}t, \tag{4.8}$$

where J_Q is the heat flow contributed by thermionic cooling, given by

$$J_Q = [(q\phi + 4k_{\mathrm{B}}T)J(T) - (q\phi + 4k_{\mathrm{B}}T_{\mathrm{E}})J(T_{\mathrm{E}})\mathrm{e}^{qV\beta}]/q. \tag{4.9}$$

The time dependence of the internal temperature at three values of K at $T_{\mathrm{E}} = 60\,^{\circ}\mathrm{C}$ is shown in Fig. 4.2. When $T_E = 25\,^{\circ}\mathrm{C}$, the internal temperature for three values of K is well below $40\,^{\circ}\mathrm{C}$. When $T_E = 60\,^{\circ}\mathrm{C}$, the maximum internal temperature is about $24\,^{\circ}\mathrm{C}$ and $36\,^{\circ}\mathrm{C}$ for $K = 0.2K_0$ and $K = K_0$, respectively, indicating that the thermionic enhanced devices can run well at $T_{\mathrm{E}} = 60\,^{\circ}\mathrm{C}$. For $K = 5K_0$, the maximum internal temperature is lower than the environmental temperature and higher than the highest running temperature. In devices without thermionic cooling, a larger K results in a lower internal temperature. However, in thermionic enhanced devices, a larger K results in a higher internal temperature. The fundamental reason is that the internal temperature is lower than the environmental temperature in thermionic enhanced devices. In such devices, a larger K accelerates the heat conduction from surroundings to the interior of the devices, leading to a higher internal temperature. Therefore, in thermionic enhanced devices, a smaller K is wanted instead of a larger one. Additionally, the internal temperature reaches the maximum temperature in just one second. In thermionic enhanced devices, there is also a maximum environmental temperature (T_{c2}). Obviously, T_{c2} is always higher than T_{c1}. Similarly, T_{c2} can be obtained by investigating the environmental temperature dependence of the maximum internal temperature, which is shown in Fig. 4.4. Here the maximum internal temperature is not linearly dependent on environmental temperature, which means that the thermionic cooling makes a comparable contribution to the heat transfer with thermal conduction. For $K = 0.2K_0, K_0$ and $5K_0$, the values of T_{c2} are 85 °C, 68 °C and 48 °C, respectively. In real devices, the internal temperature of a device should be reduced to 40 °C by thermionic cooling before the device is turned on. In this sense, the device can run below 40 °C at the entire time.

In thermionic enhanced devices, an external voltage is needed to drive the thermionic cooling, which consumes energy. The consumed power density P can be calculated by

$$P = J_{net}V, \tag{4.10}$$

where the $J_{net} = 2[J(T) - J(T_{\mathrm{E}})\mathrm{e}^{qV\beta}]$ is the net current density. The time dependence of P is shown in Fig. 4.5(a), where $T_E = 60$ °C. The curves share a rather similar trend with those in Fig. 4.2. The reason is that P depends only on T when V and T_{E} are fixed. Therefore, P and T share a similar time dependence. Combining Fig. 4.2 and Fig. 4.5, we find the device with the smallest K has the best performance in the thermionic cooling process, demonstrating the lowest internal temperature and the smallest consumed power. The underlying reason is found in Eq. 4.10, where a smaller T leads to a smaller P.

In order to characterize the cooling energy efficiency of the thermionic enhanced

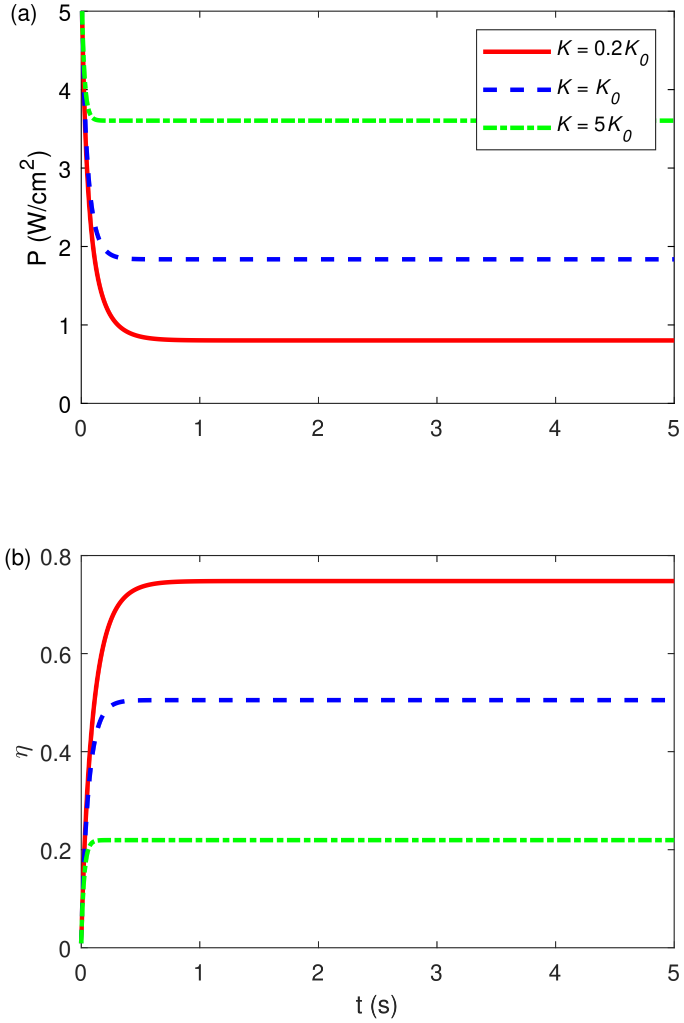

Figure 4.5: Time dependence of the consumed power in the thermionic cooling process (dashed line with left y-axis as indicated by the magenta dashed arrow) and the cooling energy efficiency (solid line with right y-axis as indicated by the solid magenta arrow), where $T_{\mathrm{E}} = 60\,^{\circ}\mathrm{C}$.

devices, a relative efficiency is defined as

$$\eta = \frac{J_Q}{P} \times \frac{T_{\mathrm{E}} - T}{T}, \tag{4.11}$$

where $T/(T_{\mathrm{E}} - T)$ is the Carnot efficiency. According to the equation, the time dependence of η is plotted in Fig. 4.5(b). The results show that η decreases with K, which indicates again that the thermionic enhanced device with the smallest K has the best performance in thermionic cooling. The energy efficiency is rather high, up to 75% of

Table 4.1: The critical environmental temperatures T_{c1} and T_{c2} for three values of K.

K	$0.2K_0$	K_0	$5K_0$
T_{c1}(°C)	15	35	39
T_{c2}(°C)	85	68	48

the Carnot efficiency. However, we should point out that the device with the smallest K has a rather low T_{c1} and this limits the applications of the device.

4.4 Conclusion

Without thermionic cooling, the maximum environmental temperature that a device can operate well is lower than the maximum running temperature. However, with the contribution of thermionic cooling, the maximum environmental temperature can be significantly higher than the maximum running temperature. Table 1 gives the values of T_{c1} and T_{c2} at three different values of K. For $K = 5K_0$, the device has a high T_{c1} and a low T_{c2}, indicating that thermionic cooling has a little effect. Indeed, the energy consumed by the process is high and the energy efficiency is low in such a device, as it can be seen in Fig. 4.5. That is to say, if a device has an excellent thermal conductivity performance, there is no need to employ thermionic cooling to accelerate the heat transfer. For $K = K_0$, the device has a relatively high T_{c1} and T_{c2}. This means that the device can normally operate without thermionic cooling and has great potential to work at higher environmental temperatures by employing thermionic cooling. For $K = 0.2K_0$, the device has a very small T_{c1} but a very large T_{c2}. This means thermionic cooling is needed even when the environmental temperature is considerably below the maximum running temperature. However, the device can operate at very high environmental temperatures when thermionic cooling is included. Additionally, the energy consumed by thermionic cooling is low, and the energy efficiency reaches about 75% of the Carnot efficiency. In this sense, if a device is designed to work at very high environmental temperatures, then a small K should be chosen. Theoretically, the device can run at even higher T_{E}, as long as we decrease the work function of the centre plane [92].

In summary, we have shown that the thermionic effect can be employed to enhance heat transfer in electronic devices. With thermionic cooling, the internal temperature of the devices may be considerably lower than the surrounding environmental temperature. In this sense, the operating temperature range of the devices may be significantly extended. The energy consumed by thermionic cooling and its energy efficiency are consonant with an excellent heat transfer performance. These findings promise to be useful in developing future electronic devices.

Chapter 5

Hot carrier relaxation in gapped Dirac semimetals

* In this chapter, we calculate the relaxation rate of hot carriers in a Cd_3As_2 semimetal with a finite gap. The quantization of the transverse momentum gives rise to a minimum gap at the Dirac point. Additional chemical doping further increases the gap. A finite gap relaxes the selection rule and gives rise to a nonvanishing internode coupling via phonon scattering. The gap also enhances the intra-node scattering. By using the Boltzmann transport equation, we find that the relaxation rate increases with the square of the gap and the electron temperature.

5.1 Introduction

Dirac semimetal Cd_3As_2 has attracted enormous attention due to its exotic electronic properties such as robust and universal optical absorbance, high electronic mobility ($\sim 10^6$ m/s) as well as a tunable carrier density through modification of the gate voltage. Recently, experimental work [69] shown a gap could be opened through the Cr element doping scheme. It was demonstrated that the bulk Dirac properties of Cd_3As_2 make it a promising material in optoelectronics, for example, optical switching.

In this chapter, we present a qualitative and quantitative analysis of hot carrier

---

* This chapter is based on S Huang, M Sanderson, J Tian, et al., Hot carrier relaxation in three dimensional gapped Dirac semi-metals, Journal of Physics D: Applied Physics, 51 (2017) 015101.

relaxation in a gapped Cd_3As_2 film. By considering the electron-phonon interaction in the Boltzmann transport equation, we calculated the energy loss of hot carriers. The hot carriers are excited by mid-infrared photons to the conduction band. We shall show that the fast relaxation of these hot carriers is strongly dependent on the size of the bandgap. For gapless Dirac semi-metals, the two nodes with opposite chirality are orthogonal and cannot be mixed by electron-phonon scattering. Opening a gap, however, introduces a finite inter-node overlap due to electron-phonon interaction. The inter-node transition contributes a term in the relaxation rate, which is proportional to the square of the gap. On the other hand, when the carrier concentration is fixed, increasing the gap will result in a higher Fermi level. This also leads to the relaxation rate increasing with the bandgap.

5.2 Electronic states and cooling of hot carriers

For gapped Cd_3As_2 thin films, the Hamiltonian is given by [113–115]

$$H = \begin{pmatrix} M_z k_z & A k_- & \Delta & 0 \\ A k_+ & -M_z k_z & 0 & \Delta \\ \Delta & 0 & -M_z k_z & -A k_- \\ 0 & \Delta & -A k_+ & M_z k_z \end{pmatrix}. \tag{5.1}$$

Here $k_\pm = k_x \pm i k_y = k_{xy} e^{\pm i\theta}$, θ is the angle between k_x and k_y. Due to quantization in the z direction, k_z is given by $n\pi/L$ where n denotes the n^{th} subband in the z direction and L is the thickness of the film. In our calculations, the following parameters are used, $M_z = 2\sqrt{M_0 M_1}$, $M_0 = 10$ meV, $M_1 = 9600$ meV·nm^2, $A = 275$ meV·nm and $L = 400$ nm. By diagonalizing the Hamiltonian, the energy-momentum dispersion is obtained by

$$\epsilon_\pm = \pm\sqrt{\epsilon_{nz}^2 + \epsilon_{xy}^2 + \Delta^2}, \tag{5.2}$$

where $\epsilon_{nz} = M_z k_z$, $\epsilon_{xy} = A k_{xy}$ and Δ is the band gap parameter. Corresponding eigenstates are obtained by $\Psi_{a=\pm}^{s=+} = (\epsilon_\pm + M_z k_z, A k_+, \Delta, 0)^T/\sqrt{R_\pm}$ and $\Psi_{a=\pm}^{s=-} = (0, \Delta, -A k_-, \epsilon_\pm + M_z k_z)^T/\sqrt{R_\pm}$, where we use $a = \pm$ to denote the valence and conduction band, and $s = \pm$ to denote spin up and down. $R_\pm$ are normalization constants of wave functions which are given by $R_\pm = A^2 k_{xy}^2 + \Delta^2 + (\epsilon_\pm + M_z k_z)^2$. The band structure of the Cd_3As_2 film is plotted in Fig. 5.1 by using Eq. 5.2, where the dashed horizontal line is the Fermi level (chemical potential μ). The blue and red curves are the 0^{th} and 35^{th} subbands in the z direction. A gap is opened at the Dirac point where $k_{xy} = 0$.

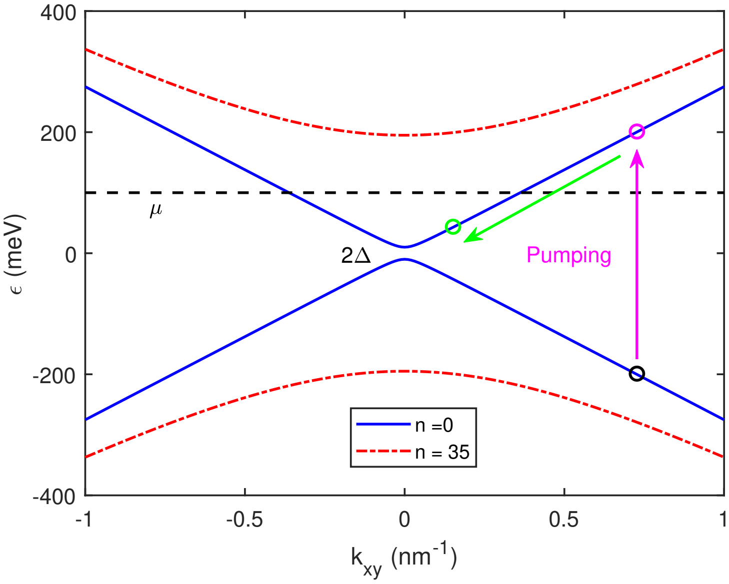

Figure 5.1: A band structure of the gapped Cd_3As_2 film along with hot electron relaxation process. Under laser pumping, ground state electrons are pumped to excited states, shown by the magenta arrow. Then, the excited electrons relax back to ground states, shown by the green arrow.

The pumping process and hot carriers relaxation process are presented schematically in Fig. 5.1. Under photon excitation, massive ground state electrons are pumped to excited states, shown by the vertical magenta arrow. The excited electrons establish a Fermi Dirac distribution via electron-electron coupling in a short time (of the order of 0.1 ps). At this stage, the electron temperature is far higher than the lattice temperature. Thus the excited electrons are named as hot electrons (hot carriers). According to the second law of thermodynamics, the hot electrons relax back to ground states and transfer energy to lattice via electron-phonon coupling, shown by the green arrow. Hot carrier relaxation is characterized by power loss P, which is defined as [70, 116]

$$P = \frac{\partial E}{\partial t} = \frac{\partial \sum_{k,a} \epsilon_{k,a} f_k^a}{\partial t} = \sum_{1}^{16} P_i, \tag{5.3}$$

where $\epsilon_{k,a}$ is the energy of an electron at a band with wave vector k and f_k^a is the Fermi

Dirac distribution. Hot carrier relaxation can be divided into sixteen types (P_i), listed in table. 5.1 according to its band, nodes, phonon and translation.

Table 5.1: Types of power loss, where intraband refers to hot electrons jumping from conduction band to conduction band, interband refers to hot electrons jumping from conduction band to valence band, intra-node refers to the jumping between nodes with the same spin, internode refers to the jumping between nodes with opposite spin. In the present work, we only evaluate intraband hot carrier relaxation marked with $\surd$.

No.	*band*	*node*	*phonon*	*translation*	evaluation
1	intraband	intra-node	acoustic	spontaneous	$\surd$
2	intraband	intra-node	optical	spontaneous	$\surd$
3	interband	intra-node	acoustic	spontaneous	$\times$
4	interband	intra-node	optical	spontaneous	$\times$
5	interband	inter-node	optical	spontaneous	$\times$
6	interband	inter-node	acoustic	spontaneous	$\times$
7	intraband	inter-node	optical	spontaneous	$\surd$
8	intraband	inter-node	acoustic	spontaneous	$\surd$
9	intraband	intra-node	acoustic	induced	$\surd$
10	intraband	intra-node	optical	induced	$\surd$
11	interband	intra-node	acoustic	induced	$\times$
12	interband	intra-node	optical	induced	$\times$
13	interband	inter-node	optical	induced	$\times$
14	interband	inter-node	acoustic	induced	$\times$
15	intraband	inter-node	optical	induced	$\surd$
16	intraband	inter-node	acoustic	induced	$\surd$

In gapless systems, there is no inter-node hot carrier relaxation due to the selection rules. In our system, a finite bandgap relaxes the selection rule and gives rise to a nonvanishing internode coupling via phonon scattering. Therefore, inter-node contributions should be taken into consideration.

To simplify the calculation, we firstly evaluate the induced transitions P_{ind}, and then the spontaneous transitions P_{spon} can be evaluated in the same way. Eight types of induced power loss are schematically shown in Fig. 5.2. Due to phonon velocity significantly less than Fermi velocity, interband transitions (P_3, P_4, P_5, P_6,) can be neglected, *i.e.* only intraband transitions need to be evaluated [116]. In the following parts, we will use inter and intra to denote inter-node and intra-node, respectively.

Usually, the energy of optical phonons is higher than that of acoustic phonon, which results in a critical temperature T_c. When the electronic temperature is around and above T_c, optical modes dominate the energy transfer. Otherwise, acoustic modes will play a dominant role. Here we mainly investigate the power loss contributed by acoustic modes.

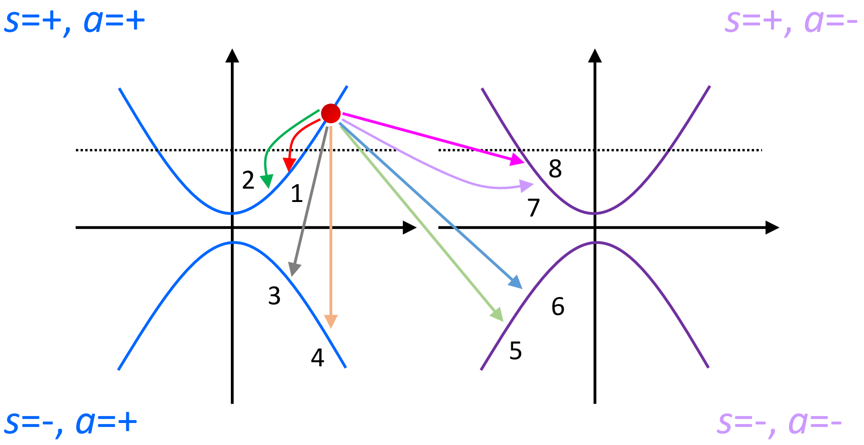

Figure 5.2: A schematic band structure for Cd_3As_2 where eight types of induced power loss are presented. In energy-momentum space, the spin up ($a = +$) and spin down ($a = -$) bands are degenerate.

The term P_i is given by [70]

$$\begin{aligned} P_i(\mu, T_e, T_L) = -2\pi \sum_{q,p} \int_0^\infty d\epsilon(\epsilon - \epsilon_p) N^L(\omega_q)(f(\epsilon) - f(\epsilon_p)) \\ \times \delta(\epsilon - \epsilon_p - \omega_q)\delta(\epsilon - \epsilon_{p+q}) w_q^i. \end{aligned} \tag{5.4}$$

Here ϵ and ϵ_p are the energy of the final state and initial state; $(\epsilon - \epsilon_p)$ is the energy difference for a carrier relaxation; $N^L(w_q)$ and $f(\epsilon)$ are the Bose-Einstein distribution for phonons and the Fermi-Dirac distribution for electrons, which measure the number of phonons and electrons in a particular state; $\delta(\epsilon - \epsilon_p - \omega_q)$ and $\delta(\epsilon - \epsilon_{p+q})$ are the energy and momentum conservation, respectively; T_e and T_L are the temperatures of the electrons and lattice, p and q are the wave vectors of electrons and phonons, $\omega_q = \hbar c_s q$ is the energy dispersion relation for the phonons and w_q^i is the transition rate for the final and initial states which is given by

$$w_q^i = \frac{\hbar^2 D^2 q^2 F^i(k,p)}{2\rho S w_q}, \tag{5.5}$$

where $D = 20$ meV is the deformation potential constant, ρ is the mass density of ions, and S is the area of the sample. $F^i(k,p)$ is the coupling term, which can be calculated by [72]

$$F(p,k) = | < \phi_p | \mathrm{e}^{-iqr} | \phi_k > |^2, \tag{5.6}$$

where p, k, q are the wave vectors of initial, final electrons and phonons, shown in Fig. 5.3; ϕ_p and ϕ_k are the wave functions of the initial and final states. We firstly use graphene wave function to show how to calculate the coupling term. The wave function of graphene is given by

$$\phi_k = \frac{1}{\sqrt{2}} \begin{pmatrix} 1 \\ e^{i\theta} \end{pmatrix} \mathrm{e}^{ikr}. \tag{5.7}$$

Plugging this into Eq. 5.6 gives

$$\begin{aligned} F(p,k) &= \frac{1}{4} |\mathrm{e}^{-ikr}(1, \mathrm{e}^{-i\theta_k}) \mathrm{e}^{iqr} \mathrm{e}^{ipr} \begin{pmatrix} 1 \\ e^{i\theta_p} \end{pmatrix} |^2 \\ &= (1 + \mathrm{e}^{i\theta_p - i\theta_k})(1 + \mathrm{e}^{-i\theta_p + i\theta_k}) \\ &= \frac{1 + \cos(\theta_p - \theta_k)}{2} = \frac{1 + \cos(\theta)}{2}, \end{aligned} \tag{5.8}$$

where θ is the angle between p and k. It is also possible to write the coupling term in p and q,

$$\begin{aligned} F(p,q) = F(p,k) &= \frac{1 + \cos(\theta)}{2} \\ &= \frac{1}{2}(1 + \frac{k + q\cos(\phi)}{|k+q|}), \end{aligned} \tag{5.9}$$

where $\tan(\theta_k) = k_y/k_x$, $\tan(\theta_p) = p_y/p_x$ and ϕ is the angle between p and q, $\cos(\theta) = \frac{p + q\cos(\phi)}{|p+q|}$.

Similarly, the coupling terms in Cd_3As_2 film are obtained by

$$F_{intra}(k,p) = \frac{x^2 + A^2(k^2 + p^2 - q^2)x + A^4 k^2 p^2}{4(\epsilon_p^2 + a\epsilon_p \epsilon_{nz})(\epsilon_k^2 + a\epsilon_k \epsilon_{mz})}, \tag{5.10}$$

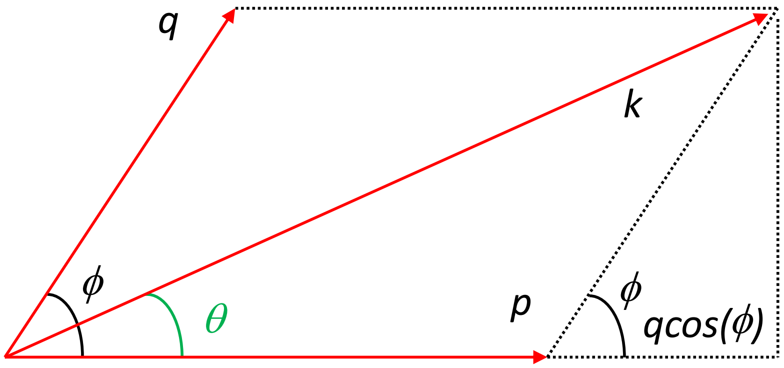

Figure 5.3: A schematic diagram of wave vectors, where ϕ is the angle between q and p, θ is the angle between k and p.

$$F_{inter}(k,p) = \frac{\Delta^2 v_F^2 q^2}{(2\epsilon_p^2 + 2a\epsilon_p\epsilon_{nz})(\epsilon_k^2 + a\epsilon_k\epsilon_{mz})}, \tag{5.11}$$

$$x = (a\epsilon_k + \epsilon_{nz})(a\epsilon_k + \epsilon_{mz}) + \Delta^2. \tag{5.12}$$

Here we have used an approximation $|p| \approx |k|$ to simplify the calculation since the sound velocity is significantly less than the Fermi velocity. $F_{intra}(k,p)$ is the coupling term for intra-node power loss P_1, P_2, P_3, P_4, P_9, P_{10}, P_{11} and P_{12}; $F_{inter}(k,p)$ is the coupling for the rest of power loss. It is clear that F_{inter} has a finite value when $\Delta \neq 0$ indicating the selection rule is released in the gapped Cd_3As_2 film.

After some algorithms, the intra and inter power loss due to the electron-acoustic phonon scattering are obtained by

$$\begin{aligned} P_{intra} = &-\frac{SD^2(k_BT_e - k_BT_L)}{4\rho\pi v_F^6\hbar^5}\sum_{n,m}\int_{\sqrt{\epsilon_{nz}^2+\Delta^2}}^{+\infty}\epsilon_{xy} \\ &\times \left(\frac{\partial f[\beta_e(\epsilon-\mu)]}{\partial\epsilon} + \frac{\partial f[\beta_e(\epsilon+\mu)]}{\partial\epsilon}\right)\int_0^{2\epsilon_{xy}} y^2 \\ &\times \frac{x^2 + A^2(k^2+p^2-q^2)x + A^4k^2p^2}{4(\epsilon_p^2 + a\epsilon_p\epsilon_{nz})(\epsilon_k^2 + a\epsilon_k\epsilon_{mz})}dy\,d\epsilon, \end{aligned} \tag{5.13}$$

$$
\begin{aligned}
P_{inter} = & -\frac{SD^2(k_BT_e - k_BT_L)}{4\rho\pi v_F^6\hbar^5}\sum_{n,m}\int_{\sqrt{\epsilon_{nz}^2+\Delta^2}}^{+\infty}\epsilon_{xy} \\
& \times (\frac{\partial f[\beta_e(\epsilon-\mu)]}{\partial\epsilon} + \frac{\partial f[\beta_e(\epsilon+\mu)]}{\partial\epsilon})\int_0^{2\epsilon_{xy}} y^2 \\
& \times \frac{\Delta^2 v_F^2 q^2}{(2\epsilon_p^2 + 2a\epsilon_p\epsilon_{nz})(\epsilon_k^2 + a\epsilon_k\epsilon_{mz})} dy d\epsilon,
\end{aligned} \tag{5.14}
$$

where K_BT_L and K_BT_e are the induced and spontaneous terms, respectively. When $T_L = T_e$, there is no hot carrier relaxation that agrees with our physical intuition. Further, $y = v_Fq$, $\beta_e = 1/(k_BT_e)$, m and n are the indexes of the subband in the z-direction, which present in x. In our calculation, Cd_3As_2 film is treated as a 2D material. We calculate the power loss for each subband in the z-direction and then sum them up to get the total power loss.

In the following section, we will discuss the power loss in different values of carrier density n_0. For each of n_0, there is a corresponding chemical potential μ. Now, we show how to use n_0 to determine μ. In the limit of $T = 0$, all states below and above the Fermi level (μ) are full and empty, respectively. Supposing the number of carriers in the i^{th} subband is Sn_i, then its Fermi radius can be determined as

$$
2 \times \frac{\pi k_{F,i}^2}{(\frac{2\pi}{L})^2} = \frac{Sk_{F,i}^2}{2\pi} = Sn_i, \tag{5.15}
$$

which generates

$$
n_i = \frac{k_F^2}{2\pi}. \tag{5.16}
$$

The chemical potential is the same for all the occupied subbands and it is obtained by

$$
\mu = \sqrt{\Delta^2 + \epsilon_{xy}^2 + \epsilon_{iz}^2} = \sqrt{\Delta^2 + A^2k_{F,i}^2 + i^2\epsilon_z^2}. \tag{5.17}
$$

From which, the Fermi radius is obtained for each subband

$$
k_{F,i}^2 = \frac{(\mu^2 - \Delta^2 - i^2\epsilon_z^2)}{A^2}. \tag{5.18}
$$

The total carrier density is the sum of carrier densities in all occupied subbands, which results in

$$
\begin{aligned}
n_0 &= \sum_0^K n_i = \sum_0^K \frac{k_F^2}{2\pi} = \sum_0^K \frac{\mu^2 - \Delta^2 - i^2\epsilon_z^2}{2\pi A^2} \\
&= \frac{1}{2\pi A^2}[(K+1)(\mu^2 - \Delta^2) - \frac{K(K+1)(2K+1)}{6}\epsilon_z^2].
\end{aligned} \tag{5.19}
$$

From which, the chemical potential is obtained by

$$\mu = \sqrt{\frac{2\pi A^2 n_0}{K+1} + \Delta^2 + \frac{K(2K+1)\epsilon_z^2}{6}}, \tag{5.20}$$

where $\epsilon_z = M_z\pi/L$. K is the index of the highest occupied subband, which is an implicit parameter. In order to obtain its value, we use a trial value and then test it. For $n_0 = 5 \times 10^{13}$ cm^{-2} and $\Delta = 0$, the chemical potential μ is about 119 meV and $K = 23$. When $T \neq 0$, the chemical potential can be approximately calculated by

$$\mu(T) = \mu(0)[1 - \frac{\pi^2}{12}(\frac{k_B T}{\mu(0)})^2]. \tag{5.21}$$

The equation above says the chemical potential decreases with temperature. Supposing $\mu(0) = 119$ meV, then $\mu(200\text{K})$ has a value of 0.98 $\mu(0)$. This indicates that μ has a small temperature dependence at the low-temperature area.

5.3 Results and discussion

The hot carrier relaxation is evaluated by solving Eq. 5.13 and Eq. 5.14. Bandgap dependence of P_{inter} and P_{intra} at three different values of carrier density are shown in Fig. 5.4(a) and (b), respectively. The results show there is no inter-node contribution to the power loss for $\Delta = 0$ due to the selection rule. When the selection rule is released by opening a bandgap, a finite P_{inter} is observed, and it increases with Δ. Increase the density of carriers, P_{inter} increases since more carriers contribute to the relaxation. Similarly, P_{intra} increases with Δ and n_0. However, P_{intra} has a finite value for $\Delta = 0$ because there is no section rule for intra-node relaxation.

The power loss, shown in Fig. 5.4, is the loss per unit volume, and it increases as the carrier density increases. Now we calculate the power loss per particle (P^s). The results are shown in Fig. 5.5. While P^s_{Inter} is zero for $\Delta = 0$ and increases with Δ, it decreases with n_0 that is considerably different from the results of P_{Inter}. The underlying reason is that the number of carriers below the Fermi level increases with n_0, and the power loss ability of these carriers is weaker than the carriers near the Fermi level. Thus, the average power loss per carrier decreases with n_0. For a small bandgap, P^s_{Intra} increases with the density. At a large gap, it decreases with the density. At small gap and low concentration, the chemical potential increase with the gap fast enough so that the total

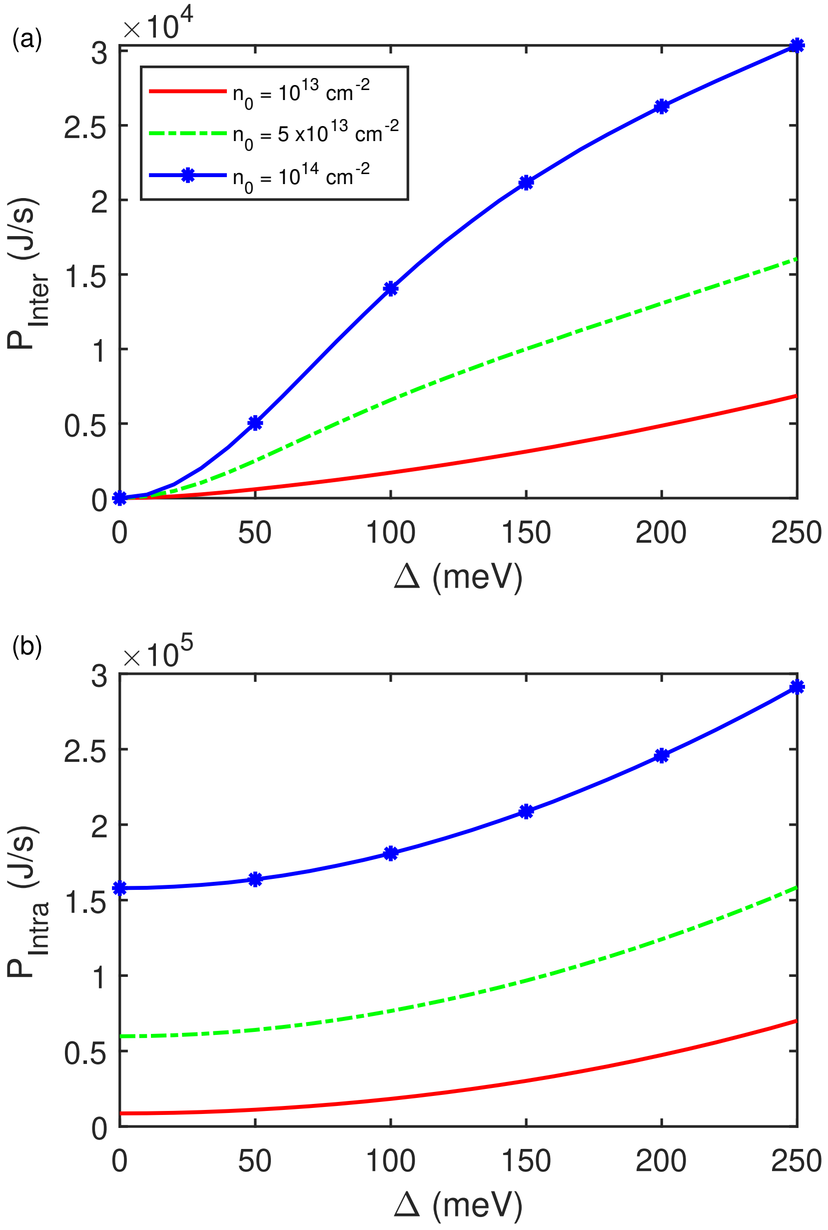

Figure 5.4: Bandgap dependence of (a) P_{inter} and (b) P_{intra} at three different values of carrier density n_0, where $T_e = 140$ K, $T_L = 77$ K and P_0 is the power loss for $\Delta = 0$.

power loss divided by the total carrier density increases with the carrier density. At large gap, the chemical potential increases with the density at a slower rate, resulting the increase of the total cooling power is slower than the increase of carrier density.

In order to obtain the contribution of internode transitions to the power loss, a

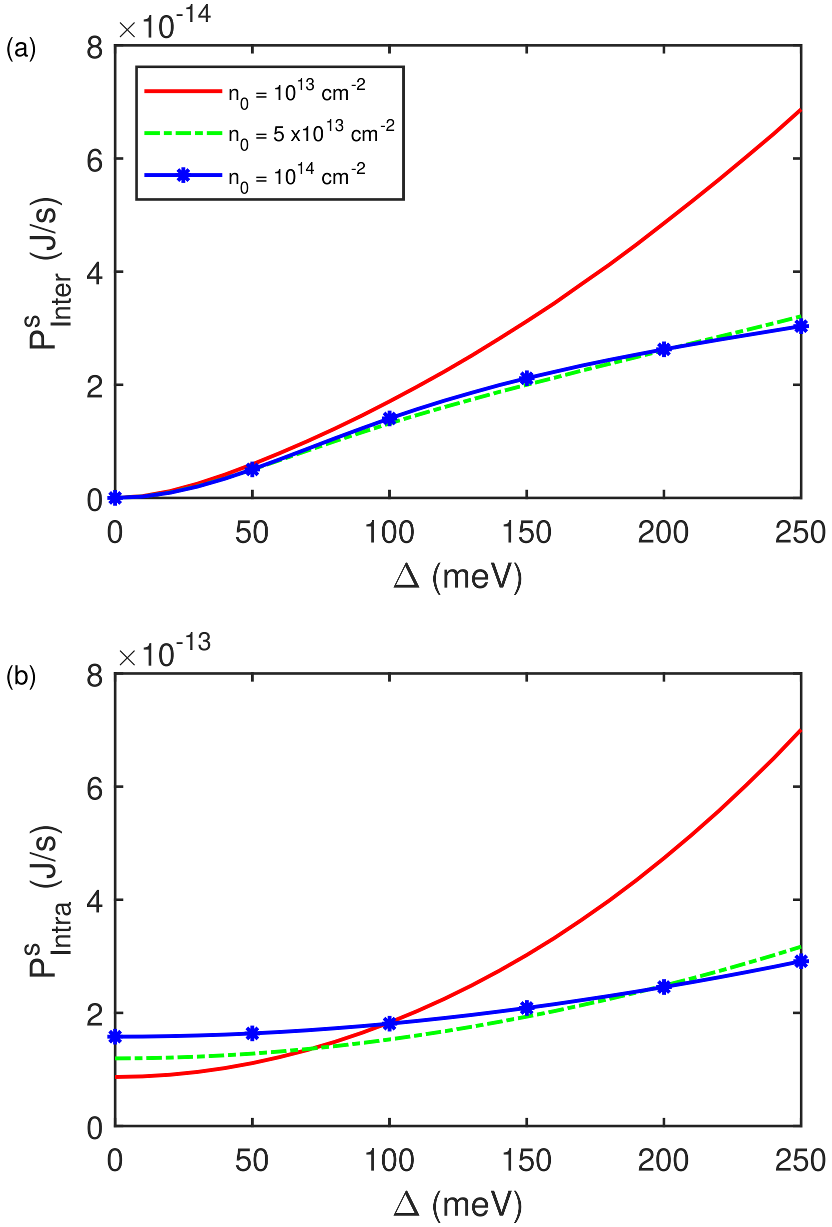

Figure 5.5: Bandgap dependence of (a) P^s_{Inter} and P^s_{Intra} at three different values of carrier density n_0, where $T_e = 140$ K and $T_L = 77$ K.

parameter $R_P = P_{inter}/P \times 100\%$ is introduced. The bandgap dependence of R_P and P at three different values of carrier density are shown in Fig. 5.6. The fractional contribution from the inter-node transition is less than 10% for all gap values, indicating that the intra-node transition dominates the hot carrier relaxation. The total energy loss rate as a function of the bandgap is presented in Fig. 5.6(b), which shows that the total power loss rate can be significantly enhanced by a band gap. The enhancement can be as large as 10 times when $\Delta = 250$ meV and $n_0 = 10^{13}$ cm^{-2}. For a fixed bandgap, the power loss increases with the carrier concentration. This is rather reasonable since more carriers mean that more hot electrons are jumping back to lower-energy states and losing energy to the lattice. The gap dependence is two-fold. (i) At a fixed carrier density, increasing the gap increases the chemical potential. For a fixed excitation energy, the energy difference between the hot electrons and the Fermi level decreases as the gap increases. This leads to faster cooling. (ii) The internode cooling increases with the gap as the overlap between different nodes increases. Both enhancements are proportional to the square of the gap. As a result, the total power loss increases with Δ^2. In order to see the parabolic band gap dependence, P as a function of Δ^2 at three values of n_0 is plotted in Fig. 5.7. The results confirm that the total power loss has parabolic dependence on the bandgap.

Fig. 5.8(a) shows the dependence of the power loss on the electron temperature with the lattice temperature $T_L = 77$ K. At a fixed lattice temperature, the power loss is determined by the temperature difference $T_e - T_L$. A large difference between the electron temperature and the lattice temperature leads to a fast energy exchange from the hot electrons to the lattice. Indeed, Fig. 5.8(a) shows P increases rapidly with the increase of T_e.

Here we define an energy relaxation time τ, which measures how fast the hot carriers loss their energy to the lattice at a constant power loss. We would like to point out that the energy relaxation time here is not the time that is needed by hot carriers to reach the lattice temperature. The τ is defined by

$$\tau = -\frac{E}{\partial E/\partial t} = -\frac{E}{P}, \tag{5.22}$$

where the total energy E is given by

$$E = \sum_{k,a} \epsilon_{k,a} f_k^a = \sum_{n=0}^{n=K} \int_{\sqrt{\Delta^2+\epsilon_{nz}}}^{\infty} \epsilon g(\epsilon) f(\epsilon) d\epsilon, \tag{5.23}$$

where $g(\epsilon) = \mathrm{S}\epsilon/(\pi A^2)$ is the density of states of subbands. The temperature dependence of τ is presented in Fig. 5.8.

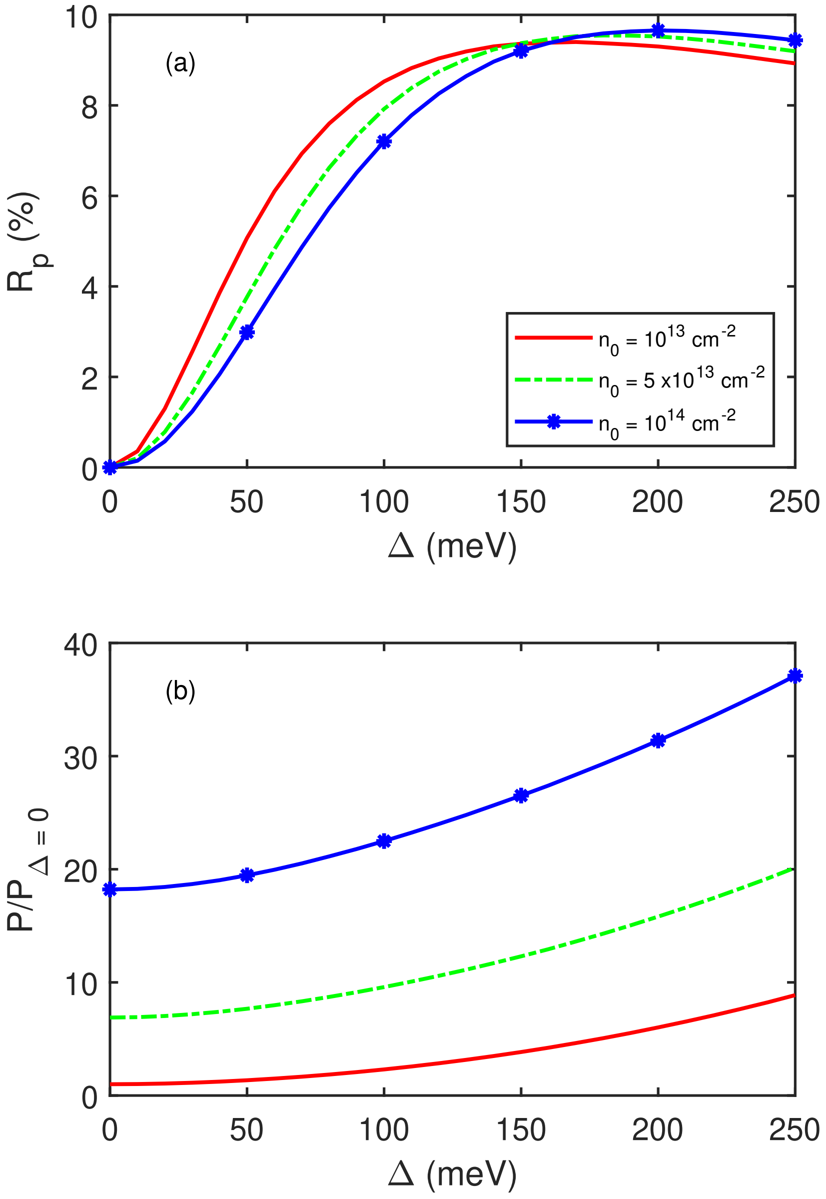

Figure 5.6: Bandgap dependence of (a) R_P and (b) P at three different valus of carrier density n_0, where $T_e = 140$ K, $T_L = 77$ K and P_0 is the power loss for $\Delta = 0$ and carrier density $n_0 = 10^{13}\text{cm}^{-2}$.

Now, we consider the relaxation due to the electron-optical phonon scattering. The energy carried by optical phonon is finite and approximately constant. Recent experimental work shows the optical phonon energy (15 meV) [69] in doped Cd_3As_2 is much smaller than that in graphene ($162 \sim 198$ meV) [117,118]. Hence, the interband contri-

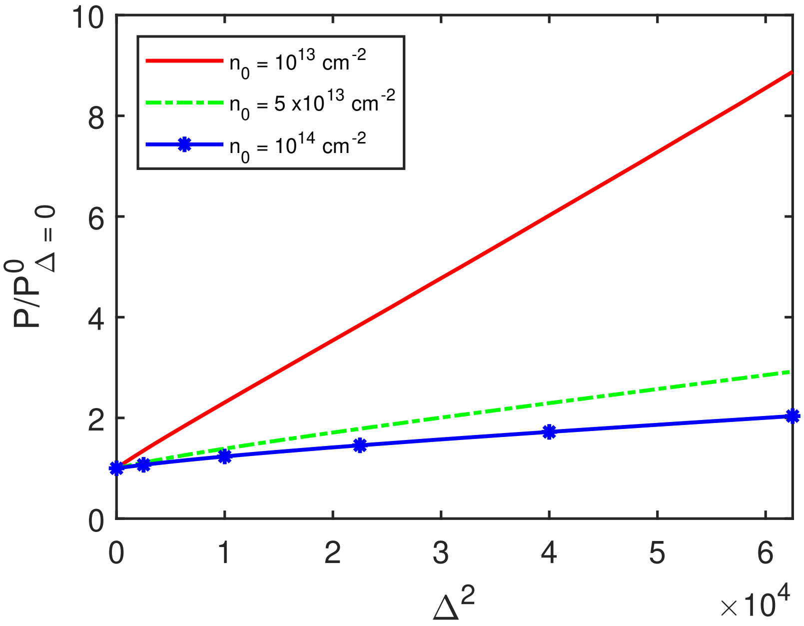

Figure 5.7: Total power loss as a function of Δ^2 at three value of carrier density, where $T_e = 140$ K, $T_L = 77$ K and P_0 is the power loss for $\Delta = 0$. We would like to point out that for different n_0, P_0 has a different value.

bution is zero in doped Cd$_3$As$_2$ where Fermi level is higher than 100 meV. The cooling power due to optical phonon scattering is given by

$$P_{op} = -\frac{1}{2\pi v_F^4 \hbar^5} \sum_{n,m} \int_{\sqrt{\epsilon_{nz}^2+\Delta^2}}^{+\infty} \epsilon_{xy} \int_0^{2\epsilon_{xy}+\omega_q} \omega_q^{op} \omega_q \\ \times [N_q^e(\omega_q) - N_q^L(\omega_q)](f(\epsilon) - f(\epsilon - \omega_q)) dy d\epsilon, \tag{5.24}$$

$$w_q^{op} = \frac{9\hbar^2 \gamma_0'^2 F(k,p)}{2\rho S w_0}. \tag{5.25}$$

Here w_q^{op} is the electron-optical phonon coupling constant [72] and $\gamma_0' = 40$ meV/ nm. The bandgap dependence of cooling power is determined by the coupling term $F(k,p)$ which is the same for optical and acoustic phonons. Therefore, the bandgap dependence of the cooling power is the same as that due to acoustic phonon scattering. The temperature dependence of the cooling power due to two different phonon scattering processes is shown in Fig. 5.9. The electron-optical phonon scattering rate is greater than that of acoustic phonon scattering rate. The main reason for this is that the energy of an

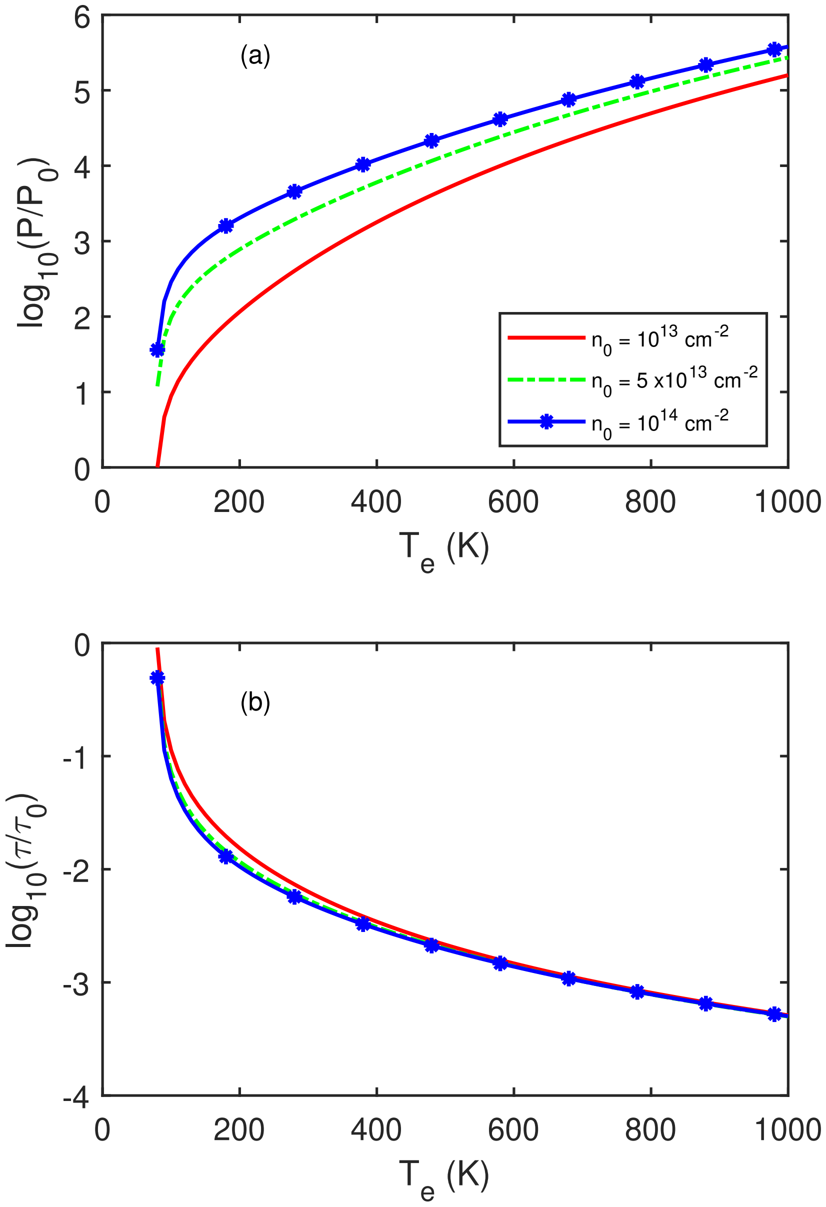

Figure 5.8: Temperature dependence of (a) power loss and (b) relaxation time at three different carrier densities, where $\Delta = 10$ meV, $T_L = 77$ K, P_0 and τ_0 are power loss and relaxation time for $T_e = 80$ K and carrier density $n_0 = 10^{13}\text{cm}^{-2}$, respectively.

optical phonons is small (15 meV) leading to a relatively small critical temperature (less than 77 K). Below the critical temperature, the power loss is dominated by acoustic phonon scattering since the optical phonons are frozen. Above this temperature, the

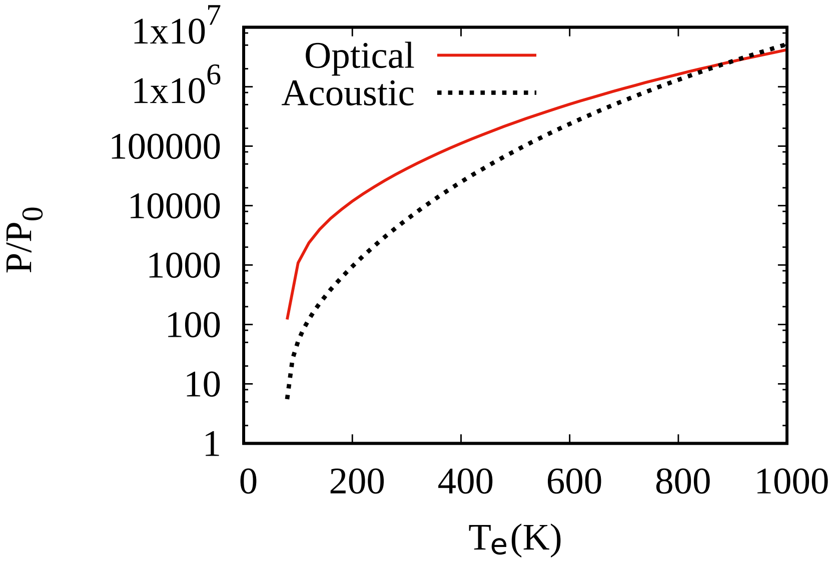

Figure 5.9: Temperature dependence of the electron power loss due to the acoustic and optical phonon scattering, respectively, where $\Delta = 10$ meV, $T_L = 77$ K and carrier density $n_0 = 10^{13}$ cm^{-2}.

optical phonon scattering rate is greater than that of the acoustic phonon scattering by 1 to 2 orders of magnitude unless the lattice temperature is very high. The result coincides with its counterpart in doped graphene [116]. It also indicates that the observed carrier relaxation is mainly due to optical phonon scattering.

5.4 Conclusion

In this chapter, we calculated the energy loss of hot carriers in 3D Dirac semimetals with a finite gap. The minimum gap is a result of transverse momentum quantization. Chemical doping further increases the gap. The hot carrier relaxation is mainly due to the electron-optical phonon interaction. The finite gap gives rise to both intra- and inter-node relaxation. At a fixed carrier concentration, the Fermi level increases with the gap. It is found that the relaxation rate increases as the gap, which agrees with experimental results. The power loss and τ have a strong dependence on electronic temperature, changing 3 or 4 orders of magnitude over a temperature range of ~ 1000 K. The temperature and gap dependence of the scattering rate due to the optical phonon scattering is similar to that due to the acoustic phonon scattering.

Chapter 6

Non-linear electromagnetic response in Semi-Dirac semimetals

* In this chapter, we demonstrate a strong and anisotropic photo-mixing effect in an electronic system whose energy-momentum dispersion is parabolic in the x-direction and linear in the y-direction, such as a $\mathrm{TiO_2/VO_2}$ multilayered structure. The third-order photoresponses along the linear and parabolic directions have been analyzed and determined quantitatively. We have found a remarkable tunability of the mixing efficiency along the parabolic direction by a small electric field in the linear direction, up to two orders of magnitude. In the terahertz (THz) regime, the third-order response is comparable to the linear response under an applied field of 10^3-10^4 V/cm. Additionally, the nonlinear response persists at room temperature. The results may have applications where different current responses are required along different directions in the THz regime.

6.1 Introduction

Terahertz (THz) technology has been proven to have promising applications in obtaining molecular spectral and material information due to energy matching [119, 120]. Although a number of THz emission mechanisms have been developed [121–124], the

---

* This chapter is based on S. Huang, M. H. Tran, J. Zuber, Q. Wang, Y. Zhu, C. Zhang, Strong tunable photomixing in semi-Dirac materials in the terahertz regime, JOSA B 36 (2) (2019) 200-203.

lack of high performance of THz resources is a hindrance in applications of THz technology [125]. Various nonlinear processes such as down-conversion and up-conversion have been used for emitting THz radiation [126].

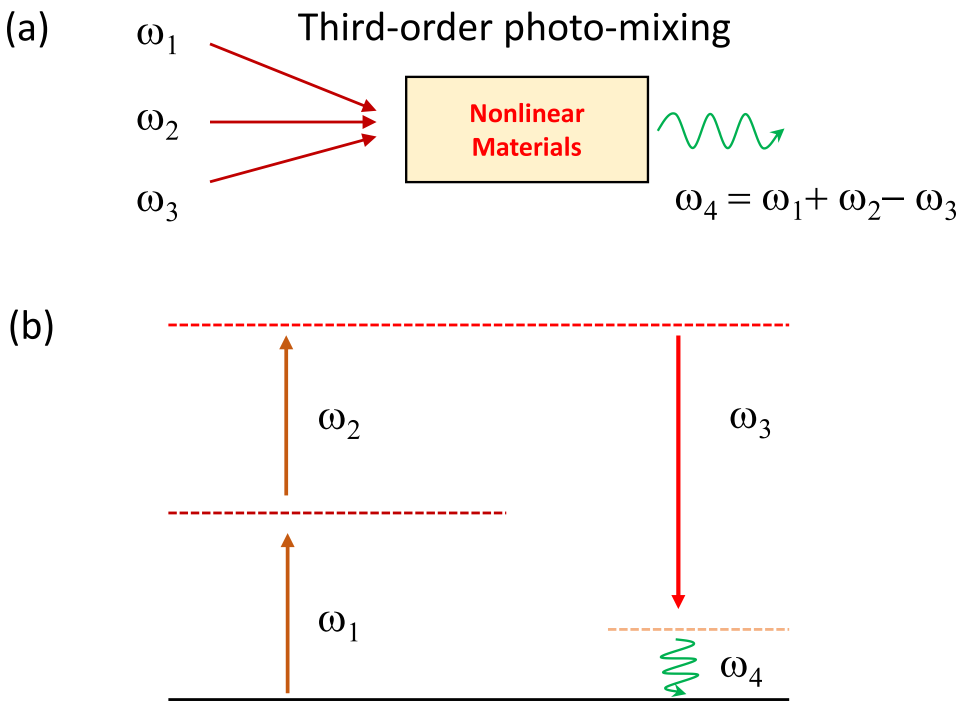

Figure 6.1: A schematic diagram of the down-conversion THz radiation process based on the third-order photo-mixing (a); Energy level diagram for the down-conversion process (b).

A schematic diagram of the down-conversion THz radiation process is presented in Fig. 6.1(a), where three incident photons (femtosecond laser) interact in a nonlinear material and produce a fourth photon in the THz regime. The process is also known as four-wave mixing since it involves four photons. Fig. 6.1(b) is the corresponding energy level diagram. In the process, the energy of the photons is conserved. Theoretically, the energy of the fourth photon (E_4) is the combinations of the incident energy (E_1, E_2, E_3) i.e.,

$$E_4 = | \pm E_1 \pm E_2 \pm E_3|. \tag{6.1}$$

For photons, their energy can be written as $E = \hbar\omega$. In this sense, Eq. 6.1 can be rewritten as

$$\omega_4 = | \pm \omega_1 \pm \omega_2 \pm \omega_3|. \tag{6.2}$$

There are two special cases. One is $\omega_4 = \omega_1 + \omega_2 + \omega_3$, which is known as the sum frequency generation. The other is $\omega_4 = \omega_1 + \omega_2 - \omega_3$, known as the difference frequency generation, where we have assumed $\omega_1 + \omega_2 > \omega_3$. This is the exact case shown in Fig. 6.1(a). In a difference frequency generation, ω_4 can be significantly smaller than ω_1, ω_2 and ω_3, which gives rise to THz radiation by using a femtosecond laser. The THz generation efficiency is charactered by the nonlinear effect (third-order nonlinear response) of nonlinear materials. Therefore, our investigations are focused on the third-order nonlinear response of nonlinear materials.

It has been demonstrated that graphene is a strong nonlinear material, due to its massless Dirac Fermion energy-momentum dispersion [126–129]. Additionally, a strong nonlinear effect [1] has been found in the bulk state of topological insulator HgTe/CdTe quantum wells, which arises from the non-parabolic energy-momentum dispersion. While Dirac systems generally show a stronger nonlinear optical effect and better photo-mixing efficiency compared to conventional systems with a parabolic energy-momentum dispersion, such systems usually have a low density of states near the Dirac point. In the case of graphene, the density of states vanishes at the Dirac point. The low density of states has limited the power generated in the nonlinear process. On the other hand, conventional electronic materials with parabolic energy dispersion have a weaker nonlinear response. It will be useful if the low efficiency can be significantly enhanced with the use of Dirac dispersion in some way. In this chapter, we will employ so-called semi-Dirac semimetals to achieve this purpose.

Recently, a unique energy-momentum dispersion was found in a VO_2-TiO_2 interface [130] and attracted enormous attention [131–134]. The new two-dimensional (2D) state possesses a semi-Dirac point that has a parabolic energy-momentum dispersion along the x-axis shown in Fig. 6.2(b) and has a linear energy-momentum dispersion along the y-axis shown in Fig. 6.2(c). For graphene with artificially designed hopping, a semi-Dirac energy dispersion can also occur [131]. Physical properties such as Faraday rotation, heat capacity, plasmon frequency [135], dynamical polarization [136], and optical conductivity [137] have been investigated in this unique system. Its plasmon frequency and optical conductivity are found to be highly anisotropic.

In this chapter, we analyze the photo-mixing properties of a semi-Dirac semimetal. By using a semi-classical approach where the quantum mechanically calculated energy dispersion is used to derive the velocity in the presence of an applied field along the x- and y-directions, we calculated the third-order current response involving three photons.

6.2 Models and current response

The energy-momentum dispersion of the semi-Dirac system is given as [137, 138]

$$\epsilon_0 = \pm 2mv_F^2 \sqrt{\frac{p_x^4}{(2mv_F)^4} + \frac{p_y^2}{(2mv_F)^2}}, \tag{6.3}$$

where ± is the index of the valence and conduction bands, m is the mass of a free electron, $v_F = 10^6$ m/s is the Fermi velocity, p_x and p_y are the momenta in the x and y directions, respectively. Based on Eq. 6.3, a band structure is plotted in Fig. 6.2(a), along with its projections in the x-z plane (b) and in the y-z plane (c), where $p_{xF} = \sqrt{2\mu m}$, $p_{yF} = \mu/v_F$ and $\mu = 0.04$ eV. In the limit $p_y = 0$, it has a parabolic energy-momentum dispersion, shown in Fig. 6.2(b). In the limit $p_x = 0$, it has a linear energy-momentum dispersion, shown in Fig. 6.2(c). The strong anisotropic energy-momentum dispersion results in an anisotropic nonlinear electromagnetic response. Therefore, the nonlinear electromagnetic response is evaluated in both the x- and y-directions.

The non-linear response is investigated under external fields $E = \sum_n E_0 \exp[i(q_n r - w_n t)]$, where E_0 is the magnitude of the external field, q_n and w_n are the n-th wave vector and frequency. Under the minimum coupling scheme [1], the momentum in the x- and y-directions is rewritten as $p_x + u_x$ and $p_y + u_y$, where $u_x = -eA_x$, $u_y = -eA_y$, A_x and A_y are electronic potentials, respectively. Additionally, the energy-momentum dispersion changes to

$$\epsilon = 2mv_F^2 \sqrt{\frac{(p_x + u_x)^4}{(2mv_F)^4} + \frac{(p_y + u_y)^2}{(2mv_F)^2}}. \tag{6.4}$$

Based on the energy-momentum dispersion, velocity of electrons in the x and y directions is calculated by

$$v_x = \frac{\partial \epsilon}{\partial p_x} = \frac{(p_x + u_x)^3}{mH}, \tag{6.5}$$

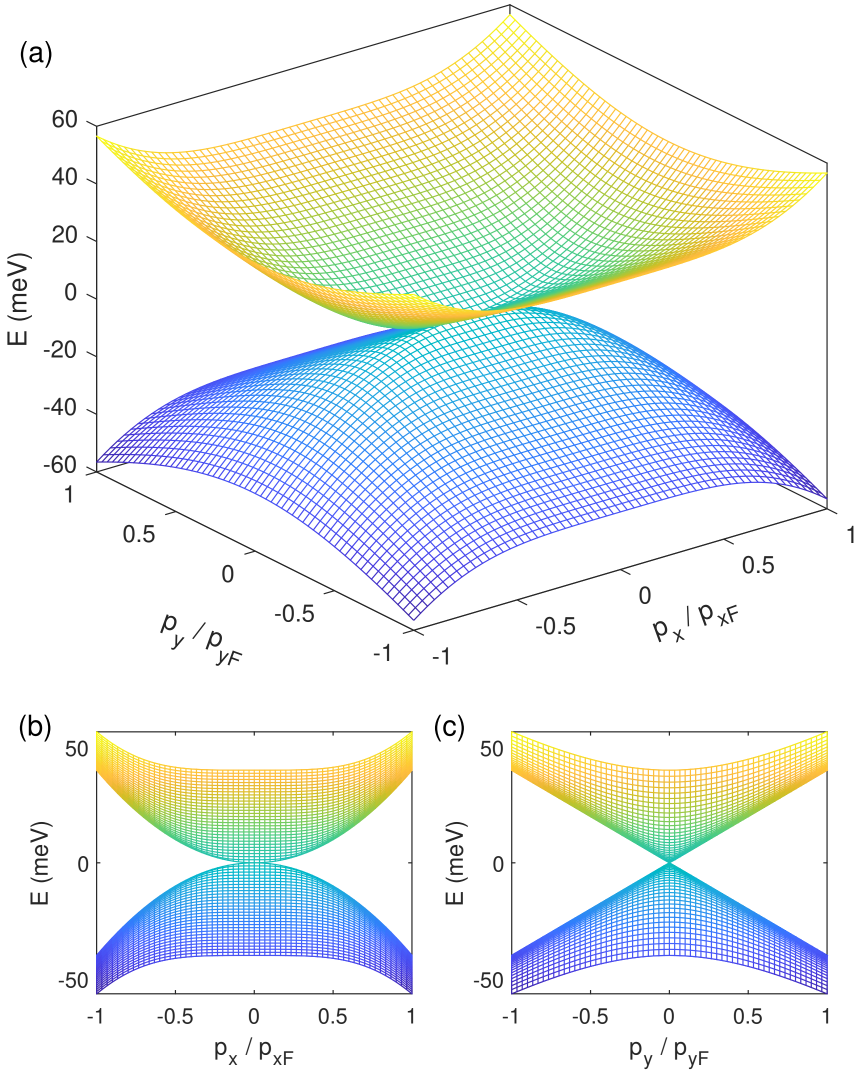

Figure 6.2: Band structures of the Semi-metal system (a); projection of the band structure in the x-z plane (b); projection of the band structure in the y-z plane (c). Here, $p_{xF} = \sqrt{2\mu m}$ and $p_{yF} = \mu/v_F$ are the Fermi momentum in the x and y directions and $\mu = 0.04$ eV.

$$v_y = \frac{\partial \epsilon}{\partial p_y} = \frac{(p_y + u_y)\epsilon_0}{H}, \tag{6.6}$$

where $\epsilon_0 = 2mv_F^2$ and $H = \sqrt{(p_x + u_x)^4 + 2m\epsilon_0(p_y + u_y)^2}$. The first- and the third-order velocity expansion in the x and y direction are given by (Calculation details can be found in Appendix A.1)

$$v_x^{(1)} = G_x^{(1)} = (\frac{3p_x^2}{mF} - \frac{2p_x^6}{mF^3})u_x - \frac{2\epsilon_0 p_x^3 p_y}{F^3}u_y, \tag{6.7}$$

$$\begin{aligned} v_x^{(3)} = \frac{1}{6}G_x^{(3)} &= (\frac{1}{mF} - \frac{17p_x^4}{mF^3} + \frac{36p_x^8}{mF^5} - \frac{20p_x^{12}}{mF^7})u_x^3 \\ &- (\frac{6\epsilon_0 p_x p_y}{F^3} - \frac{54\epsilon_0 p_x^5 p_y}{F^5} + \frac{60\epsilon_0 p_x^9 p_y}{F^7})u_x^2 u_y \\ &- (\frac{3\epsilon_0 p_x^2}{F^3} - \frac{18m\epsilon_0^2 p_x^2 p_y^2}{F^5} - \frac{6\epsilon_0 p_x^6}{F^5} + \frac{60m\epsilon_0^2 p_x^6 p_y^2}{F^7})u_x u_y^2 \\ &+ (\frac{6m\epsilon_0^2 p_x^3 p_y}{F^5} - \frac{20m^2\epsilon_0^3 p_x^3 p_y^3}{F^7})u_y^3, \end{aligned} \tag{6.8}$$

$$\begin{aligned} v_y^{(1)} &= -\frac{p_y\epsilon_0}{F^2}\frac{2p_x^3}{F}u_x + (\frac{\epsilon_0}{F} - \frac{p_y\epsilon_0}{F^2}\frac{2m\epsilon_0 p_y}{F})u_y \\ &= -\frac{2\epsilon_0 p_x^3 p_y}{F^3}u_x + (\frac{\epsilon_0}{F} - \frac{2m\epsilon_0^2 p_y^2}{F^3})u_y, \end{aligned} \tag{6.9}$$

$$\begin{aligned} v_y^{(3)} = \frac{1}{6}G_y^{(3)} &= (-\frac{2\epsilon_0 p_x p_y}{F^3} + \frac{18\epsilon_0 p_x^5 p_y}{F^5} - \frac{20\epsilon_0 p_x^9 p_y}{F^7})u_x^3 \\ &- (\frac{3\epsilon_0 p_x^2}{F^3} - \frac{18m\epsilon_0^2 p_x^2 p_y^2}{F^5} - \frac{6\epsilon_0 p_x^6}{F^5} + \frac{60m\epsilon_0^2 p_x^6 p_y^2}{F^7})u_x^2 u_y \\ &+ (\frac{18m\epsilon_0^2 p_x^3 p_y}{F^5} - \frac{60m^2\epsilon_0^3 p_x^3 p_y^3}{F^7})u_x u_y^2 \\ &- (\frac{m\epsilon_0^2}{F^3} - \frac{12m^2\epsilon_0^3 p_y^2}{F^5} + \frac{20m^3\epsilon_0^4 p_y^4}{F^7})u_y^3. \end{aligned} \tag{6.10}$$

The n-th order nonlinear response (current density) is calculated by

$$\begin{aligned} J^{(n)} &= e\int_{-\infty}^{+\infty}\int_{-\infty}^{+\infty} v^{(n)}[f(\epsilon_k) - f(\epsilon_k + \epsilon_{ph})]dk_x dk_y \\ &= \frac{e}{\hbar^2}\int_{-\infty}^{+\infty}\int_{-\infty}^{+\infty} v^{(n)}[f(\epsilon_k) - f(\epsilon_k + \epsilon_{ph})]dp_x dp_y, \end{aligned} \tag{6.11}$$

where $v^{(n)}$ is the n-th order velocity to the applied electronic field, $f(\epsilon_k)$ is the Fermi-Dirac distribution function, ϵ_{ph} is the total energy of the incoming photons. The equation is a modified version of $J = evn$, where the electron density n is replaced by the integral of the Fermi-Dirac distribution function $[f(\epsilon_k) - f(\epsilon_k + \epsilon_{ph})]$ in momentum space. It can be understood in a two energy level system, shown in Fig. 6.3. A ground-state electron jumps to a higher-energy state by absorbing a photon, shown by a red arrow. The probability of the jump is described by $P_0 f(\epsilon_k) \times [1 - f(\epsilon_k + \epsilon_{ph})]$, where

$f(\epsilon_k)$ is the probability that state ϵ_k is occupied, $[1 - f(\epsilon_k + \epsilon_{ph})]$ is the probability that state $\epsilon_k + \epsilon_{ph}$ is empty. At the same time, electrons would jump from the excited state to the ground state through radiation, shown by a blue arrow. The radiation probability is given by $P_0[1 - f(\epsilon_k)] \times f(\epsilon_k + \epsilon_{ph})$. In this sense, the net probability of electrons from state ϵ_k to state $\epsilon_k + \epsilon_{ph}$ is given by

$$\begin{aligned} P &= P_0 f(\epsilon_k) \times [1 - f(\epsilon_k + \epsilon_{ph})] - P_0[1 - f(\epsilon_k)] \times f(\epsilon_k + \epsilon_{ph}) \\ &= P_0[f(\epsilon_k) - f(\epsilon_k + \epsilon_{ph})], \end{aligned} \tag{6.12}$$

where P_0 is a dimensionless constant parameter that is omitted in Eq. 6.11. Due to the special properties of the Fermi Dirac function, $[f(\epsilon_k) - f(\epsilon_k + \epsilon_{ph})]$ only has a nonzero value near the chemical potential and has an axis of symmetry at $\mu + 0.5\epsilon_{ph}$, which can be seen from Fig. 6.4. This is an important condition, which considerably narrows down the domain of integration in Eq. 6.11. The effective domain of the integration are $[\mu - \epsilon_{ph}, \mu]$ and $[\mu - \epsilon_{ph} - 7k_BT, \mu + 7k_BT]$ for $T = 0$ and $T \neq 0$, respectively. Here $7k_BT$ is a cutoff value, which controls the accuracy of the integration.

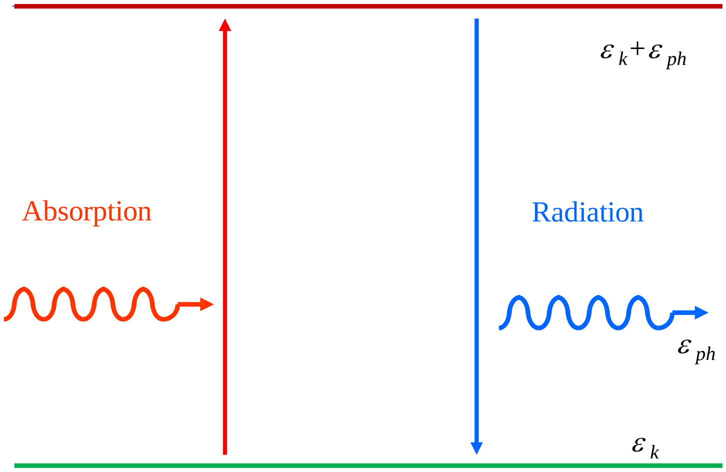

Figure 6.3: Electron absorption and radiation in a two energy level system.

Due to the symmetry of p_x and p_y in the Eq. 6.11, all terms containing odd exponents of p_x or p_y will obtain zero after integral. Hence $J^{(2)}$ is zero and $J^{(1)}$ can be written as

$$\begin{gathered} J_x^{(1)} = \frac{4e}{\hbar^2} \int_0^{+\infty} \int_0^{+\infty} (\frac{3p_x^2}{mF} - \frac{2p_x^6}{mF^3}) u_x \\ \times [f(\epsilon_k) - f(\epsilon_k + \epsilon_{ph})] dp_x dp_y. \end{gathered} \tag{6.13}$$

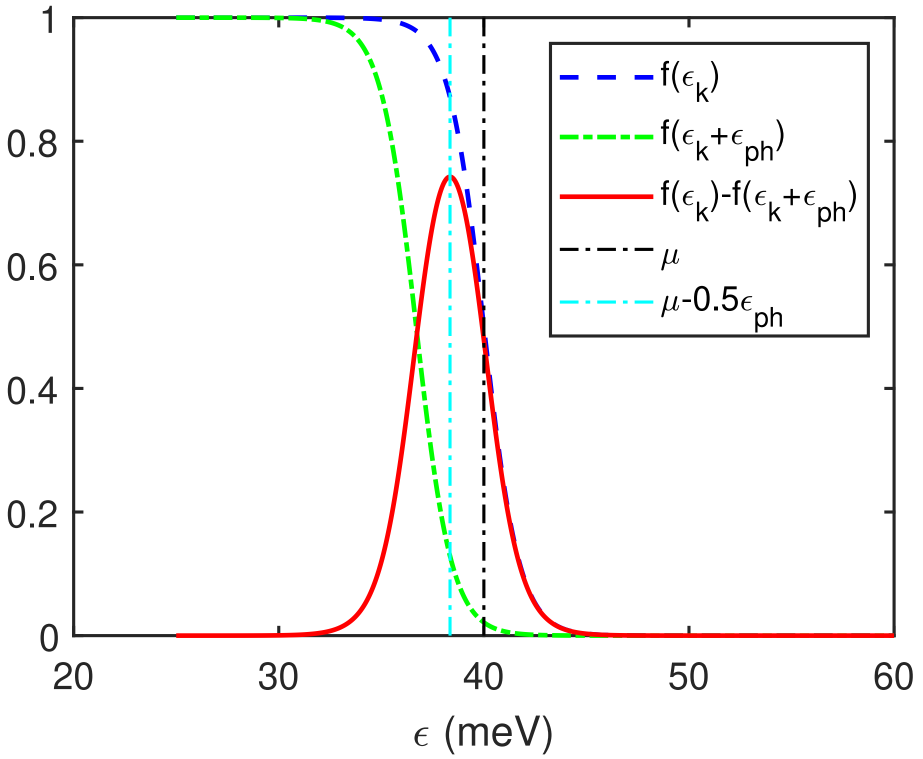

Figure 6.4: Fermi Dirac distribution function $f(\epsilon_k)$, $f(\epsilon_k+\epsilon_{ph})$ and function $f(\epsilon_k)-f(\epsilon_k+\epsilon_{ph})$, where the black dashed line is the chemical potential, and the cyan dashed line is the axis of symmetry for function $f(\epsilon_k)-f(\epsilon_k+\epsilon_{ph})$. The temperature is 10 K and $\epsilon_{ph} = 3.3$ meV (5 THz).

Here we define a Fermi momentum $p_{x0} = \sqrt{2m\mu}$ by equation $\mu = v_F\sqrt{\frac{p_x^4}{(2mv_F)^2}}$. Using the Fermi momentum to cancel out physical units, we obtain

$$J_x^{(1)} = \frac{4ep_{x0}^3}{m\hbar^2}\int_0^{+\infty}\int_0^{+\infty}(\frac{3x^2}{f}-\frac{2x^6}{f^3})u_{x0} \times [f(\epsilon_k)-f(\epsilon_k+\epsilon_{ph})]dxdy, \tag{6.14}$$

where $x = p_x/p_{x0}$, $y = p_y/p_{xo}$, $f = \sqrt{x^4+coe^2y^2}$, $coe^2 = 2m\epsilon_0/p_{x0}^2 = (2mv_F/p_{x0})^2$ and

$$u_{x0} = \frac{u_x}{p_{x0}} = \frac{eE}{\omega p_{x0}}, \tag{6.15}$$

$$\epsilon_k = v_F\sqrt{\frac{p_x^4}{(2mv_F)^2}+p_y^2} = v_Fp_{x0}\sqrt{\frac{x^4}{coe^2}+y^2}. \tag{6.16}$$

Similarly,

$$\begin{aligned} J_y^{(1)} = &\frac{4ep_{x0}^3}{m\hbar^2}\int_0^{+\infty}\int_0^{+\infty}(\frac{0.5coe^2}{f}-\frac{0.5coe^4y^2}{f^3})u_{y0} \\ &\times[f(\epsilon_k)-f(\epsilon_k+\epsilon_{ph})]dxdy, \end{aligned} \tag{6.17}$$

$$\begin{aligned} J_x^{(3)} = &\frac{4e}{\hbar^2}\int_0^{+\infty}\int_0^{+\infty}[(\frac{1}{mF}-\frac{17p_x^4}{mF^3}+\frac{36p_x^8}{mF^5}-\frac{20p_x^{12}}{mF^7})u_x^3-(\frac{3\epsilon_0p_x^2}{F^3}-\frac{18m\epsilon_0^2p_x^2p_y^2}{F^5} \\ &-\frac{6\epsilon_0p_x^6}{F^5}+\frac{60m\epsilon_0^2p_x^6p_y^2}{F^7})u_xu_y^2]\times[f(\epsilon_k)-f(\epsilon_k+\epsilon_{ph})]dp_xdp_y \\ = &\frac{4ep_{x0}^3}{m\hbar^2}\int_0^{+\infty}\int_0^{+\infty}[(\frac{1}{f}-\frac{17x^4}{f^3}+\frac{36x^8}{f^5}-\frac{20x^{12}}{f^7})u_{x0}^3 \\ &-(\frac{1.5coe^2x^2}{f^3}-\frac{4.5coe^4x^2y^2}{f^5}-\frac{3coe^2x^6}{f^5}+\frac{15coe^4x^6y^2}{f^7})u_{x0}u_{y0}^2] \\ &\times[f(\epsilon_k)-f(\epsilon_k+\epsilon_{ph})]dxdy, \end{aligned} \tag{6.18}$$

$$\begin{aligned} J_y^{(3)} = &\frac{4e}{\hbar^2}\int_0^{+\infty}\int_0^{+\infty}[-(\frac{3\epsilon_0p_x^2}{F^3}-\frac{18m\epsilon_0^2p_x^2p_y^2}{F^5}-\frac{6\epsilon_0p_x^6}{F^5}+\frac{60m\epsilon_0^2p_x^6p_y^2}{F^7})u_x^2u_y \\ &-(\frac{m\epsilon_0^2}{F^3}-\frac{12m^2\epsilon_0^3p_y^2}{F^5}+\frac{20m^3\epsilon_0^4p_y^4}{F^7})u_y^3]\times[f(\epsilon_k)-f(\epsilon_k+\epsilon_{ph})]dp_xdp_y \\ = &\frac{4ep_{x0}^3}{m\hbar^2}\int_0^{+\infty}\int_0^{+\infty}[-(\frac{1.5coe^2x^2}{f^3}-\frac{4.5coe^4x^2y^2}{f^5}-\frac{3coe^2x^6}{f^5} \\ &+\frac{15coe^4x^6y^2}{f^7})u_{x0}^2u_{y0}-(\frac{0.25coe^4}{f^3}-\frac{1.5coe^6y^2}{f^5}+\frac{1.25coe^8y^4}{f^7})u_{y0}^3] \\ &\times[f(\epsilon_k)-f(\epsilon_k+\epsilon_{ph})]dxdy. \end{aligned} \tag{6.19}$$

In what follows, we make two assumptions: first, we assume that the magnitude of three incoming photons is in the order of 10^3 V/cm. Secondly, we assume that the chemical potential is larger than 0.04 eV. The two assumptions guarantee that the value of u/p_0 is small enough to make the above velocity expansion valid, where p_0 is the Fermi momentum. We now consider a situation where three ultrafast fields (of the order of femtoseconds) are incident on the semi-Dirac system to generate a photo-response at a frequency (ω) in the THz regime.

6.3 Results and discussion

The first order current as a function of the electric field at two values of chemical potential is plotted in Fig. 6.5. Both J_{1x} and J_{1y} have a linear dependence on the amplitude of electric field E, which agrees with our physical picture. A larger E means more phonons are involved in the process, which results in a larger first order current. Besides, the number of phonons has linear dependence with E. That is why the first order current has linear dependence with E. There is saturation of E since the number of electrons near the Fermi level is finite.

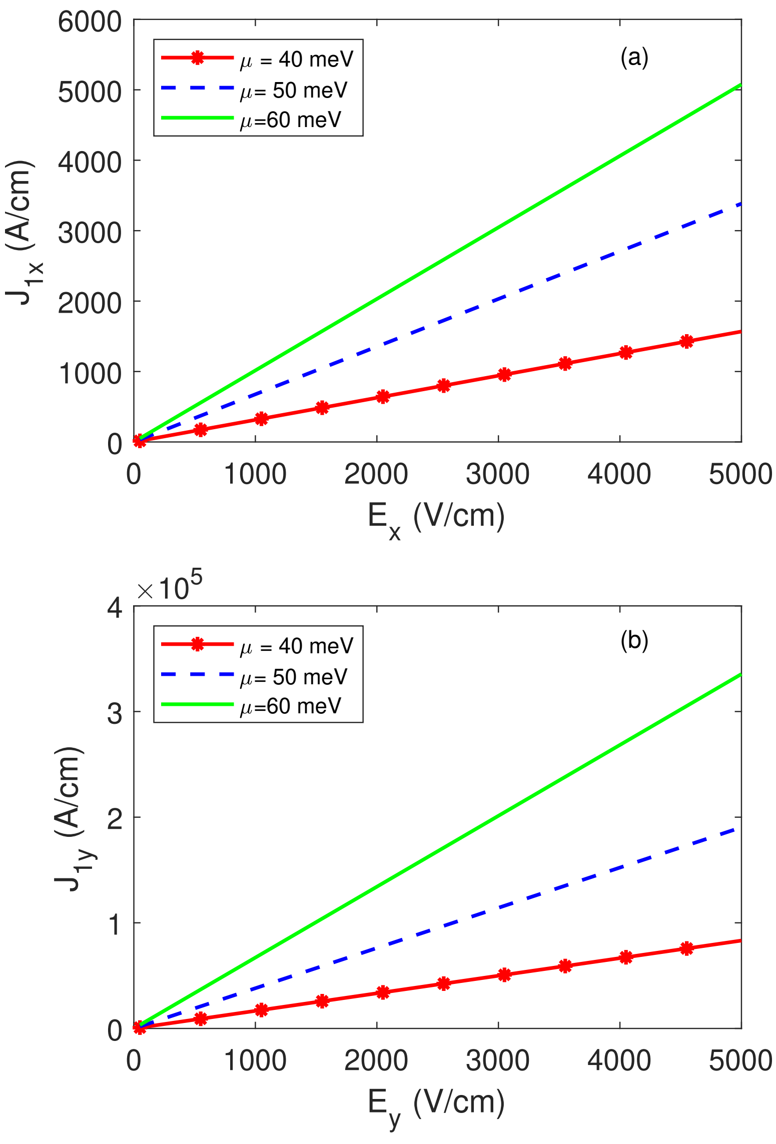

Figure 6.5: The first-order current as a function of the electric field; (a) J_{1x} where $E_y = 0$; (b) J_{1y} where $E_x = 0$.

When the chemical potential increases, the first order current increases for both J_{1x} and J_{1y}. The increase can be attributed to the enlargement of the integral domain. For the first-order response, the energy of phonon is $\epsilon_{ph} = \hbar\omega = \hbar \times 100$ THz $= 66$ meV. Therefore, the domain is [0, 40 meV] and [0, 50 meV] for $\mu = 40$ meV and $\mu = 50$ meV, shown in Fig. 6.6, respectively. We can image a physical picture where all electrons in the conduction band can contribute to the first order current. When the chemical potential is increased, there are more electrons in the conduction band, resulting in a larger first order current. The first order current in the y-direction is significantly larger than that in the x-direction. For $\mu = 0.04$ eV and $E_y = E_x = 5000$ V/cm, J_{1y}/J_{1x} is about 50. The main difference comes from the first order velocity in the x- and y-directions.

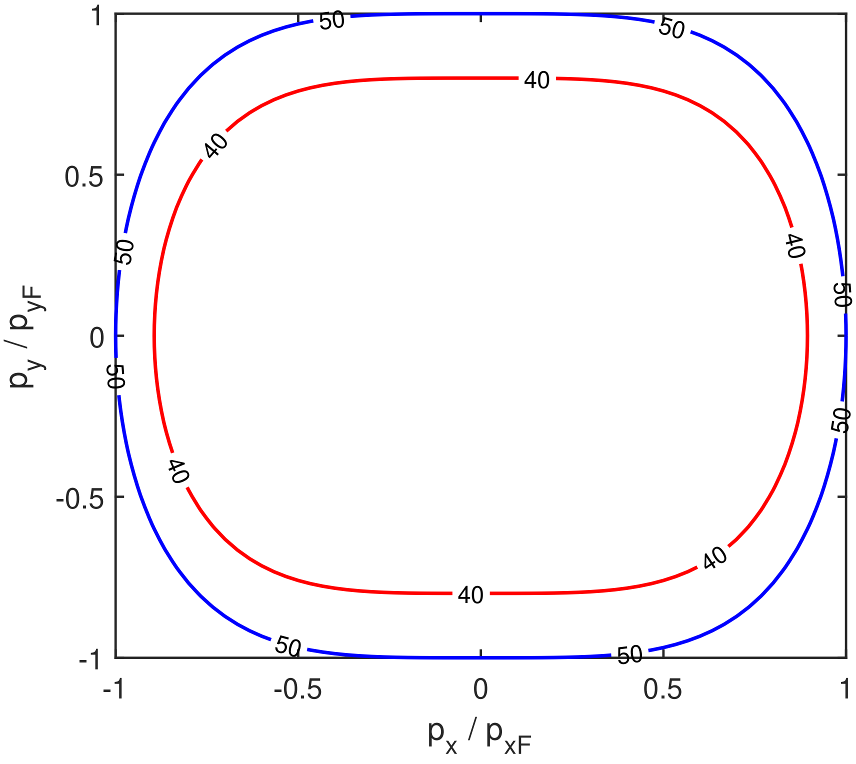

Figure 6.6: The integral domain of the first-order current in momentum space, where the area enclosed by the red line is for $\mu = 40$ meV and the area enclosed by the blue line is for $\mu = 50$ meV.

The third-order current as a function of the electric field at three values of chemical potential is plotted in Fig. 6.7(a) for J_{3x} and Fig. 6.8 for J_{3y}, respectively. The results

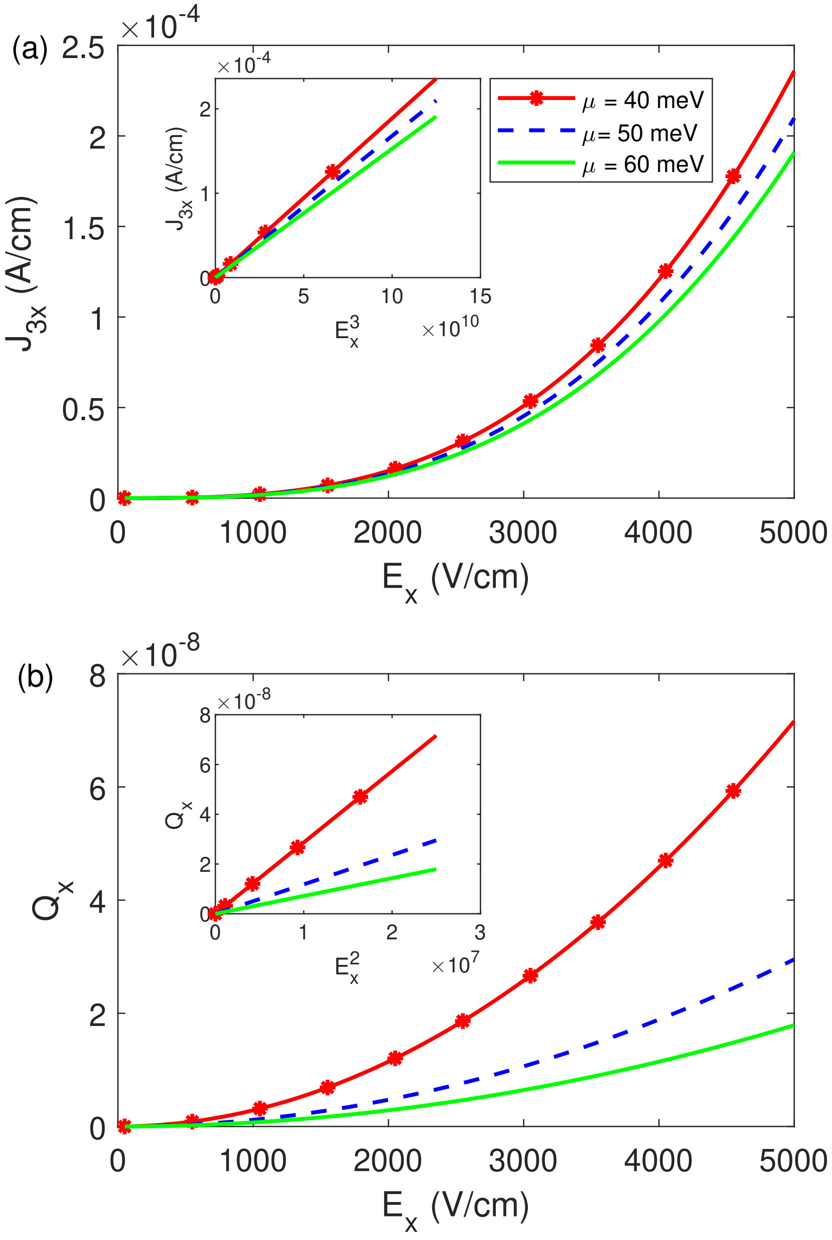

Figure 6.7: Electric field dependence of J_{3x} (a) and Q_x (b) at three values of chemical potential. The insets of (a) and (b) show the dependence of J_{3x} and Q_x on E_x^3 and E_x^2, respectively.

show that the third-order current in the x-direction with a parabolic energy-momentum dispersion is significantly smaller than that in the y-direction with a linear energy-momentum dispersion, by up to five orders. The third-order current has an exact cubic electric field dependence in the x and y directions shown in the inset of Fig. 6.7(a) and the inset of Fig. 6.8(a). For the third-order current, there are three incoming photons involved. Therefore, J_{3x} and J_{3y} have a cubic dependence on the number of incoming photons, i.e. the electric field E_x and E_y. The third order current decreases with chemical potential.

The third order current in graphene at $T = 0$ K is given by

$$J_3 = \frac{12e^4 v_F^2 E^3 \Delta}{\hbar^2 \mu^2 \omega^3}. \tag{6.20}$$

Calculation details are available in Appendix.3. The equation showes the third-order current density in graphene system has exactly cubic dependence on E and decreases with μ. The inset of Fig. 6.8(a) indicates J_{3y} of graphene is smaller than that of semi-Dirac semimetals.

To characterise the third-order photo-responses, a mixing efficiency is defined as

$$\begin{aligned} Q = \frac{J^{(3)}}{J^{(1)}} &= \frac{e \int\int v^{(3)}[f(\epsilon) - f(\epsilon + \hbar\omega)]\hbar\omega dk^2}{\hbar\omega J^{(1)}} \\ &= \frac{-e\hbar\omega \int\int v^{(3)} f'(\epsilon) dk^2}{J^{(1)}}. \end{aligned} \tag{6.21}$$

The photo-mixing efficiency as a function of the electric field is plotted in Fig. 6.7(b) and Fig. 6.8(b). The results show the photo-mixing efficiency in the x-direction is significantly larger than that in the y-direction, which agrees with our knowledge that materials with a parabolic energy-momentum dispersion demonstrate a weak nonlinear electric field response while those with a linear energy-momentum dispersion demonstrate strong nonlinear electric field response. Additionally, the photo-mixing efficiency has a parabolic dependence on the electric field, shown in the inset of Fig. 6.7(b) and the inset of Fig. 6.8(b). This is because of $Q_x = J_{3x}/J_{1x}$, where J_{3x} and J_{1x} have cubic and linear dependence on the electric field, respectively.

While the first-order current increases with electric field shown in Fig. 6.5, the third-order current decreases with electric field. As we have discussed, the integral domain is enlarged when increasing the chemical potential. The integral domain of the third-order current changes from [37 meV, 40 meV] to [47 meV, 50 meV] where $\epsilon_{ph} = \hbar\omega = \hbar \times 5$ THz ≈ 3 meV, which results a larger number of states in the momentum space being sampled, shown in the inset of Fig. 6.9. More available states would result in a larger third-order current, however we get a smaller one. This is because the third-order

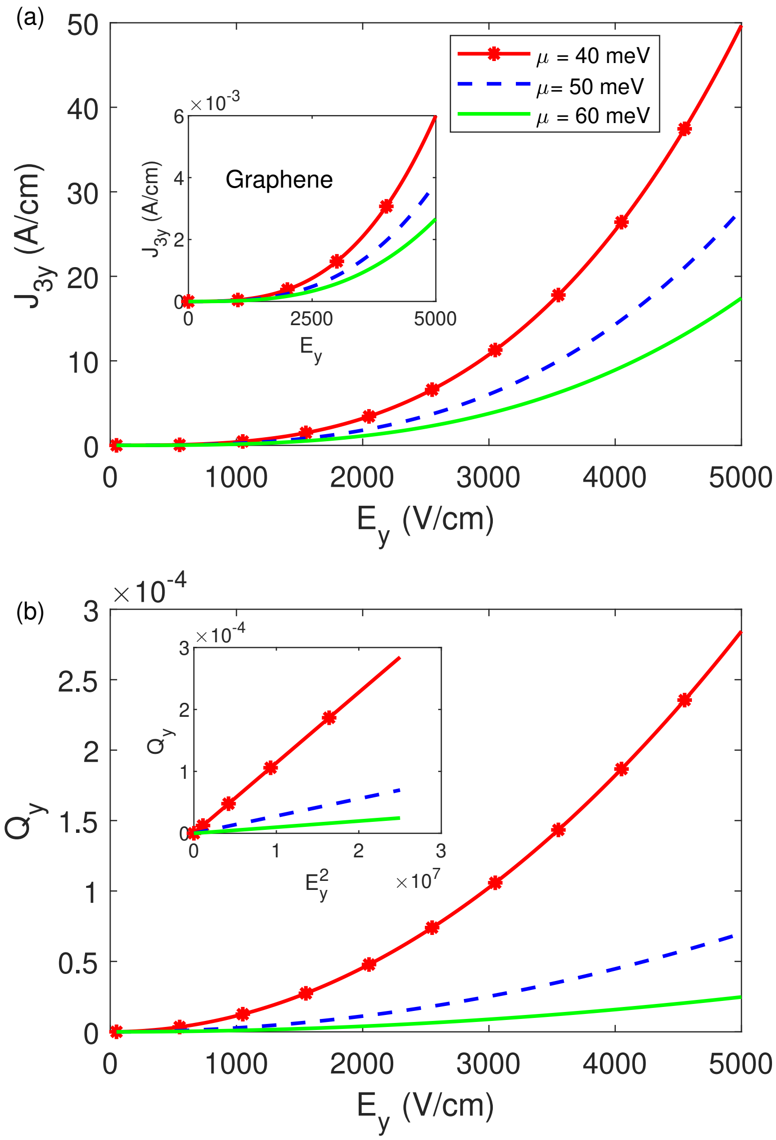

Figure 6.8: Electric field dependence of J_{3y} (a) and Q_y (b) at three values of chemical potential. The inset of (a) is electric field dependence of J_{3y} in graphene systems, and the inset of (b) showes the dependence of J_{3y} and Q_y on E_y^3 and E_y^2, respectively.

velocity ($\frac{1}{6}G^{(3)}$) decreases with ϵ. Fig. 6.9 shows $G_y^{(3)}$ decreases with ϵ when $p_x = 0$. We would like to point out that this is a rather simple situation. In fact, the third order current has a more complicated dependence on ϵ.

As we have discussed, the semi-Dirac system is strongly anisotropic in the energy-

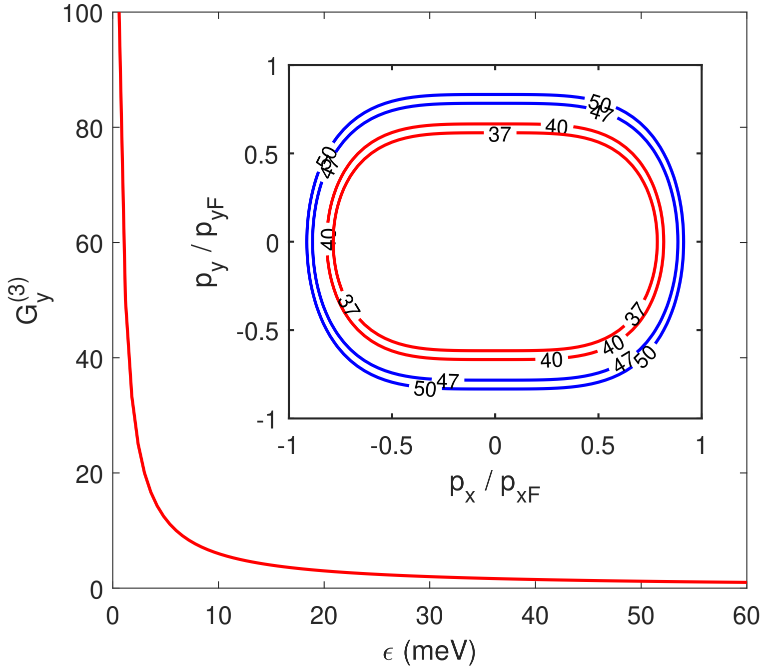

Figure 6.9: $G_y^{(3)}$ as a function of ϵ, where $p_x = 0$. The inset shows the domain of the third-order current, where the blue and red curves are equipotential lines for the energy. The integral domain of the third-order current is $[\mu - \epsilon_{ph},\ \mu]$ for $T = 0$. Consider the third-order response happens at 5 THz i.e., $\epsilon_{ph} = \hbar\omega \approx 3$ meV, the integral domain is [37 meV, 40 meV], the area enclosed by the red lines, and [47 meV, 50 meV], the area enclosed by the blue lines, for $\mu = 40$ meV and $\mu = 50$ meV, respectively.

momentum dispersion and the photo-mixing response. The anisotropic property results in the photo-mixing having a response to its vertical electric field. Q_x (Q_y) as a function of E_y (E_x) is plotted in Fig. 6.10. The results show the photo-mixing efficiency in the x-direction can be significantly enhanced by a small electric field in the y-direction. The enhancement can reach up to 50 times when the enhancement electric field is $0.2E_{y0}$. However, the photo mixing efficiency in the y-direction can be hardly enhanced by an electric field in the x-direction. The enhancement is almost zero for $E_x = 0.2E_{y0}$.

Here the benchmark is the enhancement in an isotropic system, where the photo-mixing efficiency is independent with electric field direction and proportional to the square of the electric field E^2, i.e.

$$Q = A(E_x^2 + E_y^2). \tag{6.22}$$

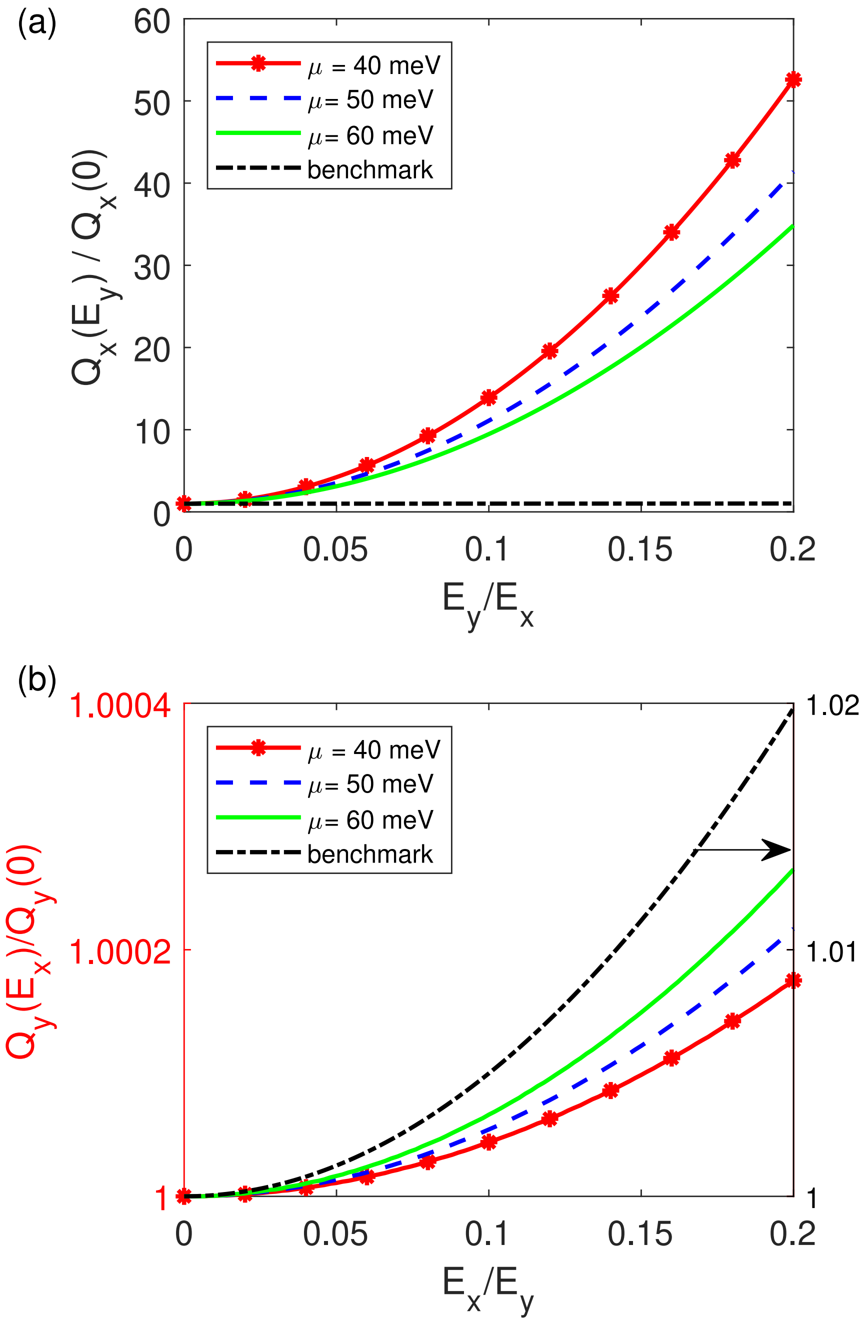

Figure 6.10: Q_x as a function of E_y (a) where $E_x = 5000$ V/cm, Q_y as a function of E_x (b) where $E_y = 5000$ V/cm, the right y axis is for benchmark indicated by a black arrow, and the left y axis is for rest curves.

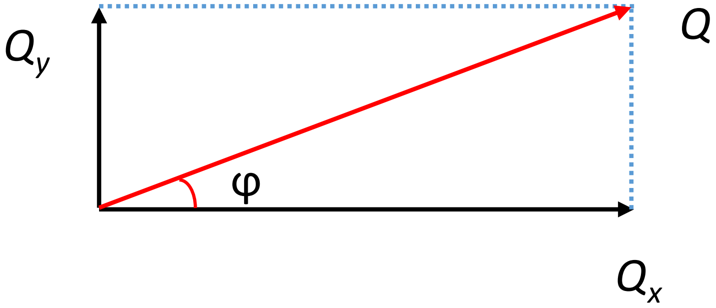

Figure 6.11: A schematic diagram shows the relationship among Q_x, Q_y and Q, where $\cos(\varphi) = \frac{E_x}{\sqrt{E_x^2+E_y^2}}$.

As shown in Fig. 6.11, its projection in the x direction can be calculated by

$$Q_x = Q\cos(\varphi) = A(E_x^2 + E_y^2) \times \frac{E_x}{\sqrt{E_x^2 + E_y^2}} = AE_x\sqrt{E_x^2 + E_y^2}. \tag{6.23}$$

The result shows a vertical electric filed can make a contribution to the photo-mixing efficiency even in an isotropic system. The benchmark is evaluated as

$$\frac{Q_x(E_y)}{Q_x(0)} = \frac{AE_x\sqrt{E_x^2 + E_y^2}}{AE_x^2} = \sqrt{1 + (\frac{E_y}{E_x})^2}. \tag{6.24}$$

$$\frac{Q_y(E_x)}{Q_y(0)} = \sqrt{1 + (\frac{E_x}{E_y})^2}. \tag{6.25}$$

The results in Fig. 6.10 show the benchmark is significantly larger than its counterparts in the x-direction and smaller than its counterparts in the y-direction of the semi-Dirac system.

The temperature dependence of J_{3x} at three values of chemical potential is plotted in Fig. 6.12, where the dashed black line is selected from [1] for topological insulator HgTe/CdTe quantum wells. J_{3x} firstly increases with T and then decreases with T. The initial increase is because electrons in the conduction band become more energetic and have more chance to contribute to the third-order current when the temperature is increased. Mathematically, the integral domain is enlarged from $[\mu - \epsilon_{ph},\ \mu]$ to $[\mu - \epsilon_{ph} - 7k_BT,\ \mu + 7k_BT]$ when the temperature is increased from 0 to T, which results in a larger integration. When the temperature is increased, $[f(\epsilon_k)$ - $f(\epsilon + \epsilon_{ph})]$

becomes more smaller, resulting in a smaller integration. Indeed, when the temperature is considerably increased, more and more electrons jump from ground states to higher-energy states. Therefore, the number of electrons at ground states and the number of empty states near the Fermi level decrease, which reduces the value of the third-order current. The competition of the above two mechanisms leads to the special temperature dependence of the third-order current. Additionally, there is an optimal T to produce a peak third-order current response. The optimal temperature increases from 50 K to 75 K as the chemical potential increases from 40 meV to 60 meV. Besides, the third-order current decreases more slowly for a larger μ. At the room temperature, the value of $J_{3x}(T)/J_{3x}(0)$ is 0.65, 0.59 and 0.49 for μ = 40 meV, 50 meV and 60 meV, respectively. In this sense, a large μ is preferred to produce a strong third-order photo-mixing in room temperature. The variation tendency of the third-order current density to temperature agrees previous results [1].

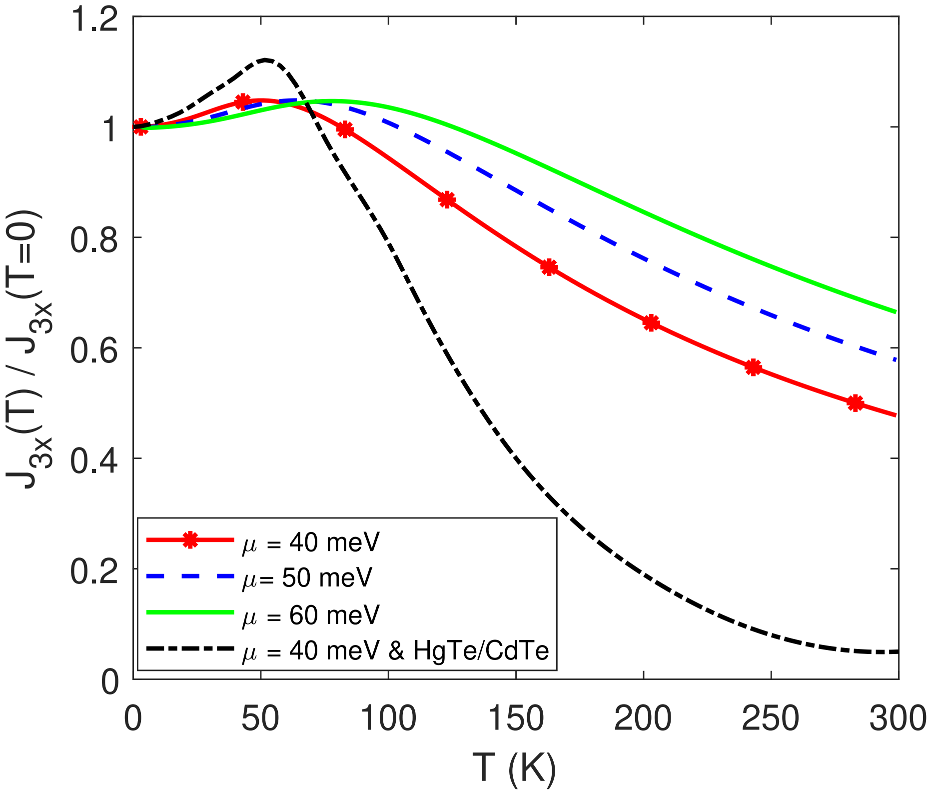

Figure 6.12: Temperature dependence of J_{3x} at three values of μ, where the dashed black line is selected from [1] for topological insulator HgTe/CdTe quantum wells.

6.4 Conclusion

We have systematically investigated the first-order and the third-order photo response in a semi-Dirac system whose energy-momentum dispersion is linear in the x-direction and is parabolic in the y-direction. Both the J_{1y}, J_{3y} and Q_y are considerably larger than their counterparts in the x-direction. We found the first order and the third-order current have linear and cubic electric field dependence. Consequently, the photo-mixing efficiency has a parabolic dependence on the electric field. While the first order current increases with the chemical potential, the third-order current and the photo-mixing efficiency decreases with the chemical potential. More importantly, the lower photo-mixing efficiency of electrons with a parabolic energy-momentum dispersion can be significantly enhanced if the electron energy-momentum dispersion perpendicular to the parabolic direction is linear. A small electric field along the linear direction can improve the mixing efficiency by two orders of magnitude. Our results suggest that the strength of the nonlinear electromagnetic response can be controlled by the weak field perpendicular to the direction of the third-order current. The enhancement is much greater than that in an isotropic parabolic system like conventional semiconductors and an isotropic linear system like graphene.

Chapter 7

Conclusion

In conclusion, we have systematically investigated thermionics in 3D Dirac and 3D nodal-ring semimetals. We have found the RD law no longer holds for both Dirac semimetals and nodal-ring semimetals due to their linear energy-momentum dispersion. Thermionic emission current in Dirac semimetals and nodal-ring semimetals is smaller than their counterparts in conventional materials due to their relatively smaller density of states near the Fermi level. However, the average energy carried by a degree of freedom in Dirac semimetals is twice that in conventional materials, which results in Dirac semimetals having a better thermionic efficiency than conventional materials. We calculate the heat transfer from electronic devices without and with thermionic cooling. Without thermionic cooling, the internal temperature of the devices is at best equal to and usually higher than the temperature of the surrounding environment. However, when thermionic cooling is employed to transport heat, the internal temperature can be considerably lower than the environmental temperature. In the thermionic cooling process proposed, energy efficiency can be as high as 75% of the Carnot efficiency.

We calculated the energy loss of hot carriers in 3D Dirac semi-metals with a finite band gap. The minimum band gap is a result of transverse momentum quantization. Chemical doping can further increase the band gap. The hot carrier relaxation is mainly due to the electron-optical phonon interaction. The finite band gap gives rise to both intra- and inter-node relaxation. It is found that the relaxation rate increases as the band gap increases, which agrees with experiment results.

The first-order and the third-order photo-response is investigated in a semi-Dirac system. We found that the lower photo-mixing efficiency of electrons with parabolic energy dispersion can be significantly enhanced if the electron energy dispersion perpendicular to the parabolic direction is linear. A small electric field along the linear direction can improve the mixing efficiency by two orders of magnitude. Compared with graphene, the semi-Dirac system has a stronger nonlinear effect at room temperature. Our results suggest that the strength of the nonlinear electromagnetic response can be controlled by the weak field perpendicular to the direction of the third-order current. This enhancement with a magnitude of up to two orders is much higher than that in isotropic systems.

Bibliography

[1] Q. Chen, Y. Sin Ang, R. Lewis, X. Wang, C. Zhang, Photomixing in topological insulator HgTe/CdTe quantum wells in terahertz regime, Applied Physics Letters 101 (21) (2012) 211109.

[2] K. v. Klitzing, G. Dorda, M. Pepper, New method for high-accuracy determination of the fine-structure constant based on quantized Hall resistance, Physical Review Letters 45 (6) (1980) 494.

[3] M. Z. Hasan, C. L. Kane, Colloquium: topological insulators, Reviews of Modern Physics 82 (4) (2010) 3045.

[4] Y. Chen, J. Analytis, J.-H. Chu, Z. Liu, S.-K. Mo, X.-L. Qi, H. Zhang, D. Lu, X. Dai, Z. Fang, et al., Experimental realization of a three-dimensional topological insulator, Bi_2Te_3, Science 325 (5937) (2009) 178–181.

[5] B. Yan, C. Felser, Topological materials: Weyl semimetals, Annual Review of Condensed Matter Physics 8 (2017) 337–354.

[6] Y. Ando, Topological insulator materials, Journal of the Physical Society of Japan 82 (10) (2013) 102001.

[7] H. Zhang, C.-X. Liu, X.-L. Qi, X. Dai, Z. Fang, S.-C. Zhang, Topological insulators in Bi_2Se_3, Bi_2Te_3 and Sb_2Te_3 with a single Dirac cone on the surface, Nature Physics 5 (6) (2009) 438–442.

[8] X.-L. Qi, S.-C. Zhang, Topological insulators and superconductors, Reviews of Modern Physics 83 (4) (2011) 1057.

[9] T.-T. Jia, M.-M. Zheng, X.-Y. Fan, Y. Su, S.-J. Li, H.-Y. Liu, G. Chen, Y. Kawazoe, Dirac cone move and bandgap on/off switching of graphene superlattice, Scientific Reports 6 (2016) 18869.

[10] C. Hwang, D. a. Siegel, S.-K. Mo, W. Regan, A. Ismach, Y. Zhang, A. Zettl, A. Lanzara, Fermi velocity engineering in graphene by substrate modification, Scientific Reports 2 (2012) 590.

[11] A. K. Geim, Graphene: Status and prospects, Science 324 (5934) (2009) 1530–1534.

[12] H. Min, J. E. Hill, N. A. Sinitsyn, B. R. Sahu, L. Kleinman, A. H. MacDonald, Intrinsic and Rashba spin-orbit interactions in graphene sheets, Physical Review B - Condensed Matter and Materials Physics 74 (16) (2006) 1–5.

[13] G. Kresse, J. Furthmüller, Efficiency of ab-initio total energy calculations for metals and semiconductors using a plane-wave basis set, Computational Materials Science 6 (1996) 15–50.

[14] J. P. Perdew, K. Burke, M. Ernzerhof, Generalized Gradient Approximation Made Simple, Physical Review Letters 77 (3) (1996) 3865–3868.

[15] S. Huang, X. Zhang, Y. Zhang, S. Hou, X. Yangi, Z. Zeng, Investigations of the mechanical properties of the Zr_8Ti_8 random alloy, International Journal of Modern Physics C 27 (07) (2016) 1650076.

[16] S. Huang, Y. Zhang, X. Zhang, Z. Wang, X. Yang, Z. Zeng, Mechanical properties of zirconium-based random alloys: Alloying elements and composition dependencies, Computational Materials Science 127 (2017) 60–66.

[17] C. Zhang, L. Chen, Z. Ma, Orientation dependence of the optical spectra in graphene at high frequencies, Physical Review B 77 (24) (2008) 241402.

[18] A. C. Neto, F. Guinea, N. M. Peres, K. S. Novoselov, A. K. Geim, The electronic properties of graphene, Reviews of Modern Physics 81 (1) (2009) 109.

[19] T. Stauber, N. Peres, A. Geim, Optical conductivity of graphene in the visible region of the spectrum, Physical Review B 78 (8) (2008) 085432.

[20] T. Wehling, A. M. Black-Schaffer, A. V. Balatsky, Dirac materials, Advances in Physics 63 (1) (2014) 1–76.

[21] M. Vazifeh, M. Franz, Electromagnetic response of Weyl semimetals, Physical Review Letters 111 (2) (2013) 027201.

[22] G. Mahan, L. Woods, Multilayer thermionic refrigeration, Physical Review Letters 80 (18) (1998) 4016.

[23] B. Lough, S. Lee, Z. Dou, R. Lewis, C. Zhang, Investigation into space charge effects in I–V characteristics of multi-layer semiconductor thermionic devices, Physica E: Low-dimensional Systems and Nanostructures 17 (2003) 651–653.

[24] M. F. O'dwyer, R. Lewis, C. Zhang, T. Humphrey, Electronic efficiency in nanostructured thermionic and thermoelectric devices, Physical Review B 72 (20) (2005) 205330.

[25] G. Mahan, Thermionic refrigeration, Journal of Applied Physics 76 (7) (1994) 4362–4366.

[26] I. Langmuir, The effect of space charge and residual gases on thermionic currents in high vacuum, Physical Review 2 (6) (1913) 450.

[27] F. Jin, D. Carter, Thermionic cooling efficiency of functionalized carbon nanotube thin films, Journal of Vacuum Science & Technology B, Nanotechnology and Microelectronics: Materials, Processing, Measurement, and Phenomena 36 (5) (2018) 051804.

[28] F. Jin, A. Beaver, Barium strontium oxide functionalized carbon nanotubes thin film thermionic emitter with superior thermionic emission capability, Journal of Vacuum Science & Technology B, Nanotechnology and Microelectronics: Materials, Processing, Measurement, and Phenomena 35 (4) (2017) 041202.

[29] Y. Ang, S.-J. Liang, L. Ang, Theoretical modeling of electron emission from graphene, MRS Bulletin 42 (7) (2017) 505–510.

[30] F. Zhu, X. Lin, P. Liu, K. Jiang, Y. Wei, Y. Wu, J. Wang, S. Fan, Heating graphene to incandescence and the measurement of its work function by the thermionic emission method, Nano Research 7 (4) (2014) 553–560.

[31] F. Morini, E. Dubois, J.-F. Robillard, S. Monfray, T. Skotnicki, Low work function thin film growth for high efficiency thermionic energy converter: Coupled Kelvin probe and photoemission study of potassium oxide, Physica Status Solidi (a) 211 (6) (2014) 1334–1337.

[32] M. Trushin, Theory of photoexcited and thermionic emission across a two-dimensional graphene-semiconductor schottky junction, Physical Review B 97 (19) (2018) 195447.

[33] X. Zhang, Y. Pan, J. Chen, Parametric optimum design of a graphene-based thermionic energy converter, IEEE Transactions on Electron Devices 64 (11) (2017) 4594–4598.

[34] S.-J. Liang, L. Ang, Electron thermionic emission from graphene and a thermionic energy converter, Physical Review Applied 3 (1) (2015) 014002.

[35] Y. Sata, R. Moriya, S. Morikawa, N. Yabuki, S. Masubuchi, T. Machida, Electric field modulation of Schottky barrier height in graphene/MoSe$_2$ van der Waals heterointerface, Applied Physics Letters 107 (2) (2015) 023109.

[36] K. Xu, C. Zeng, Q. Zhang, R. Yan, P. Ye, K. Wang, A. C. Seabaugh, H. G. Xing, J. S. Suehle, C. A. Richter, et al., Direct measurement of Dirac point energy at the graphene/oxide interface, Nano Letters 13 (1) (2012) 131–136.

[37] C. Christodoulou, A. Giannakopoulos, M. Nardi, G. Ligorio, M. Oehzelt, L. Chen, L. Pasquali, M. Timpel, A. Giglia, S. Nannarone, et al., Tuning the work function of graphene-on-quartz with a high weight molecular acceptor, The Journal of Physical Chemistry C 118 (9) (2014) 4784–4790.

[38] S.-J. Liang, B. Liu, W. Hu, K. Zhou, L. Ang, Thermionic energy conversion based on graphene van der waals heterostructures, Scientific Reports 7 (2017) 1–9.

[39] M. Neupane, S.-Y. Xu, R. Sankar, N. Alidoust, G. Bian, C. Liu, I. Belopolski, T.-R. Chang, H.-T. Jeng, H. Lin, et al., Observation of a three-dimensional topological Dirac semimetal phase in high-mobility Cd_3As_2, Nature Communications 5 (2014) 3786.

[40] T. Liang, Q. Gibson, M. N. Ali, M. Liu, R. Cava, N. Ong, Ultrahigh mobility and giant magnetoresistance in the Dirac semimetal Cd_3As_2, Nature Materials 14 (3) (2015) 280–284.

[41] C. Zhu, F. Wang, Y. Meng, X. Yuan, F. Xiu, H. Luo, Y. Wang, J. Li, X. Lv, L. He, et al., A robust and tuneable mid-infrared optical switch enabled by bulk Dirac fermions, Nature Communications 8 (2017) 14111.

[42] C. Zhang, T. Zhou, S. Liang, J. Cao, X. Yuan, Y. Liu, Y. Shen, Q. Wang, J. Zhao, Z. Yang, et al., Unexpected low thermal conductivity and large power factor in Dirac semimetal Cd_3As_2, Chinese Physics B 25 (1) (2015) 017202.

[43] H. Liu, X. Shi, F. Xu, L. Zhang, W. Zhang, L. Chen, Q. Li, C. Uher, T. Day, G. J. Snyder, Copper ion liquid-like thermoelectrics, Nature Materials 11 (5) (2012) 422.

[44] G. J. Snyder, M. Christensen, E. Nishibori, T. Caillat, B. B. Iversen, Disordered zinc in Zn_4Sb_3 with phonon-glass and electron-crystal thermoelectric properties, Nature Materials 3 (7) (2004) 458.

[45] B. Poudel, Q. Hao, Y. Ma, Y. Lan, A. Minnich, B. Yu, X. Yan, D. Wang, A. Muto, D. Vashaee, et al., High-thermoelectric performance of nanostructured bismuth antimony telluride bulk alloys, Science 320 (5876) (2008) 634–638.

[46] G. Slack, Crc handbook of thermoelectrics, in CRC Handbook of Thermoelectrics (Ed: Rowe, EM) 80 (18) (1995) 4016.

[47] X. Shi, J. Yang, J. R. Salvador, M. Chi, J. Y. Cho, H. Wang, S. Bai, J. Yang, W. Zhang, L. Chen, Multiple-filled skutterudites: High thermoelectric figure of merit through separately optimizing electrical and thermal transports, Journal of the American Chemical Society 133 (20) (2011) 7837–7846.

[48] G. J. Snyder, E. S. Toberer, Complex thermoelectric materials, Nature Materials 7 (2) (2008) 105–114.

[49] K. F. Hsu, S. Loo, F. Guo, W. Chen, J. S. Dyck, C. Uher, T. Hogan, E. Polychroniadis, M. G. Kanatzidis, Cubic $\mathrm{AgPb}_m\mathrm{SbTe}_{2+m}$: Bulk thermoelectric materials with high figure of merit, Science 303 (5659) (2004) 818–821.

[50] M. Zhou, J.-F. Li, T. Kita, Nanostructured $\mathrm{AgPb}_m\mathrm{SbTe}_{m+2}$ system bulk materials with enhanced thermoelectric performance, Journal of the American Chemical Society 130 (13) (2008) 4527–4532.

[51] K. Biswas, J. He, I. D. Blum, C.-I. Wu, T. P. Hogan, D. N. Seidman, V. P. Dravid, M. G. Kanatzidis, High-performance bulk thermoelectrics with all-scale hierarchical architectures, Nature 489 (7416) (2012) 414.

[52] W. Xie, J. He, H. J. Kang, X. Tang, S. Zhu, M. Laver, S. Wang, J. R. Copley, C. M. Brown, Q. Zhang, et al., Identifying the specific nanostructures responsible for the high thermoelectric performance of $\mathrm{(Bi, Sb)_2Te_3}$ nanocomposites, Nano Letters 10 (9) (2010) 3283–3289.

[53] Y. Pei, X. Shi, A. LaLonde, H. Wang, L. Chen, G. J. Snyder, Convergence of electronic bands for high performance bulk thermoelectrics, Nature 473 (7345) (2011) 66.

[54] Y. Pei, A. D. LaLonde, N. A. Heinz, X. Shi, S. Iwanaga, H. Wang, L. Chen, G. J. Snyder, Stabilizing the optimal carrier concentration for high thermoelectric efficiency, Advanced Materials 23 (47) (2011) 5674–5678.

[55] H. Wang, Y. Pei, A. D. LaLonde, G. J. Snyder, Heavily doped p-type pbse with high thermoelectric performance: An alternative for PbTe, Advanced Materials 23 (11) (2011) 1366–1370.

[56] W. Liu, X. Tan, K. Yin, H. Liu, X. Tang, J. Shi, Q. Zhang, C. Uher, Convergence of conduction bands as a means of enhancing thermoelectric performance of n-type $\mathrm{Mg_2Si}_{1-x}\mathrm{Sn}_x$ solid solutions, Physical Review Letters 108 (16) (2012) 166601.

[57] H. Wang, Y. Pei, A. D. LaLonde, G. J. Snyder, Weak electron–phonon coupling contributing to high thermoelectric performance in n-type PbSe, Proceedings of the National Academy of Sciences 109 (25) (2012) 9705–9709.

[58] C. Wood, Materials for thermoelectric energy conversion, Rep. Prog. Phys 51 (1988) 459–539.

[59] A. K. Geim, K. S. Novoselov, The rise of graphene, Nature Materials 6 (3) (2007) 183–191.

[60] Z. Wang, H. Weng, Q. Wu, X. Dai, Z. Fang, Three-dimensional Dirac semimetal and quantum transport in Cd_3As_2, Physical Review B 88 (12) (2013) 125427.

[61] J.-H. Chen, C. Jang, S. Xiao, M. Ishigami, M. S. Fuhrer, Intrinsic and extrinsic performance limits of graphene devices on SiO_2, Nature Nanotechnology 3 (4) (2008) 206–209.

[62] Y. S. Ang, Q. Chen, C. Zhang, Nonlinear optical response of graphene in terahertz and near-infrared frequency regime, Frontiers of Optoelectronics 8 (1) (2015) 3–26.

[63] A. K. Geim, K. S. Novoselov, The rise of graphene, in: Nanoscience and Technology: A Collection of Reviews from Nature Journals, World Scientific, 2010, pp. 11–19.

[64] V. Gusynin, S. Sharapov, J. Carbotte, On the universal ac optical background in graphene, New Journal of Physics 11 (9) (2009) 095013.

[65] K. I. Bolotin, K. Sikes, Z. Jiang, M. Klima, G. Fudenberg, J. Hone, P. Kim, H. Stormer, Ultrahigh electron mobility in suspended graphene, Solid State Communications 146 (9-10) (2008) 351–355.

[66] B. Lv, H. Weng, B. Fu, X. Wang, H. Miao, J. Ma, P. Richard, X. Huang, L. Zhao, G. Chen, et al., Experimental discovery of Weyl semimetal TaAs, Physical Review X 5 (3) (2015) 031013.

[67] A. Burkov, L. Balents, Weyl semimetal in a topological insulator multilayer, Physical Review Letters 107 (12) (2011) 127205.

[68] S. Huang, M. Sanderson, J. Tian, Q. Chen, F. Wang, C. Zhang, Hot carrier relaxation in three dimensional gapped Dirac semi-metals, Journal of Physics D: Applied Physics 51 (1) (2017) 015101.

[69] C. Zhu, F. Wang, Y. Meng, X. Yuan, F. Xiu, H. Luo, Y. Wang, J. Li, X. Lv, L. He, et al., A robust and tuneable mid-infrared optical switch enabled by bulk Dirac fermions, Nature Communications 8.

[70] R. Lundgren, G. A. Fiete, Electronic cooling in Weyl and Dirac semimetals, Physical Review B 92 (12) (2015) 125139.

[71] S. Huang, M. H. Tran, J. Zuber, Q. Wang, Y. Zhu, C. Zhang, Strong tunable photomixing in semi-Dirac materials in the terahertz regime, JOSA B 36 (2) (2019) 200–203.

[72] J. Viljas, T. Heikkilä, Electron-phonon heat transfer in monolayer and bilayer graphene, Physical Review B 81 (24) (2010) 245404.

[73] M. Sanderson, S. Huang, Q. Bao, C. Zhang, Optical conductivity of a commensurate graphene-topological insulator heterostructure, Journal of Physics D: Applied Physics 50 (38) (2017) 385301.

[74] Z. Wang, Y. Sun, X.-Q. Chen, C. Franchini, G. Xu, H. Weng, X. Dai, Z. Fang, Dirac semimetal and topological phase transitions in A_3Bi (A= Na, K, Rb), Physical Review B 85 (19) (2012) 195320.

[75] A. Zyuzin, S. Wu, A. Burkov, Weyl semimetal with broken time reversal and inversion symmetries, Physical Review B 85 (16) (2012) 165110.

[76] A. Burkov, M. Hook, L. Balents, Topological nodal semimetals, Physical Review B 84 (23) (2011) 235126.

[77] X. Zhang, Z.-M. Yu, X.-L. Sheng, H. Y. Yang, S. A. Yang, Coexistence of four-band nodal rings and triply degenerate nodal points in centrosymmetric metal diborides, Physical Review B 95 (23) (2017) 235116.

[78] J. Hu, Z. Tang, J. Liu, X. Liu, Y. Zhu, D. Graf, K. Myhro, S. Tran, C. N. Lau, J. Wei, et al., Evidence of topological nodal-line fermions in ZrSiSe and ZrSiTe, Physical Review Letters 117 (1) (2016) 016602.

[79] Y. Kim, B. J. Wieder, C. Kane, A. M. Rappe, Dirac line nodes in inversion-symmetric crystals, Physical Review Letters 115 (3) (2015) 036806.

[80] J. Liu, D. Kriegner, L. Horak, D. Puggioni, C. R. Serrao, R. Chen, D. Yi, C. Frontera, V. Holy, A. Vishwanath, et al., Strain-induced nonsymmorphic symmetry breaking and removal of Dirac semimetallic nodal line in an orthoperovskite iridate, Physical Review B 93 (8) (2016) 085118.

[81] S.-Y. Yang, H. Yang, E. Derunova, S. S. Parkin, B. Yan, M. N. Ali, Symmetry demanded topological nodal-line materials, Advances in Physics: X 3 (1) (2018) 1414631.

[82] L. M. Schoop, M. N. Ali, C. Straßer, A. Topp, A. Varykhalov, D. Marchenko, V. Duppel, S. S. Parkin, B. V. Lotsch, C. R. Ast, Dirac cone protected by non-symmorphic symmetry and three-dimensional Dirac line node in ZrSiS, Nature Communications 7 (2016) 11696.

[83] W. Duan, C. Yang, Z. Ma, Y. Zhu, C. Zhang, Accurate magneto-optical determination of radius of topological nodal-ring semimetals, Physical Review B 99 (4) (2019) 045124.

[84] M. Koshino, I. F. Hizbullah, Magnetic susceptibility in three-dimensional nodal semimetals, Physical Review B 93 (4) (2016) 045201.

[85] J.-W. Rhim, Y. B. Kim, Landau level quantization and almost flat modes in three-dimensional semimetals with nodal ring spectra, Physical Review B 92 (4) (2015) 045126.

[86] H. Jiang, L. Li, J. Gong, S. Chen, Characterization of Lifshitz transitions in topological nodal line semimetals, The European Physical Journal B 91 (5) (2018) 75.

[87] A. Burkov, Quantum anomalies in nodal line semimetals, Physical Review B 97 (16) (2018) 165104.

[88] Y. Sun, Y. Zhang, C.-X. Liu, C. Felser, B. Yan, Dirac nodal lines and induced spin Hall effect in metallic rutile oxides, Physical Review B 95 (23) (2017) 235104.

[89] J. Liu, L. Balents, Correlation effects and quantum oscillations in topological nodal-loop semimetals, Physical Review B 95 (7) (2017) 075426.

[90] S. T. Ramamurthy, T. L. Hughes, Quasitopological electromagnetic response of line-node semimetals, Physical Review B 95 (7) (2017) 075138.

[91] S. Mukherjee, J. Carbotte, Transport and optics at the node in a nodal loop semimetal, Physical Review B 95 (21) (2017) 214203.

[92] S. Huang, M. Sanderson, Y. Zhang, C. Zhang, High efficiency and non-Richardson thermionics in three dimensional Dirac materials, Applied Physics Letters 111 (18) (2017) 183902.

[93] R. Rhyner, M. Luisier, Minimizing self-heating and heat dissipation in ultrascaled nanowire transistors, Nano Letters 16 (2) (2016) 1022–1026.

[94] S. V. Garimella, Y. K. Joshi, A. Bar-Cohen, R. Mahajan, K. Toh, V. Carey, M. Baelmans, J. Lohan, B. Sammakia, F. Andros, Thermal challenges in next generation electronic systems-summary of panel presentations and discussions, IEEE Transactions on Components and Packaging Technologies 25 (4) (2002) 569–575.

[95] M. F. O'Dwyer, R. A. Lewis, C. Zhang, Thermionic refrigerators with non-Richardson current, Journal of Physics D: Applied Physics 40 (4) (2007) 1167.

[96] C. Huang, Y. Pan, Y. Wang, G. Su, J. Chen, An efficient hybrid system using a thermionic generator to harvest waste heat from a reforming molten carbonate fuel cell, Energy Conversion and Management 121 (2016) 186–193.

[97] T. Shinozaki, S. Hagiwara, N. Morioka, Y. Kimura, K. Watanabe, Real-time first-principles simulations of thermionic emission from n-doped diamond surfaces, Applied Physics Express 11 (6) (2018) 064301.

[98] J. Domenech-Garret, S. Tierno, L. Conde, Enhanced thermionic currents by non equilibrium electron populations of metals, The European Physical Journal B 86 (9) (2013) 382.

[99] F. A. Koeck, R. J. Nemanich, A. Lazea, K. Haenen, Thermionic electron emission from low work-function phosphorus doped diamond films, Diamond and Related Materials 18 (5) (2009) 789–791.

[100] J. Ryan Smith, Increasing the efficiency of a thermionic engine using a negative electron affinity collector, Journal of Applied Physics 114 (16) (2013) 164514.

[101] C. L. Kane, E. J. Mele, Quantum spin hall effect in graphene, Physical Review Letters 95 (22) (2005) 226801.

[102] S. Borisenko, Q. Gibson, D. Evtushinsky, V. Zabolotnyy, B. Büchner, R. J. Cava, Experimental realization of a three-dimensional Dirac semimetal, Physical Review Letters 113 (2) (2014) 027603.

[103] S. S. Kubakaddi, T. Biswas, Hot electron cooling in Dirac semimetal Cd_3As_2 due to polar optical phonons, Journal of Physics: Condensed Matter 30 (26) (2018) 265303.

[104] L. He, X. Hong, J. Dong, J. Pan, Z. Zhang, J. Zhang, S. Li, Quantum transport evidence for the three-dimensional Dirac semimetal phase in Cd_3As_2, Physical Review Letters 113 (24) (2014) 246402.

[105] Q. Wang, C.-Z. Li, S. Ge, J.-G. Li, W. Lu, J. Lai, X. Liu, J. Ma, D.-P. Yu, Z.-M. Liao, et al., Ultrafast broadband photodetectors based on three-dimensional Dirac semimetal Cd_3As_2, Nano Letters 17 (2) (2017) 834–841.

[106] I. Crassee, R. Sankar, W.-L. Lee, A. Akrap, M. Orlita, 3d Dirac semimetal Cd_3As_2: A review of material properties, Physical Review Materials 2 (12) (2018) 120302.

[107] R. Y. Belbachir, Z. An, T. Ono, Thermal investigation of a micro-gap thermionic power generator, Journal of Micromechanics and Microengineering 24 (8) (2014) 085009.

[108] K. A. A. Khalid, T. J. Leong, K. Mohamed, Review on thermionic energy converters, IEEE Transactions on Electron Devices 63 (6) (2016) 2231–2241.

[109] D. M. Trucchi, A. Bellucci, M. Girolami, P. Calvani, E. Cappelli, S. Orlando, R. Polini, L. Silvestroni, D. Sciti, A. Kribus, Solar thermionic-thermoelectric generator (ST_2G): Concept, materials engineering, and prototype demonstration, Advanced Energy Materials 8 (32) (2018) 1802310.

[110] B. Lough, S. Lee, R. Lewis, C. Zhang, Numerical calculation of thermionic cooling efficiency in a double-barrier semiconductor heterostructure, Physica E: Low-dimensional Systems and Nanostructures 11 (2-3) (2001) 287–291.

[111] M. Bescond, D. Logoteta, F. Michelini, N. Cavassilas, T. Yan, A. Yangui, M. Lannoo, K. Hirakawa, Thermionic cooling devices based on resonant-tunneling AlGaAs/GaAs heterostructure, Journal of Physics: Condensed Matter 30 (6) (2018) 064005.

[112] F. Jin, S. Little, Thermionic cooling with functionalized carbon nanotube thin films, Applied Physics Letters 106 (11) (2015) 113102.

[113] Z. Wang, S.-C. Zhang, Chiral anomaly, charge density waves, and axion strings from Weyl semimetals, Physical Review B 87 (16) (2013) 161107.

[114] H. Wei, S.-P. Chao, V. Aji, Excitonic phases from Weyl semimetals, Physical Review Letters 109 (19) (2012) 196403.

[115] K.-Y. Yang, Y.-M. Lu, Y. Ran, Quantum Hall effects in a Weyl semimetal: Possible application in pyrochlore iridates, Physical Review B 84 (7) (2011) 075129.

[116] R. Bistritzer, A. MacDonald, Electronic cooling in graphene, Physical Review Letters 102 (20) (2009) 206410.

[117] C. Weber, E. Arushanov, B. S. Berggren, T. Hosseini, N. Kouklin, A. Nateprov, Transient reflectance of photoexcited Cd_3As_2, Applied Physics Letters 106 (23) (2015) 231904.

[118] J. Maultzsch, S. Reich, C. Thomsen, H. Requardt, P. Ordejón, Phonon dispersion in graphite, Physical Review Letters 92 (7) (2004) 075501.

[119] B. Ferguson, X.-C. Zhang, Materials for terahertz science and technology, Nature Materials 1 (1) (2002) 26–33.

[120] R. A. Lewis, Physical phenomena in electronic materials in the terahertz region, Proceedings of the IEEE 95 (8) (2007) 1641–1645.

[121] S. Liu, P. Zhang, W. Liu, S. Gong, R. Zhong, Y. Zhang, M. Hu, Surface polariton cherenkov light radiation source, Physical Review Letters 109 (15) (2012) 153902.

[122] C. Yang, A. Wright, F. Gao, C. Zhang, Z. Zeng, W. Xu, Two color plasmon excitation in an electron-hole bilayer structure controlled by the spin-orbit interaction, Applied Physics Letters 88 (22) (2006) 223102.

[123] L. Ju, B. Geng, J. Horng, C. Girit, M. Martin, Z. Hao, H. A. Bechtel, X. Liang, A. Zettl, Y. R. Shen, et al., Graphene plasmonics for tunable terahertz metamaterials, Nature Nanotechnology 6 (10) (2011) 630–634.

[124] S. Chen, W. Shi, L. Hou, R. A. Lewis, Investigation of terahertz peak frequencies from GaAs photoconductive antennas, IEEE Journal of Selected Topics in Quantum Electronics 23 (4) (2017) 1–6.

[125] R. Köhler, A. Tredicucci, F. Beltram, H. E. Beere, E. H. Linfield, A. G. Davies, D. A. Ritchie, R. C. Iotti, F. Rossi, Terahertz semiconductor-heterostructure laser, Nature 417 (6885) (2002) 156–159.

[126] S. Mikhailov, Non-linear electromagnetic response of graphene, EPL (Europhysics Letters) 79 (2) (2007) 27002.

[127] C. Liu, Y. Zheng, Z. Zeng, R. Li, Driving-laser ellipticity dependence of high-order harmonic generation in graphene, Physical Review A 97 (6) (2018) 063412.

[128] F. Karimi, A. Davoody, I. Knezevic, Nonlinear optical response in graphene nanoribbons: The critical role of electron scattering, Physical Review B 97 (24) (2018) 245403.

[129] P. Navaeipour, I. Al-Naib, M. M. Dignam, Third-harmonic terahertz generation from graphene in a parallel-plate waveguide, Physical Review A 97 (1) (2018) 013847.

[130] V. Pardo, W. E. Pickett, Half-metallic semi-Dirac-point generated by quantum confinement in TiO_2/VO_2 nanostructures, Physical Review Letters 102 (16) (2009) 166803.

[131] G. Montambaux, F. Piéchon, J.-N. Fuchs, M. O. Goerbig, Merging of Dirac points in a two-dimensional crystal, Physical Review B 80 (15) (2009) 153412.

[132] G. Montambaux, F. Piéchon, J.-N. Fuchs, M. Goerbig, A universal Hamiltonian for motion and merging of Dirac points in a two-dimensional crystal, The European Physical Journal B 72 (4) (2009) 509.

[133] V. Pardo, W. E. Pickett, Metal-insulator transition through a semi-Dirac point in oxide nanostructures: VO_2 (001) layers confined within TiO_2, Physical Review B 81 (3) (2010) 035111.

[134] G. E. Volovik, Topological invariants for Standard Model: From semi-metal to topological insulator, JETP Letters 91 (2) (2010) 55–61.

[135] S. Banerjee, W. E. Pickett, Phenomenology of a semi-Dirac semi-Weyl semimetal, Physical Review B 86 (7) (2012) 075124.

[136] P. Pyatkovskiy, T. Chakraborty, Dynamical polarization and plasmons in a two-dimensional system with merging Dirac points, Physical Review B 93 (8) (2016) 085145.

[137] M. Sanderson, S. Huang, Y. Zhang, C. Zhang, Frequency and orientation dependent conductivity of a semi-Dirac system, Journal of Physics D: Applied Physics 51 (20) (2018) 205302.

[138] S. Banerjee, R. Singh, V. Pardo, W. Pickett, Tight-binding modeling and low-energy behavior of the semi-Dirac point, Physical Review Letters 103 (1) (2009) 016402.

Appendix

A.1 Velocity expansion

(a) velocity expansion in the x direction

$$v_x = \frac{\partial \epsilon}{\partial P_x} = \frac{P_x^3}{mH}, \tag{7.1}$$

$$H = \sqrt{P_x^4 + 2m\epsilon_0 P_y^2}, \tag{7.2}$$

$$P_x = p_x + u_x, P_y = p_y + u_y, \tag{7.3}$$

$$F = \sqrt{p_x^4 + 2m\epsilon_0 p_y^2}, \tag{7.4}$$

$$\frac{\partial F}{\partial p_x} = \frac{2p_x^3}{F}, \tag{7.5}$$

$$\frac{\partial F}{\partial p_y} = \frac{2m\epsilon_0 p_y}{F}. \tag{7.6}$$

Firstly, we calculate the total differential of v_x up to the third-order

$$G_x^{(1)} = \frac{\partial v_x}{\partial p_x}u_x + \frac{\partial v_x}{\partial p_y}u_y = (\frac{3p_x^2}{mF} - \frac{2p_x^6}{mF^3})u_x - \frac{2\epsilon_0 p_x^3 p_y}{F^3}u_y, \tag{7.7}$$

$$\begin{aligned} G_x^{(2)} = \frac{\partial G_x^1}{\partial p_x}u_x + \frac{\partial G_x^1}{\partial p_y}u_y &= (\frac{6p_x}{mF} - \frac{18p_x^5}{mF^3} + \frac{12p_x^9}{mF^5})u_x^2 \\ &- (\frac{12\epsilon_0 p_x^2 p_y}{F^3} - \frac{24\epsilon_0 p_x^6 p_y}{F^5})u_x u_y - (\frac{2\epsilon_0 p_x^3}{F^3} - \frac{12m\epsilon_0^2 p_x^3 p_y^2}{F^5})u_y^2 \\ &= I_1 u_x^2 - I_2 u_x u_y - I_3 u_y^2, \end{aligned} \tag{7.8}$$

$$\begin{aligned} G_x^{(3)} = (&\frac{\partial I_1}{\partial p_x}u_x^3 - \frac{\partial I_2}{\partial p_x}u_x^2 u_y - \frac{\partial I_3}{\partial p_x}u_x u_y^2 \\ &+ \frac{\partial I_1}{\partial p_y}u_x^2 u_y - \frac{\partial I_2}{\partial p_y}u_x u_y^2 - \frac{\partial I_3}{\partial p_y}u_y^3), \end{aligned} \tag{7.9}$$

$$\begin{aligned} \frac{\partial I_1}{\partial p_x} &= (\frac{6}{mF} - \frac{6p_x}{mF^2}\frac{2p_x^3}{F} - 90\frac{p_x^4}{mF^3} \\ &+ 3\frac{18p_x^5}{mF^4}\frac{2p_x^3}{F} + \frac{108p_x^8}{mF^5} - 5\frac{12p_x^9}{mF^6}\frac{2p_x^3}{F} \\ &= \frac{6}{mF} - \frac{102p_x^4}{mF^3} + \frac{216p_x^8}{mF^5} - \frac{120p_x^{12}}{mF^7}, \end{aligned} \tag{7.10}$$

$$\begin{aligned}\frac{\partial I_1}{\partial p_y} &= -\frac{6p_x}{mF^2}\frac{2m\epsilon_0 p_y}{F} + 3\frac{18p_x^5}{mF^4}\frac{2m\epsilon_0 p_y}{F} - 5\frac{12p_x^9}{mF^6}\frac{2m\epsilon_0 p_y}{F} \\ &= -\frac{12\epsilon_0 p_x p_y}{F^3} + \frac{108\epsilon_0 p_x^5 p_y}{F^5} - \frac{120\epsilon_0 p_x^9 p_y}{F^7},\end{aligned} \tag{7.11}$$

$$\begin{aligned}\frac{\partial I_2}{\partial p_x} &= \frac{24\epsilon_0 p_x p_y}{F^3} - 3\frac{12\epsilon_0 p_x^2 p_y}{F^4} \times \frac{2p_x^3}{F} - \frac{24\epsilon_0 6p_x^5 p_y}{F^5} \\ &\quad + 5\frac{24\epsilon_0 p_x^6 p_y}{F^6} \times \frac{2p_x^3}{F} \\ &= \frac{24\epsilon_0 p_x p_y}{F^3} - \frac{216\epsilon_0 p_x^5 p_y}{F^5} + \frac{240\epsilon_0 p_x^9 p_y}{F^7},\end{aligned} \tag{7.12}$$

$$\begin{aligned}\frac{\partial I_2}{\partial p_y} &= \frac{12\epsilon_0 p_x^2}{F^3} - 3\frac{12\epsilon_0 p_x^2 p_y}{F^4} \times \frac{2m\epsilon_0 p_y}{F} \\ &\quad - \frac{24\epsilon_0 p_x^6}{F^5} + 5\frac{24\epsilon_0 p_x^6 p_y}{F^6} \times \frac{2m\epsilon_0 p_y}{F} \\ &= \frac{12\epsilon_0 p_x^2}{F^3} - \frac{72m\epsilon_0^2 p_x^2 p_y^2}{F^5} - \frac{24\epsilon_0 p_x^6}{F^5} + \frac{240m\epsilon_0^2 p_x^6 p_y^2}{F^7},\end{aligned} \tag{7.13}$$

$$\frac{\partial I_3}{\partial p_x} \quad = \tfrac{6\epsilon_0 p_x^2}{F^3} - \tfrac{12\epsilon_0 p_x^6}{F^5} - \tfrac{36m\epsilon_0^2 p_x^2 p_y^2}{F^5} + \tfrac{120m\epsilon_0^2 p_x^6 p_y^2}{F^6}, \tag{7.14}$$

$$\frac{\partial I_3}{\partial p_y} = -\frac{36m\epsilon_0^2 p_x^3 p_y}{F^5} + \frac{120m^2\epsilon_0^3 p_x^3 p_y^3}{F^7}. \tag{7.15}$$

Now the first- and the third-order velocity in the x direction are obtained by

$$v_x^{(1)} = G_x^{(1)} = (\frac{3p_x^2}{mF} - \frac{2p_x^6}{mF^3})u_x - \frac{2\epsilon_0 p_x^3 p_y}{F^3}u_y, \tag{7.16}$$

$$\begin{aligned}v_x^{(3)} &= \frac{1}{6}G_x^{(3)} = (\frac{1}{mF} - \frac{17p_x^4}{mF^3} + \frac{36p_x^8}{mF^5} - \frac{20p_x^{12}}{mF^7})u_x^3 \\ &\quad - (\frac{6\epsilon_0 p_x p_y}{F^3} - \frac{54\epsilon_0 p_x^5 p_y}{F^5} + \frac{60\epsilon_0 p_x^9 p_y}{F^7})u_x^2 u_y \\ &\quad - (\frac{3\epsilon_0 p_x^2}{F^3} - \frac{18m\epsilon_0^2 p_x^2 p_y^2}{F^5} - \frac{6\epsilon_0 p_x^6}{F^5} + \frac{60m\epsilon_0^2 p_x^6 p_y^2}{F^7})u_x u_y^2 \\ &\quad + (\frac{6m\epsilon_0^2 p_x^3 p_y}{F^5} - \frac{20m^2\epsilon_0^3 p_x^3 p_y^3}{F^7})u_y^3.\end{aligned} \tag{7.17}$$

(b) velocity expansion in the y direction

$$v_y = \frac{\partial \epsilon}{\partial P_y} = \frac{P_y}{H}. \tag{7.18}$$

Similarly, we calculate the total differential of v_y up to the third-order

$$\begin{aligned}G_y^{(1)} &= -\frac{p_y\epsilon_0}{F^2}\frac{2p_x^3}{F}u_x + (\frac{\epsilon_0}{F} - \frac{p_y\epsilon_0}{F^2}\frac{2m\epsilon_0 p_y}{F})u_y \\ &= -\frac{2\epsilon_0 p_x^3 p_y}{F^3}u_x + (\frac{\epsilon_0}{F} - \frac{2m\epsilon_0^2 p_y^2}{F^3})u_y,\end{aligned} \tag{7.19}$$

$$\begin{aligned}G_y^{(2)} &= (-\frac{6\epsilon_0 p_x^2 p_y}{F^3} + \frac{6\epsilon_0 p_x^3 p_y}{F^4}\frac{2p_x^3}{F})u_x^2 - (\frac{\epsilon_0}{F^2}\frac{2p_x^3}{F} - \frac{6m\epsilon_0^2 p_y^2}{F^4}\frac{2p_x^3}{F} \\ &+ \frac{2\epsilon_0 p_x^3}{F^3} - \frac{6\epsilon_0 p_x^3 p_y}{F^4}\frac{2m\epsilon_0 p_y}{F})u_x u_y \\ &- (\frac{\epsilon_0}{F^2}\frac{2m\epsilon_0 p_y}{F} + \frac{4m\epsilon_0^2 p_y}{F^3} - \frac{6m\epsilon_0^2 p_y^2}{F^4}\frac{2m\epsilon_0 p_y}{F})u_y^2 \\ &= (-\frac{6\epsilon_0 p_x^2 p_y}{F^3} + \frac{12\epsilon_0 p_x^6 p_y}{F^5})u_x^2 \\ &- (\frac{4\epsilon_0 p_x^3}{F^3} - \frac{24m\epsilon_0^2 p_x^3 p_y^2}{F^5})u_x u_y - (\frac{6m\epsilon_0^2 p_y}{F^3} - \frac{12m^2\epsilon_0^3 p_y^3}{F^5})u_y^2 \\ &= I_1 u_x^2 - I_2 u_x u_y - I_3 u_y^2,\end{aligned} \tag{7.20}$$

$$\begin{aligned}\frac{\partial I_1}{\partial p_x} &= -\frac{12\epsilon_0 p_x p_y}{F^3} + \frac{18\epsilon_0 p_x^2 p_y}{F^4}\frac{2p_x^3}{F} + \frac{72\epsilon_0 p_x^5 p_y}{F^5} - \frac{60\epsilon_0 p_x^6 p_y}{F^6}\frac{2p_x^3}{F} \\ &= -\frac{12\epsilon_0 p_x p_y}{F^3} + \frac{108\epsilon_0 p_x^5 p_y}{F^5} - \frac{120\epsilon_0 p_x^9 p_y}{F^7},\end{aligned} \tag{7.21}$$

$$\begin{aligned}\frac{\partial I_1}{\partial p_y} &= -\frac{6\epsilon_0 p_x^2}{F^3} + \frac{18\epsilon_0 p_x^2 p_y}{F^4}\frac{2m\epsilon_0 p_y}{F} + \frac{12\epsilon_0 p_x^6}{F^5} - \frac{60\epsilon_0 p_x^6 p_y}{F^6}\frac{2m\epsilon_0 p_y}{F} \\ &= -\frac{6\epsilon_0 p_x^2}{F^3} + \frac{36m\epsilon_0^2 p_x^2 p_y^2}{F^5} + \frac{12\epsilon_0 p_x^6}{F^5} - \frac{120m\epsilon_0^2 p_x^6 p_y^2}{F^7},\end{aligned} \tag{7.22}$$

$$\begin{aligned}\frac{\partial I_2}{\partial p_x} &= \frac{12\epsilon_0 p_x^2}{F^3} - \frac{12\epsilon_0 p_x^3}{F^4}\frac{2p_x^3}{F} - \frac{72m\epsilon_0^2 p_x^2 p_y^2}{F^5} + \frac{240m\epsilon_0^2 p_x^3 p_y^2}{F^6}\frac{2p_x^3}{F} \\ &= \frac{12\epsilon_0 p_x^2}{F^3} - \frac{24\epsilon_0 p_x^6}{F^5} - \frac{72m\epsilon_0^2 p_x^2 p_y^2}{F^5} + \frac{240m\epsilon_0^2 p_x^6 p_y^2}{F^7},\end{aligned} \tag{7.23}$$

$$\begin{aligned}\frac{\partial I_2}{\partial p_y} &= -\frac{12\epsilon_0 p_x^3}{F^4}\frac{2m\epsilon_0 p_y}{F} - \frac{48m\epsilon_0^2 p_x^3 p_y}{F^5} + \frac{240m\epsilon_0^2 p_x^3 p_y^2}{F^6}\frac{2m\epsilon_0 p_y}{F} \\ &= -\frac{72m\epsilon_0^2 p_x^3 p_y}{F^5} + \frac{240m^2\epsilon_0^3 p_x^3 p_y^3}{F^7},\end{aligned} \tag{7.24}$$

$$\frac{\partial I_3}{\partial p_x} = -\tfrac{36m\epsilon_0^2 p_x^3 p_y}{F^5} + \tfrac{120m^2\epsilon_0^3 p_x^3 p_y^3}{F^7}, \tag{7.25}$$

$$\begin{aligned}\frac{\partial I_3}{\partial p_y} &= \frac{6m\epsilon_0 62}{F^3} - \frac{18m\epsilon_0^2 p_y}{F64}\frac{2m\epsilon_0 p_y}{F} - \frac{36m^2\epsilon - 0^3 p_y 62}{F65}\frac{2m\epsilon_0 p_y}{F} \\ &= \frac{6m\epsilon_0^2}{F^3} - \frac{72m^2\epsilon_0^3 p_y^2}{F^5} + \frac{120m^3\epsilon_0^4 p_y^4}{F^7}.\end{aligned} \tag{7.26}$$

The first- and the third-order velocity in the y direction are obtained by

$$\begin{aligned}v_y^{(1)} &= -\frac{p_y\epsilon_0}{F^2}\frac{2p_x^3}{F}u_x + (\frac{\epsilon_0}{F} - \frac{p_y\epsilon_0}{F^2}\frac{2m\epsilon_0 p_y}{F})u_y \\ &= -\frac{2\epsilon_0 p_x^3 p_y}{F^3}u_x + (\frac{\epsilon_0}{F} - \frac{2m\epsilon_0^2 p_y^2}{F^3})u_y,\end{aligned} \tag{7.27}$$

$$\begin{aligned}v_y^{(3)} = \frac{1}{6}G_y^{(3)} &= (-\frac{2\epsilon_0 p_x p_y}{F^3} + \frac{18\epsilon_0 p_x^5 p_y}{F^5} - \frac{20\epsilon_0 p_x^9 p_y}{F^7})u_x^3 \\ &- (\frac{3\epsilon_0 p_x^2}{F^3} - \frac{18m\epsilon_0^2 p_x^2 p_y^2}{F^5} - \frac{6\epsilon_0 p_x^6}{F^5} + \frac{60m\epsilon_0^2 p_x^6 p_y^2}{F^7})u_x^2 u_y \\ &+ (\frac{18m\epsilon_0^2 p_x^3 p_y}{F^5} - \frac{60m^2\epsilon_0^3 p_x^3 p_y^3}{F^7})u_x u_y^2 \\ &- (\frac{m\epsilon_0^2}{F^3} - \frac{12m^2\epsilon_0^3 p_y^2}{F^5} + \frac{20m^3\epsilon_0^4 p_y^4}{F^7})u_y^3.\end{aligned} \tag{7.28}$$

A.2 Density of states for Nodal-ring semimetals

The energy momentum dispersion of nodal-ring is given by

$$\epsilon = \pm\sqrt{k_x^2 + (\sqrt{k_y^2 + k_z^2} \pm b)^2}. \tag{7.29}$$

At the beginning, we only discuss the branch that forms nodal ring *i.e.*,

$$\epsilon = \sqrt{k_x^2 + (\sqrt{k_y^2 + k_z^2} - b)^2}. \tag{7.30}$$

In a spherical coordinate system, k_x, k_y and k_z can be written as

$$\begin{aligned} k_y &= k\sin(\theta)\cos(\phi), \\ k_z &= k\sin(\theta)\sin(\phi), \\ k_x &= k\cos(\theta). \end{aligned} \tag{7.31}$$

Plugging them into Eq. 7.30, we get

$$\epsilon = \sqrt{k^2 + b^2 - 2kb\sin(\theta)}. \tag{7.32}$$

$$\begin{aligned} \epsilon^2 &= k^2 + b^2 - 2kb\sin(\theta) = (k - b\sin(\theta))^2 + b^2 - b^2\sin^2(\theta) \\ &= (k - b\sin(\theta))^2 + b^2\cos^2(\theta). \end{aligned} \tag{7.33}$$

Therefore, k can be written as

$$k_\pm = b\sin(\theta) \pm \sqrt{\epsilon^2 - b^2\cos^2(\theta)}. \tag{7.34}$$

In spherical coordinates, k is always a non-negative real number, which requires

$$\epsilon^2 - b^2\cos^2(\theta) > 0. \tag{7.35}$$

In this sense, $|\cos\theta| < \epsilon/b$ can make sure $k = b\sin(\theta) + \sqrt{\epsilon^2 - b^2\cos^2(\theta)}$ is meaningful. To make sure $k_2 = b\sin(\theta) - \sqrt{\epsilon^2 - b^2\cos^2(\theta)}$ is meaningful, it further requires,

$$b\sin(\theta) - \sqrt{\epsilon^2 - b^2\cos^2(\theta)} > 0. \tag{7.36}$$

This results $\epsilon < b$. Overall, for $\epsilon < b$ and $|\cos(\theta)| < \epsilon/b$,

$$k_\pm = b\sin(\theta) \pm \sqrt{\epsilon^2 - b^2\cos^2(\theta)}. \tag{7.37}$$

For $\epsilon > b$ and $|\cos(\theta)| < \epsilon/b$,

$$k = b\sin(\theta) + \sqrt{\epsilon^2 - b^2\cos^2(\theta)}. \tag{7.38}$$

Now, we are going to evaluate density of states of nodal ring system. According to its definition, density of states can be calculated by,

$$\begin{aligned} g(\epsilon) &= 2\frac{1}{(2\pi)^3}\int\int\int \delta(\epsilon - \epsilon(k_x, k_y, k_z))\mathrm{d}k_x\mathrm{d}k_y\mathrm{d}k_z \\ &= 2\frac{1}{(2\pi)^3}\int\int\int \delta(\epsilon - \sqrt{k^2 + b^2 - 2kb\sin(\theta)}) \\ &\times k^2\sin(\theta)\mathrm{d}\theta\mathrm{d}\phi\mathrm{d}k \\ &= \frac{1}{2\pi^2}\int\int \delta(\epsilon - \sqrt{k^2 + b^2 - 2kb\sin(\theta)})k^2\sin(\theta)\mathrm{d}\theta dk. \end{aligned} \tag{7.39}$$

Let $h(k) = \epsilon - \sqrt{k^2 + b^2 - 2kb\sin(\theta)} = 0$. Then,

$$|h'(k)| = \frac{|2k - 2b\sin(\theta)|}{2\sqrt{k^2 + b^2 - 2kb\sin(\theta)}} = \frac{|k - b\sin(\theta)|}{\epsilon}. \tag{7.40}$$

As we have discussed before, $h(k) = 0$ has two roots when $\epsilon < b$, and it has one root when $\epsilon > b$. When $\epsilon < b$, the density of states can be calculated by,

$$\begin{aligned} g(\epsilon) &= \frac{1}{2\pi^2}\int\int \delta(\epsilon - \sqrt{k^2 + b^2 - 2kb\sin(\theta)})k^2\sin(\theta)\mathrm{d}\theta dk \\ &= \frac{1}{2\pi^2}\int \frac{1}{|h'(k_1)|}k_1^2\sin(\theta)\mathrm{d}\theta + \frac{1}{2\pi^2}\int \frac{1}{|h'(k_2)|}k_2^2\sin(\theta)\mathrm{d}\theta \\ &= I_1 + I_2, \end{aligned} \tag{7.41}$$

where I_1 can be calculated by

$$\begin{aligned}
I_1 &= \frac{1}{2\pi^2}\int \frac{1}{|h'(k_1)|}k_1^2\sin(\theta)\mathrm{d}\theta = \frac{1}{2\pi^2}\int \frac{\epsilon}{|k_1 - b\sin(\theta)|}k_1^2\sin(\theta)\mathrm{d}\theta \\
&= \frac{1}{2\pi^2}\int \frac{\epsilon}{|b\sin(\theta) + \sqrt{\epsilon^2 - b^2\cos^2(\theta)} - b\sin(\theta)|}[b\sin(\theta) \\
&+ \sqrt{\epsilon^2 - b^2\cos^2(\theta)}]^2\sin(\theta)\mathrm{d}\theta \\
&= \frac{1}{2\pi^2}\int \frac{\epsilon}{\sqrt{\epsilon^2 - b^2\cos^2(\theta)}}[b\sin(\theta) + \sqrt{\epsilon^2 - b^2\cos^2(\theta)}]^2\sin(\theta)\mathrm{d}\theta \\
&= \frac{\epsilon}{2\pi^2}\int \frac{b^2 + \epsilon^2 - 2b^2\cos^2(\theta)}{\sqrt{\epsilon^2 - b^2\cos^2(\theta)}} + 2\frac{\sqrt{\epsilon^2 - b^2\cos^2(\theta)}b\sin(\theta)}{\sqrt{\epsilon^2 - b^2\cos^2(\theta)}}\sin(\theta)\mathrm{d}\theta \\
&= \frac{\epsilon}{2\pi^2}\int [\frac{b^2 + \epsilon^2}{\sqrt{\epsilon^2 - b^2\cos^2(\theta)}} - \frac{2b^2\cos^2(\theta)}{\sqrt{\epsilon^2 - b^2\cos^2(\theta)}} + 2b\sin(\theta)]\sin(\theta)\mathrm{d}\theta \\
&= \frac{\epsilon}{2\pi^2}\int -[\frac{b^2 + \epsilon^2}{\sqrt{\epsilon^2 - b^2\cos^2(\theta)}} - \frac{2b^2\cos^2(\theta)}{\sqrt{\epsilon^2 - b^2\cos^2(\theta)}}]\mathrm{d}\cos(\theta) \\
&+ \int \frac{\epsilon}{2\pi^2}2b\sin^2(\theta)\mathrm{d}\theta.
\end{aligned} \tag{7.42}$$

As mentioned above, $|\cos(\theta)| \leq \epsilon/b$ results in $\theta \in$ [arccos(ϵ/b), π - arccos(ϵ/b)], where arccos(-ϵ/b) = π - arccos(ϵ/b). Thus I_1 can be written as

$$\begin{aligned}
I_1 &= \frac{\epsilon}{2\pi^2}\int_{\epsilon/b}^{-\epsilon/b} -[\frac{b^2+\epsilon^2}{\sqrt{\epsilon^2-b^2x^2}} - \frac{2b^2x^2}{\sqrt{\epsilon^2-b^2x^2}}]\mathrm{d}x \\
&+ \int_{\mathrm{arccos}(\epsilon/b)}^{\pi-\mathrm{arccos}(\epsilon/b)} \frac{\epsilon}{2\pi^2}2b\mathrm{sin}^2(\theta)\mathrm{d}\theta \\
&= \frac{\epsilon}{2\pi^2}\int_{\epsilon/b}^{-\epsilon/b}[-\frac{b^2+\epsilon^2}{b\sqrt{\epsilon^2/b^2-x^2}} + \frac{2bx^2}{\sqrt{\epsilon^2/b^2-x^2}}]\mathrm{d}x \\
&+ \int_{\mathrm{arccos}(\epsilon/b)}^{\pi-\mathrm{arccos}(\epsilon/b)} \frac{\epsilon}{2\pi^2}2b\mathrm{sin}^2(\theta)\mathrm{d}\theta \\
&= \frac{\epsilon}{2\pi^2}[-\frac{b^2+\epsilon^2}{b}\mathrm{arcsin}(\frac{bx}{\epsilon}) + 2b[-\frac{1}{2}x\sqrt{\epsilon^2/b^2-x^2} \\
&+ \frac{1}{2}(\frac{\epsilon}{b})^2\mathrm{arcsin}(\frac{bx}{\epsilon})]]|_{\epsilon/b}^{-\epsilon/b} \\
&+ \frac{b\epsilon}{2\pi^2}[\theta - \mathrm{sin}(\theta)\mathrm{cos}(\theta)]|_{\mathrm{arccos}(\epsilon/b)}^{\pi-\mathrm{arccos}(\epsilon/b)} \\
&= \frac{\epsilon}{2\pi^2}[-\frac{b^2+\epsilon^2}{b}\mathrm{arcsin}(-1)\times 2 + 2b[0+\frac{1}{2}(\frac{\epsilon}{b})^2\mathrm{arcsin}(-1)]\times 2] \\
&+ \frac{b\epsilon}{2\pi^2}[\pi - 2\mathrm{arccos}(\epsilon/b) - \frac{b}{\sqrt{\epsilon^2+b^2}}\frac{-\epsilon}{b}\times 2] \\
&= \frac{\epsilon}{2\pi^2}[-\frac{b^2+\epsilon^2}{b}(-\pi/2) + \frac{\epsilon^2}{b}(-\pi)] \\
&+ \frac{b\epsilon}{2\pi^2}[\pi - 2\mathrm{arccos}(\epsilon/b) + \frac{2\epsilon}{\sqrt{\epsilon^2+b^2}}] \\
&= \frac{b\epsilon}{2\pi} - \frac{b\epsilon}{\pi^2}\mathrm{arccos}(\frac{\epsilon}{\mathrm{b}}) + \frac{b\epsilon^2}{\pi^2\sqrt{\epsilon^2+b^2}}.
\end{aligned} \tag{7.43}$$

Where I_2 can be calculated by

$$\begin{aligned}
I_2 &= \frac{1}{2\pi^2}\int\frac{1}{|g'(k_2)|}k_2^2\mathrm{sin}(\theta)\mathrm{d}\theta \\
&= \frac{1}{2\pi^2}\int\frac{\epsilon}{|k_2 - b\mathrm{sin}(\theta)|}k_2^2\mathrm{sin}(\theta)\mathrm{d}\theta \\
&= \frac{1}{2\pi^2}\int\frac{\epsilon}{|b\mathrm{sin}(\theta) - \sqrt{\epsilon^2-b^2\mathrm{cos}^2(\theta)} - b\mathrm{sin}(\theta)|} \\
&\times [b\mathrm{sin}(\theta) - \sqrt{\epsilon^2-b^2\mathrm{cos}^2(\theta)}]^2\mathrm{sin}(\theta)\mathrm{d}\theta \\
&= \frac{1}{2\pi^2}\int\frac{\epsilon}{\sqrt{\epsilon^2-b^2\mathrm{cos}^2(\theta)}}[b\mathrm{sin}(\theta) - \sqrt{\epsilon^2-b^2\mathrm{cos}^2(\theta)}]^2\mathrm{sin}(\theta)\mathrm{d}\theta \\
&= \frac{\epsilon}{2\pi^2}\int -[\frac{b^2+\epsilon^2}{\sqrt{\epsilon^2-b^2\mathrm{cos}^2(\theta)}} - \frac{2b^2\mathrm{cos}^2(\theta)}{\sqrt{\epsilon^2-b^2\mathrm{cos}^2(\theta)}}]\mathrm{dcos}(\theta) \\
&- \int\frac{\epsilon}{2\pi^2}2b\mathrm{sin}^2(\theta)\mathrm{d}\theta,
\end{aligned} \tag{7.44}$$

$$\begin{aligned}
I_2 &= \frac{\epsilon}{2\pi^2}\int_{\epsilon/b}^{-\epsilon/b} -[\frac{b^2+\epsilon^2}{\sqrt{\epsilon^2-b^2x^2}} \\
&- \frac{2b^2x^2}{\sqrt{\epsilon^2-b^2x^2}}]\mathrm{d}x - \int_{\arccos(\epsilon/b)}^{\pi-\arccos(\epsilon/b)} \frac{\epsilon}{2\pi^2}2b\sin^2(\theta)\mathrm{d}\theta \\
&= \frac{\epsilon}{2\pi^2}[-\frac{b^2+\epsilon^2}{b}(-\pi/2)+\frac{\epsilon^2}{b}(-\pi)] \\
&+ \frac{b\epsilon}{2\pi^2}[\pi - 2\arccos(\epsilon/b) - \frac{2\epsilon}{\sqrt{\epsilon^2+b^2}}] \\
&= \frac{b\epsilon}{2\pi} + \frac{b\epsilon}{\pi^2}\arccos(\frac{\epsilon}{\mathrm{b}}) - \frac{b\epsilon^2}{\pi^2\sqrt{\epsilon^2+b^2}}.
\end{aligned} \tag{7.45}$$

Therefore, $g(\epsilon) = \frac{b\epsilon}{\pi}$ for $\epsilon < b$. When $\epsilon \leq b$, $f(k) = 0$ only has one root

$$k_1 = b\sin(\theta) + \sqrt{\epsilon^2 - b^2\cos^2(\theta)}, \tag{7.46}$$

where $\theta \in [0,\ \pi]$.

$$\begin{aligned}
g(\epsilon) &= \frac{1}{2\pi^2}\int \frac{1}{|h'(k_1)|}k_1^2\sin(\theta)\mathrm{d}\theta \\
&= \frac{\epsilon}{2\pi^2}\int [\frac{b^2+\epsilon^2}{\sqrt{\epsilon^2-b^2\cos^2(\theta)}} - \frac{2b^2\cos^2(\theta)}{\sqrt{\epsilon^2-b^2\cos^2(\theta)}} + 2b\sin(\theta)]\sin(\theta)\mathrm{d}\theta \\
&= \frac{\epsilon}{2\pi^2}\int_1^{-1}[-\frac{b^2+\epsilon^2}{b\sqrt{\epsilon^2/b^2-x^2}} + \frac{2bx^2}{\sqrt{\epsilon^2/b^2-x^2}}]\mathrm{d}x \\
&+ \int_0^{\pi}\frac{\epsilon}{2\pi^2}2b\sin^2(\theta)\mathrm{d}\theta \\
&= \frac{\epsilon}{2\pi^2}[-\frac{b^2+\epsilon^2}{b}\arcsin(\frac{bx}{\epsilon}) + 2b[-\frac{1}{2}x\sqrt{\epsilon^2/b^2-x^2} \\
&+ \frac{1}{2}(\frac{\epsilon}{b})^2\arcsin(\frac{bx}{\epsilon})]]|_1^{-1} + \frac{b\epsilon}{2\pi^2}[\theta - \sin(\theta)\cos(\theta)]|_0^{\pi} \\
&= \frac{\epsilon}{2\pi^2}[-\frac{b^2+\epsilon^2}{b}\arcsin(-\frac{b}{\epsilon})\times 2 \\
&+ 2b[\frac{1}{2}\sqrt{\epsilon^2/b^2-1}\times 2 + \frac{1}{2}(\frac{\epsilon}{b})^2\arcsin(-\frac{b}{\epsilon})\times 2]] + \frac{b\epsilon}{2\pi^2}[\pi - 0] \\
&= \frac{\epsilon}{2\pi^2}[2\frac{b^2+\epsilon^2}{b}\arcsin(\frac{b}{\epsilon}) + 2b[\sqrt{\epsilon^2/b^2-1} - (\frac{\epsilon}{b})^2\arcsin(\frac{b}{\epsilon})]] + \frac{b\epsilon}{2\pi} \\
&= \frac{b\epsilon}{\pi^2}\arcsin(\frac{b}{\epsilon}) + \frac{\epsilon}{\pi^2}\sqrt{\epsilon^2-b^2} + \frac{b\epsilon}{2\pi}.
\end{aligned} \tag{7.47}$$

Therefore, the density of states for the upper branch is given by

$$g_1(\epsilon) = \begin{cases} \frac{b\epsilon}{\pi} & \epsilon < b. \\ \frac{b\epsilon}{\pi^2}\arcsin(\frac{b}{\epsilon}) + \frac{\epsilon}{\pi^2}\sqrt{\epsilon^2-b^2} + \frac{b\epsilon}{2\pi} & \epsilon \geq b. \end{cases} \tag{7.48}$$

When $\epsilon = b$, $g(\epsilon) = \frac{b\epsilon}{\pi^2} \times \frac{\pi}{2} + \frac{b\epsilon}{2\pi} = \frac{b\epsilon}{\pi}$ indicates that the density of states is continuous. If we set $b = 0$, then $g(\epsilon) = \frac{\epsilon^2}{\pi^2}$ agrees well with the density of states of 3D Dirac materials.

Now we discuss another energy momentum branch *i.e.*,

$$\epsilon = \sqrt{k_x^2 + (\sqrt{k_y^2 + k_z^2} + b)^2} = \sqrt{k^2 + b^2 + 2kb\mathrm{sin}(\theta)}, \tag{7.49}$$

$$\begin{aligned} \epsilon^2 &= k^2 + b^2 + 2kb\mathrm{sin}(\theta) = (k + b\mathrm{sin}(\theta))^2 + b^2 - b^2\mathrm{sin}^2(\theta) \\ &= (k + b\mathrm{sin}(\theta))^2 + b^2\mathrm{cos}^2(\theta). \end{aligned} \tag{7.50}$$

Therefore, k can be written as

$$k_\pm = -b\mathrm{sin}(\theta) \pm \sqrt{\epsilon^2 - b^2\mathrm{cos}^2(\theta)}. \tag{7.51}$$

In spherical coordinates, k is always a non-negative real number. Therefore, only $k_1 = -b\mathrm{sin}(\theta) + \sqrt{\epsilon^2 - b^2\mathrm{cos}^2(\theta)}$ may meet the requirement and it further requires $\sqrt{\epsilon^2 - b^2\mathrm{cos}^2(\theta)} > b\mathrm{sin}(\theta)$ *i.e.*, $\epsilon > b$. This makes $(\epsilon^2 - b^2\mathrm{cos}^2(\theta))$ always greater than zero, where $\theta \in [0, \pi]$. Let $f(k) = \epsilon - \sqrt{k^2 + b^2 + 2kb\mathrm{sin}(\theta)} = 0$, then $f'(k) = \frac{k + b\mathrm{sin}(\theta)}{\epsilon}$. The density of states can be obtained by

$$\begin{aligned} g(\epsilon) &= \frac{1}{2\pi^2}\int \frac{1}{|f'(k_1)|}k_1^2\mathrm{sin}(\theta)\mathrm{d}\theta = \frac{1}{2\pi^2}\int \frac{\epsilon}{|k_1 + b\mathrm{sin}(\theta)|}k_1^2\mathrm{sin}(\theta)\mathrm{d}\theta \\ &= \frac{1}{2\pi^2}\int \frac{\epsilon}{|-b\mathrm{sin}(\theta) + \sqrt{\epsilon^2 - b^2\mathrm{cos}^2(\theta)} + b\mathrm{sin}(\theta)|}[-b\mathrm{sin}(\theta) \\ &+ \sqrt{\epsilon^2 - b^2\mathrm{cos}^2(\theta)}]^2\mathrm{sin}(\theta)\mathrm{d}\theta \\ &= \frac{\epsilon}{2\pi^2}\int [\frac{b^2 + \epsilon^2}{\sqrt{\epsilon^2 - b^2\mathrm{cos}^2(\theta)}} - \frac{2b^2\mathrm{cos}^2(\theta)}{\sqrt{\epsilon^2 - b^2\mathrm{cos}^2(\theta)}} - 2b\mathrm{sin}(\theta)]\mathrm{sin}(\theta)\mathrm{d}\theta \\ &= \frac{\epsilon}{2\pi^2}[-\frac{b^2 + \epsilon^2}{b}\mathrm{arcsin}(\frac{bx}{\epsilon}) + 2b[-\frac{1}{2}x\sqrt{\epsilon^2/b^2 - x^2} \\ &+ \frac{1}{2}(\frac{\epsilon}{b})^2\mathrm{arcsin}(\frac{bx}{\epsilon})]]|_1^{-1} - \frac{b\epsilon}{2\pi^2}[\theta - \mathrm{sin}(\theta)\mathrm{cos}(\theta)]|_0^\pi \\ &= \frac{\epsilon}{2\pi^2}[2\frac{b^2 + \epsilon^2}{b}\mathrm{arcsin}(\frac{b}{\epsilon}) + 2b[\sqrt{\epsilon^2/b^2 - 1} \\ &- (\frac{\epsilon}{b})^2\mathrm{arcsin}(\frac{b}{\epsilon})]] - \frac{b\epsilon}{2\pi} \\ &= \frac{b\epsilon}{\pi^2}\mathrm{arcsin}(\frac{b}{\epsilon}) + \frac{\epsilon}{\pi^2}\sqrt{\epsilon^2 - b^2} - \frac{b\epsilon}{2\pi}. \end{aligned} \tag{7.52}$$

Therefore, the density of states for the whole system is given by

$$g(\epsilon) = \begin{cases} \frac{b\epsilon}{\pi} & \epsilon < b, \\ \frac{2b\epsilon}{\pi^2}\mathrm{arcsin}(\frac{b}{\epsilon}) + \frac{2\epsilon}{\pi^2}\sqrt{\epsilon^2 - b^2} & \epsilon \geq b. \end{cases} \tag{7.53}$$

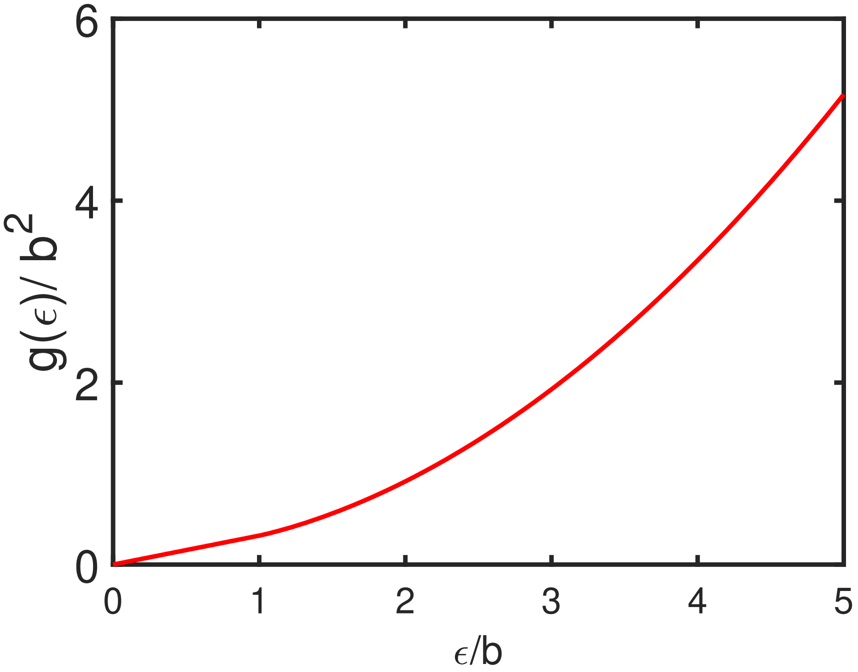

Figure 7.1: The density of states for nodal-ring system.

When $\epsilon = b$, $g(\epsilon) = \frac{2b\epsilon}{\pi^2} \times \frac{\pi}{2} = \frac{b\epsilon}{\pi}$ indicates that the density of states is continuous. The density of states is plotted in Fig. 7.1.

A.3 The third-order current in graphene

The low energy-momentum dispersion of graphene is

$$\epsilon = \hbar k v_F = \hbar\sqrt{p_x^2 + p_y^2}. \tag{7.54}$$

By using the energy-momentum dispersion, we obtained the third-order velocity in the x-direction as

$$\begin{aligned} v_x^{(3)} &= \tfrac{v_F}{6}(-\tfrac{3}{p^3} + \tfrac{18p_x^2}{p^5} - \tfrac{15p_x^4}{p^7})u_x^3 \\ &= \tfrac{6\cos^2\theta - 5\cos^4(\theta) - 1}{2p^3})u_x^3 v_F. \end{aligned} \tag{7.55}$$

Graphene is an isotropic system. Therefore we can safely set $u_y = 0$ to simple the calculations. The third-order current at $T = 0$ K is calculated by

$$\begin{aligned} J_3 &= 4e\int\int v^{(3)}(\Theta(\epsilon) - \Theta(\epsilon - \Delta))\mathrm{d}k_x\mathrm{d}k_y \\ &= 4e\int\int \frac{6\cos^2\theta - 5\cos^4\theta - 1}{6p^3})\frac{u_x^3 v_F}{\hbar^2}(\Theta(\epsilon) - \Theta(\epsilon - \Delta))\mathrm{d}p_x\mathrm{d}p_y \\ &= 4e\int\int \frac{6\cos^2\theta - 5\cos^4\theta - 1}{2p^3})\frac{u_x^3 v_F}{\hbar^2}(\Theta(\epsilon) - \Theta(\epsilon - \Delta))p\mathrm{d}\theta\mathrm{d}p \\ &= \frac{2ev_F^2 u_x^3}{\hbar^2}\int_{\mu-\Delta}^{\mu}\int_0^{2\pi} \frac{6\cos^2\theta - 5\cos^4\theta - 1}{\epsilon^2})\mathrm{d}\theta\mathrm{d}\epsilon \\ &= (18\pi - 8)\frac{ev_F u_x^3\Delta}{\hbar^2\mu(\mu - \Delta)} \approx \frac{12e^4 v_F^2 E^3\Delta}{\hbar^2\mu^2\omega^3}, \end{aligned} \tag{7.56}$$

where the factor 4 is for spin and valley degree, and Δ is far less than μ.

A.4 Math tools used in the main text

(a) **Coordinate systems**

For a three dimensional space coordinate system, there are three independent coordinate variables u_1, u_2 and u_3. Take Cartesian coordinate system for example, $u_1 = x$, $u_2 = y$ and $u_3 = z$.

In spherical coordinates, $u_1 = r$, $u_2 = \phi$ and $u_3 = \theta$, where r the length of coordinate vector, ϕ is the angle between z axis and the vector, θ is the angle between x axis and the xy plane projection of r. The relationship between those two coordinate systems are

$$x = r\mathrm{sin}(\theta)\mathrm{cos}(\phi), \tag{7.57}$$

$$y = r\mathrm{sin}(\theta)\mathrm{sin}(\phi), \tag{7.58}$$

$$z = r\mathrm{cos}(\theta). \tag{7.59}$$

In spherical coordinates, coordinate axises have different unit such as length and angle. To overcome this, a parameter called metric coefficient is introduced,

$$h_n = \sqrt{(\frac{\partial x_1}{\partial u_n})^2 + (\frac{\partial x_2}{\partial u_n})^2 + (\frac{\partial x_3}{\partial u_n})^2}. \tag{7.60}$$

For Cartesian coordinate system, $h_1 = h_2 = h_3 = 1$, while for spherical coordinates, $h_1 = 1$, $h_2 = r$ and $h_3 = rsin(\theta)$. In Cartesian coordinate system, potential gradient can be written as

$$\nabla V = \frac{\partial V}{\partial l_1}\hat{e_1} + \frac{\partial V}{\partial l_2}\hat{e_2} + \frac{\partial V}{\partial l_3}\hat{e_3} = \frac{\partial V}{\partial x}\hat{e_x} + \frac{\partial V}{\partial y}\hat{e_y} + \frac{\partial V}{\partial z}\hat{e_z}, \tag{7.61}$$

where $l_n = h_n du_n$. In spherical coordinates, potential gradient can be written as

$$\nabla V = \frac{\partial V}{\partial r}\hat{e_r} + \frac{\partial V}{r\partial \theta}\hat{e_\theta} + \frac{\partial V}{rsin(\theta)\partial \phi}\hat{e_\phi}. \tag{7.62}$$

(b) **Integal formulas**

Skills for integraling the imaginary part of optical conductivity.

$$\mathrm{Im}\int_0^\infty \frac{f(x)}{g(x)} = \pi \sum_{x_0} \frac{f(x_0)}{|g'(x_0)|}, \tag{7.63}$$

where $g(x_0) = 0$ and $x_0 > 0$. For example,

$$\mathrm{Im}\int_0^\infty \frac{x + x^2}{x^2 - a^2} = \pi \sum_{x_0} \frac{f(x_0)}{|g'(x_0)|} = \frac{a + a^2}{2a}\pi = \frac{1 + a}{2}\pi. \tag{7.64}$$

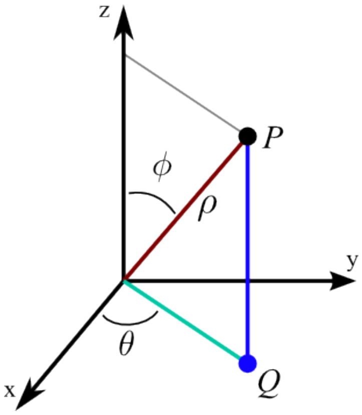

Figure 7.2: Low energy spectra of Dirac and Weyl semimetals.

Cauchy principles intergal.

We want to evaluate $I = \int_0^\infty \frac{sin(x)}{x}$ that contains a singular pole at $x = 0$. Hence, Cauchy's integral principle is needed, which is given by

$$\oint \frac{sin(z)}{z} = \int_{-\infty}^{-\epsilon} \frac{sin(z)}{z} + \int_{C_m} \frac{sin(z)}{z} + \int_{\epsilon}^{\infty} \frac{sin(z)}{z} + \int_{C_r} \frac{sin(z)}{z}. \tag{7.65}$$

Then the target intergal is written by

$$\begin{aligned} I &= \frac{1}{2}\int_{-\infty}^{\infty} \frac{sin(z)}{z} = \frac{1}{2}[\oint \frac{sin(z)}{z} - \int_{C_m} \frac{sin(z)}{z} - \int_{C_r} \frac{sin(z)}{z}] \\ &= \frac{1}{2}[I_1 - I_2 - I_3]. \end{aligned} \tag{7.66}$$

There are two paths to evaluate the intergal Fig.7.3(a) and (b). Firstly, we consider the situation (a), where $I_1 = \oint \frac{sin(z)}{z} = 0$ due to no singular polar inside the intergal path, $I_2 = \int_{C_r} \frac{sin(z)}{z} = 0$ and I_3 is caculated by

$$\begin{aligned} I_3 &= \int_{C_m} \frac{sin(z)}{z} = lim_{\epsilon \to 0} \int_{C_m} \frac{\mathrm{Im} \mathrm{e}^{iz}}{\epsilon \mathrm{e}^{i\theta}} \epsilon \mathrm{e}^{i\theta} i \mathrm{d}\theta = \mathrm{Im} lim_{\epsilon \to 0} \int_{C_m} e^{i\epsilon e^{i\theta}} i \mathrm{d}\theta \\ &= \mathrm{Im} \int_{C_m} i \mathrm{d}\theta = \mathrm{Im} \int_{\pi}^{0} = -\pi. \end{aligned} \tag{7.67}$$

Thus, $I = 0.5\pi$.

The second situation is slightly different from the first one, where $I_1 = \mathrm{Im} \frac{\mathrm{e}^{iz}}{z} = \mathrm{Im} 2\pi i \mathrm{Res} \frac{\mathrm{e}^{iz}}{0} = 2\pi$, $I_2 = 0$ and $I_3 = \mathrm{Im} \int_{\pi}^{2\pi} = \pi$. Therefore, I still equals to 0.5π agreeing with the first situation.

Some integral formulae.

$$\int_m^\infty \mathrm{e}^{-cx} \mathrm{d}x = \frac{1}{c} \mathrm{e}^{-cm}. \tag{7.68}$$

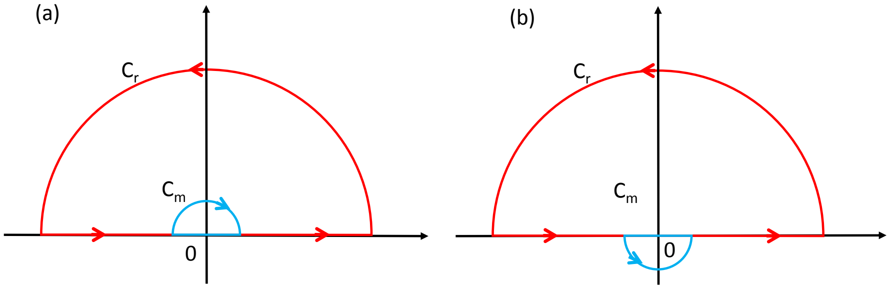

Figure 7.3: Cauchy principle intergral for sin $(x)/x$.

$$\int_m^\infty x\mathrm{e}^{-cx}\mathrm{d}x = (\frac{m}{c} + \frac{1}{c^2})\mathrm{e}^{-cm}. \tag{7.69}$$

$$\int_m^\infty x^2\mathrm{e}^{-cx}\mathrm{d}x = (\frac{m^2}{c} + \frac{2m}{c^2} + \frac{2}{c^3})\mathrm{e}^{-cm}. \tag{7.70}$$

$$\int_m^\infty x^3\mathrm{e}^{-cx}\mathrm{d}x = (\frac{m^3}{c} + \frac{3m^2}{c^2} + \frac{6m}{c^3} + \frac{6}{c^4})\mathrm{e}^{-cm}. \tag{7.71}$$

$$\int_m^\infty x^4\mathrm{e}^{-cx}\mathrm{d}x = (\frac{m^4}{c} + \frac{4m^3}{c^2} + \frac{12m^2}{c^3} + \frac{24m}{c^4} + \frac{24}{c^4})\mathrm{e}^{-cm}. \tag{7.72}$$

(c) **Ways to calculate velocity along one direction**

For single layer graphene, the Hamiltonian can be written as

$$H = \hbar v_F \begin{pmatrix} 0 & k_x - ik_y \\ k_x + k_y & 0 \end{pmatrix}. \tag{7.73}$$

The eigenvalues and corresponding wavefunctions are obtained by $\epsilon = \pm\hbar v_F k$ and $\Psi(r)_\pm$ $=\frac{1}{\sqrt{2}}(e^{i\phi}, \pm 1)$.

1. Obtaining v_x from energy

$$v_x = \frac{\partial\epsilon}{\partial p_x} = \frac{\hbar v_F \partial\sqrt{k_x^2 + k_y^2}}{\hbar\partial k_x} = v_f \frac{k_x}{\sqrt{k_x^2 + k_y^2}} = v_F cos(\phi). \tag{7.74}$$

where ϕ is the angle between k_x and k_y.

2. Obtaining v_x from wave function

$$v_x =< \Psi^*|\hat{v}_x|\Psi >, \tag{7.75}$$

where $\hat{v}_x = \frac{\partial H}{\hbar \partial k_x}$ can be written as

$$\hat{v}_x = v_F \begin{pmatrix} 0 & 1 \\ 1 & 0 \end{pmatrix}. \tag{7.76}$$

$$v_x =< \Psi^*|\hat{v}_x|\Psi >= \frac{v_F}{2}(e^{-i\phi}, 1) \begin{pmatrix} 0 & 1 \\ 1 & 0 \end{pmatrix} (e^{i\phi}, 1)^T = \frac{v_F}{2}(e^{i\phi} + e^{-i\phi}) = v_F cos(\phi). \tag{7.77}$$

(d) **Density of states**

1. two dimensional conversional materials.

$$D(\epsilon_0) = \frac{g}{(2\pi)^2} \int_0^\infty 2\pi k \delta[\epsilon(k) - \epsilon(k_0)] \mathrm{d}k = \frac{g}{2\pi} \frac{k}{|\epsilon'(k_0)|} = \frac{m}{\pi \hbar^2}, \tag{7.78}$$

where $g = 2$ is spin degeneracy and $\epsilon(k) = \hbar^2 k^2/(2m)$.

2. three dimensional conversional materials.

$$D(\epsilon_0) = \frac{g}{(2\pi)^3} \int_0^\infty 4\pi k^2 \delta[\epsilon(k) - \epsilon(k_0)] \mathrm{d}k = \frac{g}{2\pi^2} \frac{k^2}{|\epsilon'(k_0)|} = \frac{(2m)^{3/2}}{2\pi^2 \hbar^3} \sqrt{\epsilon}. \tag{7.79}$$

3. two dimensional Dirac materials.

$$D(\epsilon_0) = \frac{g}{(2\pi)^2} \int_0^\infty 2\pi k \delta[\epsilon(k) - \epsilon(k_0)] \mathrm{d}k = \frac{g}{2\pi} \frac{k}{\gamma} = \frac{\epsilon}{\pi \gamma^2}, \tag{7.80}$$

where $\epsilon(k) = \gamma k$ and $|\epsilon'(k)| = \gamma$.

4. three dimensional Dirac materials.

$$D(\epsilon_0) = \frac{g}{(2\pi)^3} \int_0^\infty 4\pi k^2 \delta[\epsilon(k) - \epsilon(k_0)] \mathrm{d}k = \frac{g}{2\pi^2} \frac{k^2}{\gamma} = \frac{\epsilon^2}{\pi^2 \gamma^3}. \tag{7.81}$$

Therefore, the densiy of states of three dimensional mateirals changes more quickly with energy than that of two dimensional materials and it changes more quickly in Dirac system than in convensional systems.